NOV 2 6 1979

Y3.N88:25/0470

NUREG/CR-0470
SAND78-2002
Vol. 8
R-7

COMPLETED

Advanced Reactor Safety Research Quarterly Report July-September 1978

Advanced Reactor Research Department

Sandia Laboratories

SF 2900 Q(7-73)

Prepared for
U. S. NUCLEAR REGULATORY COMMISSION

200

NOTICE

This report was prepared as an account of work sponsored by an agency of the United States Government. Neither the United States Government nor any agency thereof, or any of their employees, makes any warranty, expressed or implied, or assumes any legal liability or responsibility for any third party's use, or the results of such use, of any information, apparatus, product or process disclosed in this report, or represents that its used by such third party would not infringe privately owned rights.

The views expressed in this report are not necessarily those of the U.S. Nuclear Regulatory Commission.

Available from
National Technical Information Service
Springfield, VA 22161

NUREG/CR-0470
SAND78-2002
Vol. 8
R-7

ADVANCED REACTOR SAFETY RESEARCH
QUARTERLY REPORT
JULY-SEPTEMBER 1978

Advanced Reactor Research Department
Sandia Laboratories, Albuquerque, New Mexico 87185

Printed: September 1979

APPROVED:

Manager, Advanced Reactor Research

Director, Nuclear Fuel Cycle Programs

Sandia Laboratories
Albuquerque, New Mexico 87185
operated by
Sandia Corporation
for the
U. S. Department of Energy

Prepared for
Division of Reactor Safety Research
Office of Nuclear Regulatory Research
U.S. Nuclear Regulatory Commission
Washington, DC 20555
Under Interagency Agreement DOE 40-550-75
NRC FIN Nos. A-1016, -1172, -1180,
-1186, -1054, -1181, -1032, -1058, -1198, -1197

BLANK PAGE

CONTENTS

Page

FOREWORD 11

EXECUTIVE SUMMARY 13

1. ENERGETICS 39
   - 1.1 Prompt Burst Energetics 39
   - 1.2 Equation-of-State 51

2. FUEL DYNAMICS 67
   - 2.1 Fuel Disruption 67
   - 2.2 Transition Phase 75
   - 2.3 Initial and Extended Fuel Motion 85
   - 2.4 Fuel Motion Detection 88

3. CORE DEBRIS BEHAVIOR - INHERENT RETENTION 105
   - 3.1 Molten Core Technology 105
   - 3.2 PAHR Debris Bed 127
   - 3.3 PAHR Molten Pool 135
   - 3.4 Containment Analysis 141
   - 3.5 Fragmentation 142
   - 3.6 Sodium Containment and Structural Integrity 147

4. AEROSOL SOURCE NORMALIZATION 159

5. ELEVATED TEMPERATURE DESIGN ASSESSMENT 163

6. LMFBR ACCIDENT DELINEATION 175

7. TEST AND FACILITY TECHNOLOGY 193
   - 7.1 ACPR Upgrade - Initial Test and Operations 193
   - 7.2 ACPR Fuel-Motion Detection System 193
   - 7.3 Large-Scale Test Assessment 195

ILLUSTRATIONS

Figure		Page
1.1-1	HONDO Model of Piston-Sleeve	41
1.1-2	Sodium Pressurization	43
1.1-3	Piston Velocity	43
1.1-4	Piston Displacement	43
1.2-1	Pressure Transducer Signal of a Vapor Pressure Transient in the SPR-III Reactor	53
1.2-2	Fission Density Profiles in a UO_2 Sample Calculated by Transport Theory and Monte Carlo	55
1.2-3	Fission Density Profiles in a UO_2 Sample Calculated by Transport and Diffusion Theory	56
1.2-4	Comparison of Filtered and Bare Energy Deposition Profiles for a UO_2 Sample	57
1.2-5	Calculated Temperature vs Time for the Nonequilibrium Model (A) and the Equilibrium Model (B) of the Heat Capacity	61
1.2-6	Measured Temperature vs Time for Frames 1 Through 5	62
1.2-7	Theoretical Predictions of Center Hole Temperature on End of Fuel Segment for the Nonequilibrium Model (A) and the Equilibrium Model (B) of the Heat Capacity, and Measured Values, Given by Xs for Odd Frames 1 Through 9	62
2.1-1	Predicted and Calculated Fuel Swelling - Test FD 1.4	73
2.1-2	Predicted and Calculated Fuel Swelling - Test FD 1.7	74
2.1-3	Predicted and Calculated Fuel Swelling - Test FD 1.8	74
2.2-1	Schematic of Liquid-Liquid Ablation Experiment Apparatus	79
2.2-2	Observed Melting Pattern During Liquid-Liquid Ablation Experiments	81
2.3-1	Axial Fission Density in CABRI A2 Test Pin in CABRI and ACRR (Polyethylene Moderated Test)	87
2.4-1	Fuel Pin Motion Flash X-Ray Cinematography	93
2.4-2	Lead Brick Target Used in Detection Studies With LINAC	94
2.4-3	LINAC and Active Detector System Geometry (Top View)	95
2.4-4	Characteristics of Kodak 2484 Film Developed for 6 Minutes in D-19 Developer at 68°F (20°C)	98
2.4-5	Reconstructed Image of the ^{252}Cf Source Obtained by Imaging Neutrons With Energies ≥ 1.5 MeV	102

ILLUSTRATIONS (Cont)

Figure		Page
3.1-1	Locations of Refractory Specimens in Test BURN 0	112
3.1-2	Posttest X-Ray of BURN 0 Crucible	114
3.1-3	Posttest X-Ray of BURN 0 Crucible	115
3.1-4	Schematic of Test Fixture Used in Test BURN 3	115
3.1-5	Test BURN 3 - Steel Temperature (°C)	118
3.1-6	Test BURN 3 - Cap Thermocouple	118
3.1-7	Test BURN 3 - Wall Thermocouple 0.25 In. Above Cavity Bottom	119
3.1-8	Test BURN 3 - Thermocouple 1 In. Above Cavity Bottom	119
3.1-9	Test BURN 3 - Thermocouple 1 In. Below Cavity Bottom	120
3.1-10	Top View of Steel From Test BURN 3	121
3.1-11	Bottom View of Steel From Test BURN 3	121
3.1-12	Posttest X-Ray of the Test BURN 4 Crucible	125
3.2-1	Conduction Model of Dryout Zone, Initial Hypothesis	129
3.2-2	Calculated Temperature Elevations (Eq 3.1) vs Time at 1.5 mm Above the Bottom of the Bed for Three Thicknesses of Dryout Zone, Compared With Observed Temperature Transient During Dryout of the D-3 Experiments (circles)	129
3.2-3	Conduction Model of Dryout Zone, Second Hypothesis	131
3.2-4	Calculation (solid line), Using Eqs (3.3) and (3.4), Compared With Data Points From Dryout 4, D-3 Experiment	131
3.2-5	Values of Variable Dryout Zone Thickness (Z) Calculated for Dryouts 1 Through 4 for the D-3 Experiment	132
3.2-6	Power Partitioning During Dryout as Calculated for Dryout Expansion 4	134
3.5-1	A Typical Fragment Weight Fraction	144
3.5-2	FRAG 2 Fragments as Classified by Sieving	145
3.5-3	Typical SEM From FRAG 2 Showing Two-Phase Particles, Typical of Energetic Interactions	146
3.6-1	Crucible Temperatures and Sodium Pool Temperature, Test 11	148
3.6-2	Basalt Concrete Crucible Penetration, Test 11	149
3.6-3	Top View of Crack Pattern of Basalt Concrete Crucible, Test 11	149
3.6-4	Side Views of Cracking Pattern of Basalt Concrete Crucible, Test 11	150
3.6-5	Arrangement of Firebrick and Insert in Concrete Crucible Cavity, Test 12	152

ILLUSTRATIONS (Cont)

Figure		Page
3.6-6	South Brick (SB) Temperatures and Crucible (CR) Temperature (South Side)	152
3.6-7	Test No. 12 Liner Configuration Posttest vs Pretest	153
3.6-8	Test No. 12 Posttest Circumferential Distribution of Radial Cracks	154
4.2-1	Schematic of Experimental Canister To Be Used for In-Pile Aerosol Source Experiments, Series II	160
4.2-2	Distribution of Total Particle Mass According to Size for Particle Sampled in In-Pile Aerosol Source Experiment, Series I	161
5.3-1	PA Measurements of Isochronally Annealed 25% Cold Worked Type 316 Stainless Steel	168
5.3-2	Hardness of Isochronally Annealed 25% and 75% Cold Worked Type 316 Stainless Steel	169
5.6-1	Comparison of Creep Laws	172
6.2-1	Areas of LMFBR Accident Delineation Study	176
6.3-1	Schematic of the Principal Systems Essential to the Generation and Transport of Heat	178
6.3-2	Event Tree for a Reactor Control Subsystem Failure	179
6.5-1	Model Containment System	186
7.3-1	Fission Density Profiles in CABRI Test Pins in CABRI Reactor	197
7.3-2	Power History in CABRI, P_o = 14 MW, P = \$2.7	198

TABLES

Table		Page
1-I	Sodium Pressure at Several Distances from Piston Face	42
1-II	Comparison of EXPAND Results with Experiment	44
1-III	EXPAND Results	46
1-IV	Energy Conversion Results for PBE Oxide/Sodium Experiments	49
2-I	Comparison of Laminar and Turbulent Transpiration Effects	78
2-II	Comparison of Total Transpiration Heat Transfer Rate to Nonablation Heat Transfer Rate	78
2-III	2484 Film Characteristics Scanned With 50- by 50-μm Aperture, 201 Data Points	96
2-IV	LINAC Film, 2484, Three Gains, Scanned With 50- by 50-μm Aperture, 201 Data Points	97
2-V	LINAC Data, 2484 Film, Three Gains	99
3-I	Summary of BURN Tests	107
3-II	Summary of Planned X-Ray Tests	108
3-III	Future BURN Series Tests	111
3-IV	Test BURN 3 Fixture Dimensions	116
3-V	Thermocouples Used in Test BURN 3	117
3-VI	Summary of Planned CATH Tests	126
3-VII	Chemical Analyses of Reaction Products, Test No. 11	150
3-VIII	Analysis of Firebrick	154
5-I	Creep Testing of Type 316 Stainless Steel	164
5-II	Type 316 Stainless Steel Creep-Fatigue Test Matrix at Mar-Test Inc.	165
5-III	Fatigue Tests for Sequential Surface PA Measurements and Crack Observations	166
6-I	Possible Outcome Categories for a Reactor Control Subsystem Failure	180

BLANK PAGE

FOREWORD

Sandia Laboratories' Advanced Reactor Safety Research Program, initiated in FY75, is a comprehensive research activity conducted on behalf of the U.S. Nuclear Regulatory Commission (NRC) and is part of NRC's confirmatory research effort to assure that the necessary safety data and theoretical understanding exist to license and regulate the Liquid Metal Fast Breeder Reactor (LMFBR) or other advanced converters and breeders which may be commercialized in the United States. The program includes a broad range of experiments to simulate accidental transient and postaccident conditions in the LMFBR, to provide the required data base to understand the controlling accident sequences, and to serve as a basis for verification of the complex computer simulation models and codes used in accident analysis and licensing reviews. Such a program must include the development of analytical models, verified by experiment, which can be used to predict reactor performance under a broad variety of abnormal conditions. This work along with that of other United States and International researchers should provide the technology base on which licensing decisions can be made with confidence that the safety of the public is assured.

The early thrust of Sandia's program was designed to provide data associated with the hypothetical core disruptive accident, with emphasis on prompt burst (~ 1-ms period) energetics and the behavior of postaccident core debris. The scope of the program was expanded in FY76 and FY77 to encompass other energetics and inherent retention concerns such as large-scale sodium containment and structural integrity, aerosol source studies, transition phase energetics, fuel failure and motion, and studies to quantify elevated temperature failure modes of critical component materials. A portion of the initial effort in the program was directed toward obtaining data to support the licensing review of the Clinch River Breeder Reactor (CRBR). Another important early thrust of the program is the development of the test facilities and techniques. In mid-FY77 three additional tasks were initiated: Fuel Failure, Containment Analysis, and Advanced Reactor Safety Research Assessment. For FY78, the program is organized in the following subtasks, progress of which is reported herein.

TASK 1 Energetics

- Subtask 1.1 - Prompt Burst Energetics (PBE)
- Subtask 1.2 - Equation-of-State (EOS)

TASK 2 Fuel Dynamics

- Subtask 2.1 - Fuel Disruption
- Subtask 2.2 - Transition Phase
- Subtask 2.3 - Initial and Extended Fuel Motion
- Subtask 2.4 - Fuel Motion Detection
  - a. In-Core Systems
  - b. Electron Beam Flash X-Radiography
  - c. Coded Aperture Imaging

TASK 3 Core Debris Behavior - Inherent Retention

- Subtask 3.1 - Molten Core Technology
- Subtask 3.2 - PAHR Debris Bed
- Subtask 3.3 - PAHR Molten Pool
- Subtask 3.4 - Containment Analysis
- Subtask 3.5 - Fragmentation
- Subtask 3.6 - Sodium Containment and Structural Integrity

TASK 4 Aerosol Source Normalization

TASK 5 Elevated Temperature Design Assessment

TASK 6 LMFBR Accident Delineation

TASK 7 Test and Facility Technology

- Subtask 7.1 - ACPR Upgrade - Initial Test and Operation
- Subtask 7.2 - ACPR Fuel Motion Detection Systems
- Subtask 7.3 - Large-Scale Test Assessments

EXECUTIVE SUMMARY

Introduction

Sandia Laboratories, Albuquerque, New Mexico is conducting the Advanced Reactor Safety Research Program on behalf of the U.S. Nuclear Regulatory Commission (NRC). The overall objective of the program is to provide NRC a comprehensive data base essential to: (1) defining key safety issues, (2) understanding the controlling accident sequences, (3) verifying the complex computer models used in accident analysis and licensing reviews, and (4) assuring the public that advanced power reactor systems will not be licensed and placed in commercial service in the United States without appropriate consideration being given to their effects on health and safety.

The NRC program is carefully planned to complement the larger DOE program, but the same time to satisfy the NRC obligation of independent confirmatory research.

Together with other programs, the Sandia effort is directed at assuring the soundness of the technology base upon which licensing decisions are made, and includes experiments and model and code development.

Sandia has been tasked to investigate seven major areas of interest which are intimately related to overall NRC needs. These are:

1. Energetics
2. Fuel Dynamics
3. Core Debris Behavior - Inherent Retention
4. Aerosol Source Normalization
5. Elevated Temperature Design Assessment
6. LMFBR Accident Delineation
7. Test and Facility Technology

These major tasks are subdivided as necessary into subtasks to facilitate the organization of work and the interaction of subtask results into a body of coherent information which supports the requirements of the NRC.

1. Energetics

1.1 Prompt Burst Energetics

Prompt Burst Energetics (PBE) experiments provide information on the energetic response of various reactor fuel-clad-coolant systems to superprompt critical excursions. This program is directed at characterizing the phenomena which result in pressure generation and the conversion of thermal energy to work, and reactivity effects arising from rapid coolant voiding and initial fuel motion. These experiments examine integral effects of fuel-clad-coolant interactions (FCI), fission gas release, and fuel and fission product vapor pressures during superprompt critical core disruptive accidents and determine the potential for damage to the primary containment. Furthermore, the rate of coolant voiding in a positive reactivity void-coefficient system determines the reactivity insertion rate and hence the magnitude of the transient under accident conditions. The experimental work is closely interfaced with analytical efforts to develop models which uniquely describe the observed phenomena for incorporation into predictive accident analysis as well as to provide data to verify existing accident analysis codes. These experiments also provide information about the thermodynamic states and spatial distribution of fuel, clad, and coolant following a superprompt excursion. These data serve as initial conditions for postaccident heat removal (PAHR) and molten core containment analysis.

In tests performed to date, single fuel pins have been pulse fission heated in the Annular Core Pulse Reactor (ACPR) (now modified and called the Annular Core Research Reactor, ACRR) to temperatures resulting in fuel vaporization. The pins, which have been surrounded by helium or sodium, are contained in a rigid pressure vessel which is instrumented with thermocouples and pressure transducers and which is fitted with a movable piston at its upper end. Estimates of the conversion of thermal energy to work result from comparisons of the kinetic energy of the piston to the fission energy input to the fuel. Pressure, temperature, and piston displacement histories are determined for a variety of fuel-coolant systems and initial conditions. A series of experiments with fresh uranium dioxide fuel and sodium coolant has been completed. Initial experiments with fresh uranium carbide (UC) fuel and sodium have been performed. Future experiments will examine fission product effects in preirradiated fuel. A seven-pin test vehicle for PBE experiments is under development.

During this quarter, activities were directed toward the analysis of completed experiments, completion of a topical report describing the fresh oxide/sodium PBE experiments, and preparations for upcoming experiments.

In several experiments in both the oxide/sodium and carbide/sodium systems, significant pressure transients were observed coincident with the stoppage of the piston. One possible source for the observed pressure transients is the compression of the sodium slug moving with the piston as it is decelerated. Modeling of the sodium pressurization arising from deceleration was performed for experiment PBE-9S. PBE-9S was similar to other oxide/sodium PBE experiments except that it was irradiated by using a "double-pulse" reactor-operating mode. Double-pulse irradiations provide a means to achieve fuel temperature profiles peaked inside the fuel in the PBE experiments. These conditions more closely approximate reactor conditions and may lead to more effective mixing of molten fuel and sodium before channel voiding can occur and may subsequently lead to an increase in the possibility of energetic interaction between fuel and coolant if they exist. PBE-9S yielded the most energetic response of the oxide/sodium experiments. As in previous analysis of the PBE-SG2 experiment (the most energetic UC/sodium experiment) the amplitude of the deceleration pressure in the upper sodium slug was found from the calculations to be small compared to the pressure transient observed coincident with piston stoppage. These results further support the conclusion that the observed pressure transient resulted from an FCI triggered by the hydrodynamic pressurization. These and other experimental results demonstrate that at least local fuel-coolant interactions do occur in the oxide/sodium system. The apparent triggering of FCI suggests a source of coherent interaction that must be understood and evaluated for the reactor system since this could lead to large pressures within the primary vessel.

The EXPAND pin-failure modeling was extended to the double-pulse oxide experiments. The posttest analysis with EXPAND predicted no failure for three double-pulse experiments (PBE-3S, -8S, and -10S) and in fact no failure was observed in those tests. For experiment PBE-9S, failure by stress rupture was predicted to occur about 9.6 ms after the power peak. When experiment PBE-9S was run, a pressure transient (indicating pin failure) occurred approximately 1.8 ms before the power peak. The observed difference in predicted and experimental timing (approximately 11.4 ms) for experiment PBE-9S is much larger than corresponding differences between experiment results and EXPAND predictions for all other PBE experiments. Further, the energy input at 1.8 ms before the power peak is not sufficient to melt a 20% enriched pin in PBE-9S. Possible explanations for these discrepancies are being investigated and include the possibility that the test pin was of a much higher fuel enrichment than 20%.

One objective of the PBE program is to derive estimates of the fraction of thermal energy in the fuel that is converted to work during a reactor accident in order to determine the threat to containment. In the experiments, this information is derived from measured piston motion and from the impulse represented in the histories. Estimates of the work potential in the oxide/sodium experiments were derived from the measured pressure histories. Results show substantial agreement with results derived from piston motion in those experiments for which piston motion reflects the entire pressure history. For experiments PBE-9S and -12S in which the pistons moved full travel and stopped while the channels were still pressurized, greater energy conversion efficiencies were estimated from the pressure integral analysis. These estimates yielded a maximum value of 0.54% for experiment PBE-9S.

At the request of the staff at HEDL, EXPAND was used to predict pin failure in the pending UC-fueled TREAT experiment AX-1. This work was part of a multi-laboratory effort to predict pin failure time in this experiment. Test AX-1 is designed to study fuel-coolant interactions between carbide fuel and sodium in a domain of temperatures associated with possible large-scale explosive vaporization of sodium. Thus, pin-failure time, which affects fuel temperature, is a critical parameter in that test. EXPAND was developed for such modeling, and the results for AX-1 predict failure to occur about 90 ms before the peak of the power transient.

1.2 Equation-of-State

Equation-of-state represents a crucial relationship for each material that determines hypothetical-core-disruptive-accident (HCDA) energetics in advanced reactors. In particular, the effective pressure source from fission products in irradiated fuels is important in determining the likelihood of either (1) terminating the accident via fuel dispersal prior to disassembly or (2) early terminating of the disassembly by early fuel expansion prior to significant UO_2 vaporization. These data, at high temperature, do not exist. Baseline data have now been obtained for fresh UO_2 fuels throughout the range of hypothesized accident conditions. Current studies are concentrated upon obtaining time scales and effective pressure sources for irradiated fuels. To accomplish these goals, a series of SPR-III irradiated-fuel EOS experiments has been designed and preparations have been initiated. The first such experiment is scheduled for the second quarter of FY79.

In the past quarter, a series of preliminary EOS experiments using fresh UO_2 was carried out in the SPR-III. Experimental data are now available and analysis is beginning. Building on these experiments, the SPR-III series of irradiated-fuels EOS experiments is being designed. Neutronic and heat transfer calculations indicate that powdered samples with a radial filter (probably gold) will provide the best energy deposition profile. It is now anticipated that energy states from boiling to those states with several hundred atmosphere vapor pressures can be achieved.

A series of calculations has been performed to investigate the formation of CO gas due to interaction between fuel and the graphite liner used in all Sandia EOS experiments to date. The preliminary result is that CO formation is unimportant for Sandia electron-beam heated experiments and at most represents a small perturbation for the in-pile experiments. This is important because the high temperature Sandia experiments had been questioned due to potential CO contribution to measured pressures.

Finally, a calculation of rate effects due to nonequilibrium suppression of oxygen stoichiometry defects shows that such effects are apparently small on the prompt-burst timescale. These results were based on an analysis of data obtained on ACPR aerosol tests. The conclusion is that equilibrium thermodynamics is thus adequate for interpretation on prompt-burst timescale phenomena.

2. Fuel Dynamics

2.1 Fuel Disruption

The nature of and timescale for fuel disruption under loss-of-flow (LOF) conditions is of crucial importance in determining the sequence of an LOF accident in an LMFBR. Uncertainties in the reactivity ramp rate at disassembly are strongly affected, if not dominated, by the nature of initial fuel disruption. Dust cloud or froth formation would tend to disperse fuel axially leading to shutdown, while fuel swelling or fuel slumping both tend to exacerbate the accident severity. The data base to determine which conditions dominate is inadequate or nonexistent.

The Sandia fuel disruption (FD) task is aimed at determining the type of initial fuel disruption, as well as the rate of disruption, for both fresh and irradiated mixed-oxide fuels under prototypic LOF heating conditions.

The fuel disruption task has entered a second stage with the successful completion of the first (FD-1) series of experiments. In addition to providing unique fuel disruption data, results of this series indicated considerably larger swelling than had been previously predicted. Detailed neutronic and thermal analyses have now been performed for FD-1, and predicted fuel and clad temperatures are in excellent agreement with experimental data. For FISGAS, a new fuel swelling code (developed when existing codes could not explain the experimental results), the first stage of modeling is now complete as are detailed swelling predictions. Modeling of those experiments in which strong fuel disruption was the dominant response mode has commenced and will continue.

The second series (FD-2) of experiments has gone through preliminary design stage and is expected to provide a much better simulation of LOF heating conditions. As part of the second stage of its development, FISGAS will be employed to predict the swelling portion of fuel disruption in these experiments.

Thermal design analysis effort directed toward FD-2 experiment planning has defined the geometry for the experiment which will provide flat axial and radial profiles.

2.2 Transition Phase

Following the loss of initial geometry in a core disruptive accident, and assuming that neither early shutdown nor rapid hydrodynamic disassembly takes place, the accident enters the transition phase. The progression of the transition phase toward possible second recriticalities may strongly influence the severity of the accident; therefore, it is important to understand in detail the phenomena associated with this accident stage. Sandia work is currently directed toward the mechanics of fuel blockage formation since this defines conditions leading to recriticality.

The formation of fuel blockages by freezing is an important aspect of the transition phase since this phenomena controls the distance fuel penetrates through the upper core structure, and hence the amount of negative reactivity available for accident termination. Heat transfer between flowing molten fuel and ablating steel walls which ultimately controls fuel penetration distance is affected by transpiration as molten steel moves away from the solid wall and is ablated into the bulk flow. This effect was examined in greater detail this quarter. Expressions and descriptive equations are in Section 2.1 of the main text of this report.

The liquid-liquid ablation experiments currently underway facilitate the study of the mechanics of heat transfer during the melting of a wall by a turbulently flowing liquid. Initial experiments with Refrigerant-11 and ice were performed with the Re-11 simulating molten UO_2 and the ice simulating stainless steel.

Early experiments emphasized qualitative information. Later experiments, which will be reported as they are performed, will concentrate on more quantitative information. Three flow orientations are of interest: horizontal, vertical upward, and vertical downward. For all three orientations, two distinct regions can be clearly defined. Near the inlet there is a region of strong turbulence characterized by rapid melting and considerable entrainment of the water at the wall. However, beyond this is a downstream region where the exact behavior depends upon the flow orientation. In this region, there is minimal entrainment and a film is formed along the channel. This film dominates the heat transfer such that if these were real reactor materials the fuel would penetrate the upper core structure to the extent that the probability of a recriticality would be greatly reduced.

2.3 Initial and Extended Fuel Motion

The purpose of the Initial and Extended Fuel Motion (IEFM) Program is to investigate various phenomena associated with fast reactor initiating accidents such as a loss-of-coolant flow (LOF) and transient overpower (TOP) without SCRAM. In these hypothetical accidents, dispersive fuel motion is a major source of negative reactivity insertion. However, depending upon failure location, failure mode, and final fuel relocation, positive reactivity effects are also possible. Therefore, it is important to identify and model phenomena such as fuel motion inside the clad prior to failure, axial fuel-failure location, mode of cladding failure, fuel disruption modes, rate of dispersal, fuel plateout, and extended fuel motion into the blanket (potential for blockage). Data to support model development and verification of these phenomena are severely limited. Irradiated fuel experiments are currently being planned that will utilize the newly developed coded aperture fuel motion detection system currently being installed in the ACRR. Investigators hope that due to the considerably improved resolution of this diagnostic device, direct observations of these phenomena will be possible. These tests in the ACRR will require operating modes allowing preheats at nominal power followed by ramp, square wave, or pulse power profiles. The required hardware to provide these modes is being constructed. This capability is expected to be available in late FY79 or early in FY80. An additional facility needed for these experiments is a flowing sodium loop. Design of a small prototype loop for single fresh fuel pin tests is currently underway. Design of an advanced loop for larger irradiated fuel tests will begin in late FY79. Hot cell and fuel handling requirements are also being considered.

These experiments are somewhat complementary to those currently being performed in the CABRI reactor in France. Consequently, cooperative efforts are underway through the ACRR/CABRI exchange agreement to provide a continuing interchange of expected data and analysis results.

During this quarter, the preliminary design of a prototype in-pile flowing sodium loop continued with emphasis on reviewing the scope of the experimental program as related to loop design considerations. It appears at this point that a single-pass gas-driven loop would meet the requirements of early fresh fuel tests.

Work was initiated this quarter to implement hardware changes to the ACRR transient-rod drive mechanisms. These changes are required to support the addition of advanced operating modes. For the full spectrum of desired operations, it will be necessary to increase the motor drive speed by a factor of 2.5 and install a rod withdrawal programmer.

Calculations were performed to determine the feasibility of testing the CABRI common test pin in the ACRR under conditions similar to those of the CABRI reactor so that results could be compared. By suitable moderation, the ACRR can achieve a similar axial energy deposition profile within the test pin. As part of the CABRI program, EXPAND calculations were performed on TOP Tests A1, A2, and A3 with the August 1978 CABRI core design. Comparison will be made with other CABRI partners (France, Germany, Japan, UK) to determine consistency of the various analyses. Sandia calculations indicate that Test A1 will achieve approximately 27% area fuel melt without subsequent fuel failure. In Test A2, the pin will receive a 69% area fuel melt. Test A3 is predicted to fail with an area fuel melt of approximately 82%, but at a time (208 ms after the peak of the pulse) longer than a true simulation. Hence, it is doubtful, based upon these results, that the original test objectives will be met. Results of comparisons will be reported next quarter.

2.4 Fuel Motion Detection

2.4.1 In-Core Systems

The feasibility of in-core fuel motion detection is being investigated at Sandia because many facilities which can be used for NRC fast reactor safety tests do not have instrumentation slots. Also, in those reactors which do have slots, self-shielding may preclude the use of high-resolution techniques for large-scale tests. Consequently, 7-, 19-, and 37-pin experiments are being conducted in the SPR-III to test both detectors and unfolding methods. Following the completion of these experiments, fuel motion detection will be performed in the ACRR as part of prototypic accident situations generated during PBE experiments.

During this quarter the experiment plan and safety analysis report for the seven-pin fuel motion detection experiments was presented to and passed by the Sandia Safety Committees. After remaining required tasks are performed, it is hoped that the first fuel motion detection experiments can begin next quarter.

As part of an ongoing effort to develop fuel motion detection devices, several miniature ^{238}U fission-couple detectors were fabricated and successfully tested in SPR-III. Because of their small size and fast-neutron sensitivity, these detectors will be sensitive to fuel motion when placed close to the fuel.

The CABRI operating group has asked Sandia's assistance with energy deposition experiments to determine the time and spatially dependent energy deposition within a fuel pin subjected to a simulated fast-reactor accident. The accurate measurement of effects of control rods and transient rods upon the test fuel has been a continuing problem in CABRI. Actions are being taken to provide the proper assistance. Measurements in the reactor are planned to be taken in about a year.

2.4.2 Electron Beam Flash X-Radiography

The feasibility of using electron-beam x-ray cinematography for fuel and cladding motion detection in NRC reactor-safety testing facilities is being investigated at Sandia. This technology is being studied for its potential as a high-resolution, two-dimensional detection device for up to subassembly-size experiments.

Because the requisite source determination is of major importance to this task, most of the work during this quarter was devoted to optimizing the design of a state-of-the-art active detector system and the subsequent determination of its performance characteristics. Then, by coupling the performance capabilities of the detector system to the resolution requirements of the experimental program, the source requirements can be established.

The performance studies on the active detector system were carried out on a 10-MeV LINAC, necessitating the design and fabrication of electronic components in order to allow the active systems to synchronously drive the linear accelerator. Analysis of the data has not been completed and will be reported during the next period.

2.4.3 Coded Aperture Imaging

2.4.3.1 Introduction -- One of the main purposes of the Coded Aperture Imaging task is the study of imaging problems which will arise in large reactor safety experiments (involving more than seven fuel pins). Imaging in these large tests is expected to differ considerably from single- or seven-pin tests because of the significant scattering and absorption of the imaging radiation within the larger test fuel pin bundles, and the greater complexity of the image itself. Coded-aperture imaging of both gamma rays and neutrons is being studied.

2.4.3.2 Gamma-Ray Coded Aperture Imaging -- Gamma-ray coded aperture imaging technology is being developed in order to measure fuel motion in experiments involving up to seven fast reactor fuel pins on the ACRR. This development is proceeding satisfactorily, and it is therefore attractive to consider extending this technology to larger fuel bundles. In larger fuel bundles, there will be much greater absorption and scattering of the fission gamma rays used for imaging than in single- or seven-pin cases. This scattering and absorption will tend to reduce the signals from the center and back surface of the fuel bundle.

The Monte Carlo calculations for a 37-pin bundle are now complete and a topical report on the results has been prepared. It appears that removal of fuel from the center of the bundle can be detected; however, correlation with experiments will be necessary to obtain the exact mass resolution that can be achieved in the presence of realistic reactor backgrounds.

2.4.3.3 Fast Neutron Coded Aperture Imaging -- A major milestone was reached with the reconstruction of a fast neutron image of the ^{252}Cf source. This reconstruction is believed to be the first successful, high quality fast neutron image obtained by using coded aperture techniques. To achieve this result a new aperture design and improved image reconstruction techniques were used. Development of transient fast neutron detectors for use in an imaging system has now begun.

3. Core Debris Behavior - Inherent Retention

3.1 Molten Core Technology

If it is assumed that following a major reactor accident the core material debris is uncoolable, ultimately penetrating the reactor vessel, large quantities of molten core materials can come into contact with structural and containment materials. The interaction of the melt with these materials defines (1) the pressurization of the containment structure, (2) the radioactive aerosol production, and (3) the ability of the containment to prevent melt-through.

The previously observed destructive behavior of large quantities of molten materials with containment materials is the focus of this task. In addition, any core meltdown accident includes a phase during which the internal heat generation by fission products is insufficient to maintain the core materials in the molten state. The assumption that significant core debris/concrete interactions cease when the molten state cannot be maintained ignores the observed temperature ranges at which concrete melts. These temperatures are less than the solidification temperatures of core-melt constituents. A test (BURN 2) was performed this quarter to determine the gas evolution and erosion of concrete by hot solid core material.

The BURN-series tests are small-scale experiments also intended to develop instrumentation and techniques for the quantitative study of melt/concrete interactions. Test BURN 0 was designed to demonstrate a technique for producing melt interactions and utilized Joule heating to sustain a thermitically generated corium melt. Test BURN 0 failed because of limitations in the experiment equipment which did not permit rapid control of current flow between tungsten electrodes used in the test. Test BURN 1 successfully demonstrated an x-ray technique that allows real-time, continuous observation of a high-temperature melt in contact with concrete. Melt behavior, gas flow behavior, and concrete interfacial behavior were readily visible in this test, producing the first quantitative data obtained in such tests. Test BURN 2 demonstrated that core materials need not be molten to erode the concrete or to cause the liberation of substantial volumes of gas. Test BURN 3 was quite similar to Test BURN 2 except that the crucible was fabricated from CRBR composition concrete. Adequate modeling of the processes observed in Tests BURN 2 and 3 cannot be done at this time without improved data concerning upward heat fluxes. Data from Test BURN 3 suggest that the time variation of this upward heat flux is complex. The experimental and instrumental arrangements used in Test BURN 4 were quite similar to those used in Test BURN 3 except that the melt to be sustained in Test BURN 4 was generated metallothermically in a generator similar to that used in a previous test series. Events following the entry of the melt into the crucible resulted in expulsion of the melt, destruction of most of the instrumentation sensors, and termination of the experiment. As a result of these first four tests, a significant improvement was achieved in the quantitative data describing erosion rates and gas evolution for concrete-core melt interaction.

Future tests in the experimental program addressing molten core technology are discussed in the main text of this report in Section 3.1.

3.2 PAHR Debris Bed

Following a core disruptive accident, molten core materials may exit the core region and contact sodium where solid fuel debris will be formed and collected on horizontal surfaces within the vessel. This debris is still capable of generating significant power through the decay of fission products. Should insufficient cooling be afforded by natural processes, the debris could remelt and threaten containment. The purpose of this task is to determine the natural cooling of such debris. Three major first of a kind in-pile experiments have been performed at Sandia and have provided significant (and unexpected) data for modeling the behavior of debris beds.

The work this quarter has concentrated on the preparation of the fourth major experiment, D-4, and on the development of a model to describe the observed debris bed behavior and to be incorporated in the containment analysis code, CONTAIN. The sequence of events leading to remelt of a debris bed includes formation of a region within the bed in which sodium exists only in the vapor phase. This region is referred to as the dryout zone. A significant result of a previous debris bed experiment was the very lethargic behavior of beds during the dryout process. This observation is contrary to previous postulated behavior of immediate melt after dryout. As part of the effort to develop models, attempts are being made to describe the behavior observed during previous experiments. A one-dimensional synthesis of the bed thermal behavior during dryout shows that the temperature transients observed during previous experiments are due to increasing thickness of the dryout zone rather than to previously assumed thermal equilibrium of a rapidly formed zone. In addition, the analysis shows that the dryout zone is in approximate thermal equilibrium during its expansion. Vapor generation and the work of displacing the coolant upward absorb little energy during the dryout process; thus, dryout does not significantly alter the power transferred, only the mode of its transfer. The main result of dryout is the shortening of the convection flow paths in the region above the dryout zone, leading to a more stable hydrodynamic regime.

Significant improvement has been made, using the data of previous experiments, in the understanding of and ability to model the behavior of debris beds.

3.3 PAHR Molten Pool

In the assessment of postaccident heat removal possibilities, it is necessary to consider the case in which the debris formed by the hypothesized accident cannot be cooled and progresses to a molten state. Understanding the behavior of such pools is important to determine if a pool of given characteristics will be retained within engineered barriers and if not, what retention times are afforded by these barriers to permit reduction of decay heat and radiation levels.

The in-core molten pool experiments are aimed at the investigation of the progression to melt, the growth of the melt zone, and the short and long term behavior of internally heated melts of reactor materials. The studies will determine the thermal and kinetic behavior of the molten pools as well as the interaction of such melts with retention materials and will help define the probability and rate of vessel failure.

The first goal of the molten pool program has been to develop experimental hardware and accompanying diagnostics for in-pile tests in which heat flux and structural ablation can be studied with the use of real materials under typical temperature and heating conditions. Such tests had never been accomplished.

Three in-core experiments were conducted in the first molten pool series prior to the shutdown of the ACPR for upgrading. In the first fuel-only experiment, MP-1, the ultrasonic thermometry indicated fuel temperatures and axial temperature gradients which were similar to pretest calculations. In the second fuel-only experiment, MP-2, the on-line ultrasonic thermometry and posttest x-radiography indicated that a significant amount of fuel had melted. In experiment MP-3S, a 220-g stainless steel sample was melted by 628 g of overlying fission-heated UO_2 which reached 2673 K (2400°C) during the experiment. Thus, the three in-core experiments run to date have demonstrated the feasibility of in-pile tests, confirmed the operational capabilities of the experiment package design, and shown that fission-heating of enriched UO_2 to the desired "molten pool" temperatures could be achieved. Ultrasonic thermometry developed for this program has proved to be a valuable diagnostic of temperatures and temperature gradients up to the UO_2 melting point.

During this quarter, work continued in the development of diagnostics techniques. The evaluation of a continuously rotating ultrasonic thermometer sensor within a metallic sheath was conducted to improve the ultrasonic temperature measurements. Initial tests were conducted on an ultrasonic thermometer to be used to monitor in-pile the interface between liquid and vapor phases of sodium which will be a diagnostic of the vapor-blanketed volume of a debris bed during dryout. Previous high-temperature material interaction studies showed that particulate UO_2 and solid Harklase (a 98% MgO brick proposed as a core retention material) fuse in an inert atmosphere at 2848 K (2575°C) ±40 K, an effect which could influence the proposed use of MgO as a containment material. Detailed analysis of the thermal conductivity of a porous bed of particulate fuel was examined and a model was developed for use in describing heat transfer in dried-out debris beds, thus enhancing significantly the ability to model the transition from a solid debris bed to a fuel melt.

3.4 Fragmentation

Most severe accident scenarios for advanced sodium-cooled reactor systems involve the production of significant amounts of molten fuel and steel. The ultimate dispersal of this molten material often depends on either bulk freezing of the melt or the establishment of coolable particulate beds. Scenarios which differentiate between the dispersal modes involve questions of the fragmentation of substantial quantities of melt when contacted with coolant. Previous investigations yielding quantitative information involve very small quantities of fuel melt, leaving unanswered the question as to whether or not large quantities would yield different particulate size distribution due to vapor blanketing of the bulk stream. A knowledge of particle size distributions is crucial to the resolution of postaccident coolability of cores which have been reduced to rubble.

During this quarter, two experiments, FRAG3 and FRAG 4, using UO_2-producing metallothermic mixtures were performed to examine the fragmentation process in the 20-kg range. The fragments from the second fragmentation experiment, FRAG 2, were classified according to size. Some scanning electron microscope (SEM) examinations of the fragments were also made.

FRAG 4, a repeat of the unsuccessful FRAG 3 was run on August 28. Visual observations indicated a much milder interaction than those observed in previous experiments that used nonthermic mixture (i.e., steel-rich). Core samples of the debris revealed slightly varying bed thickness. Inspection of the bed indicated that the degree of size stratification of the fragments, an important effect in debris bed cooling, was far less than in previous, more energetic experiments.

Analysis of FRAG 2 results yielded a fragment distribution (classification structure reported in 3.5.3 of the main text) similar to that obtained in small-scale tests. Other results obtained thus far indicate that for 20-kg scale and the experiment conditions used, no scale effects are yet observed. The experiments have also demonstrated stratification of debris beds formed which, due to the resulting higher porosity, would lead to much more favorable conditions for natural cooling of debris beds.

3.5 Sodium Containment and Structural Analysis

In the event of vessel or pipe rupture, large quantities of liquid sodium at temperatures in excess of 873 K come into contact with concrete or other containment materials. This task is aimed at identifying and quantifying the dominant phenomena involved in the erosion and possible breach of containment and in the liberation of gas which may contribute to containment failure.

Any loop-type LMFBR system must account for the interaction of hot sodium with cell liners and, given either a failed liner or a Core Disruptive Accident (CDA), the interaction of hot sodium with concrete. The data base available for safety assessments involving these interactions is extremely limited, especially for the concrete and failed-liner interactions.

Concrete made with basalt aggregate to Fast Flux Test Facility (FFTF) mix design was tested during this quarter. Two tests were conducted: Test 11 and Test 12. Test 11 involved dumping 128 kg of sodium at 873 K (600°C) into a bare basalt concrete crucible cavity resulting in a 13.2-cm-deep pool. An energetic exothermic reaction started at about 75 min into the test. The reaction was sodium limited. This result is consistent with earlier observations in tests with limestone concrete. Side wall attack and cracking were more severe than had been seen with the limestone concrete.

The basalt concrete crucible cavity of Test 12 was lined with two layers of firebrick simulating the FFTF geometry. A mild steel insert was placed inside of the firebrick. The insert contained three preformed flaws to allow the liquid sodium to contact the firebrick. Sixty-eight kg of sodium at 873 K (600°C) were dumped into the steel insert for a sodium pool depth of 30.5 cm. An energetic exothermic reaction was observed between the sodium and firebrick. An additional dump of 45 kg of sodium was made about 4 hr into the test in an attempt to keep the test from being sodium-limited. In spite of this, posttest examination revealed that the test was sodium-limited in that all 113 kg of sodium had reacted with the firebrick. The concrete crucible side wall cracking was more severe than occurred in the bare cavity of Test 11. The insert bottom plate was bowed, in the direction of the cavity, about 4 cm. No radial distortion of the insert was noted. These results are in significant disagreement with DOE FFTF support work performed at HEDL. Although the Sandia theories appear to explain the results, the differences have not been fully resolved. Additional tests will be performed to resolve the difference between the DOE and NRC sponsored experiments.

4. Aerosol Source Normalization

During an energetic hypothetical core disruptive accident, fuel vapor may be produced which subsequently condenses to form small, very particulate debris (molten or solid) which can be transported to the upper vessel regions and through-breaks which may have occurred in the vessel. The possibility of transporting this material depends strongly on its initial character.

Aerosol produced from in-pile (ACRR) experiments is being characterized to determine the physical properties of fuel particles resulting from the vaporization and melt breakup of fuel pins subjected to simulated overpower excursions. The characteristics of these particles will be compared with those produced by out-of-pile experiments at ORNL which are part of the NRC sponsored aerosol transport program. Subsequent in-pile studies will examine the interaction of particles with the supporting structure and with sodium.

Design was completed on the second series of in-pile aerosol experiments and fabrication has begun on all components. The experimental canister provides for a vertically mounted fuel pin which allows simultaneous photographic viewing of the top and side of the fuel and for room to make a four-terminal measurement of fuel resistance. An in-pile pumping system was designed to maintain vacuum in the canister during temperature conditioning of fuel by resistive heating or by programmed pulsing in the ACRR. The total distribution of particle mass as a function of particle size is reported from the Series I experiment. Fuel vapor accounts for about 30% of total mass and about 60% of the mass is in particles larger than 1 μm. The out-of-pile aerosol source experiments are scheduled at ORNL for December or January. These tests will use similar diagnostics to those developed for the ACRR experiments.

5. Containment Analysis

This task is directed toward developing a total containment systems code (CONTAIN) which will analyze a variety of possible accident sequences, beginning at the point of a disrupted core debris bed to the definition of the radiological release term in the event of multiple containment failure. Core-melt accidents, energetic disassemblies, reactor vessel rupture, and large-scale sodium spills are addressed. Existing containment models are being adapted where feasible and new models are being developed in areas where suitable models do not exist. These new models are being supported by the test program described in previous sections. Major phenomenological factors are (1) postaccident heat removal; (2) debris melt; (3) vessel failure; (4) concrete-sodium interactions; (5) concrete-melt interactions; (6) melt-sodium interactions; (7) liner response; (8) sodium pool/spray burning; (9) chemical reaction products and kinetics; (10) gas flow, pressurization, and venting characteristics; (11) heat transfer (pool/wall/atmosphere); (12) fission product chemistry and inventory; (13) aerosol transport behavior.

During this quarter, the program has been directed toward continued review and evaluation of phenomenological models for the CONTAIN code. The development of melt-sodium-concrete interaction models has also continued. The development review of individual phenomenological models have been done in the context of the two primary submodels for CONTAIN (Cavity Debris Pool/Material Interactions Model) and the cell atmosphere model (sodium burning, aerosol, and heat transfer model).

A significant part of the effort involved improvements to the concrete thermal response model in anticipation of incorporating this model into the code. Mass transfer routines for both the wet and dry regions of concrete for the sodium-concrete interaction case have been developed and incorporated. An improved algorithm for treating boundary conditions for the energy equation at ablating surfaces has been programmed and inserted into the code, as has a subroutine to calculate temperature-dependent Darcy coefficients.

To minimize the problems associated with modeling fluid flow for CONTAIN, a steady-state solution of the mass transport equations has been formulated and is being programmed. The initial version of the cavity debris pool model, based on the existing melt-concrete interaction code, INTER, has undergone considerable revision to allow treatment of sodium as a pool component in the layered structure. This revised version has been restructured into a more modular code with improved heat transfer and layer structures. For the cell atmosphere model, generalized implicit heat transfer routines have been written and incorporated into a cell description allowing arbitrary specification of materials and cell liners. Sodium burning models have been modified for incorporation into CONTAIN. Reviews are progressing with the objective of refining and enhancing the accuracy of the code.

6. Elevated Temperature Design Assessment

The primary objectives of the elevated-temperature design assessment studies are (1) to develop correlative NDE techniques that can be used to monitor progressive creep, fatigue, and combined creep-fatigue damage in materials used in advanced reactor primary- and secondary-loop components; (2) to evaluate analytical methods (and correlate with experimental data) for creep buckling of advanced-reactor components operating at elevated temperatures; and (3) to design, fabricate and operate a multiaxial creep-fatigue facility for the purpose of evaluation of creep-fatigue damage rules.

6.1 Creep-Fatigue Test Program (Uniaxial Loading)[*]

6.1.1 Creep-Testing

A creep test (316-C-7) was terminated short of failure after 2,204 hr at 27,500 psi. This specimen and a previous test specimen (316-C-5) will be checked by positron annihilation (PA) to evaluate the sensitivity of this method of assessing creep damage.

6.1.2 Creep-Fatigue Testing

Three additional creep-fatigue tests were completed. One test (316-MTF-12) with a compressive hold period resulted in visual evidence of surface cracking at 1680 cycles and numerous large cracks at the conclusion of the test (3000 cycles). The number of cycles to failure for both the tensile and compressive hold period tests was equivalent. This conflicts with previous data. Another test will be conducted to verify the results.

A series of fatigue tests was initiated to provide specimens for multiple sequential surface PA measurements as a function of the number of cycles at five different strain ranges.

---

[*] All testing is performed on Type 316 Stainless Steel.

6.2 Nondestructive Examination

A series of PA measurements was initiated to determine the species of defects (vacancies, dislocations or precipitates) which contribute to the observed increase in PA lineshape parameter produced by either cold work or low and elevated temperature fatigue. Both vacancies and dislocations are produced during deformation, and it is important to understand their relative contributions to the total PA measurements. A better understanding would help explain the lower lineshape parameters measured at cyclic saturation for elevated temperature fatigue compared to room temperature fatigue. This effort is continuing. These studies are aimed at evaluation of PA as a viable NDE technique.

6.3 Microstructural Analysis

Transmission Electron Microscopy (TEM) observations have been completed on samples fatigued at low strain ranges at room and elevated temperatures. Large variations in dislocation substructure are seen from grain to grain within a single sample for both high- and low-temperature fatigue. These variations make it difficult to generalize a single description of a sample. Observations from these tests will continue. Details will be reported in a future topical report.

6.4 Multiaxial Test Facility

All of the equipment for the multiaxial test facility has been received by Sandia, and the system was checked out and calibrated by the manufacturer. Testing of specimens under axial load and internal pressure will begin in the next quarter.

6.5 Creep-Fatigue Damage Analysis and Analysis of Piping Elbows

6.5.1 Creep Fatigue Damage Analysis

Design of a tubular test specimen to be used in the multiaxial test facility continued. The specimen is not supposed to buckle and the analyses were directed toward this purpose. The preliminary analyses were completed, and a set of operational curves as a function of temperature is being developed.

6.5.2 International Benchmark Activities

Participation was begun in the international calculational benchmark project of the Pressure Vessel Research Committee (PVRC) of the Welding Research Council.

6.5.3 Creep Buckling of Piping Elbows

Investigations were performed to determine differences in behavior of several types of creep laws when applied to the analysis of piping elbows. Two power laws were used to model the piping elbow. The simple Norton power law was more efficient, but the more complex Blackburn power law was more accurate. This area needs more investigation. This, and the results of other calculations will be presented in a forthcoming topical report.

7. LMFBR Accident Delineation

The principal objective of this program is to determine the applicability of event tree methodology to all phases of LMFBR accidents. The results of the study are intended to (1) provide a demonstrated methodology for developing accident sequence diagrams for an LMFBR, (2) identify and systematize the key phenomena and phenomenological or system uncertainties in the accident sequences, and (3) illustrate the methodology by determining the dominant accident sequences.

Over the past year, Sandia Laboratories initiated the LMFBR Accident Delineation Study to examine the applicability of event tree methodology to the representation of fast reactor accident sequences. This project was a broad effort to review and evaluate available information on LMFBR accident sequences and to construct event trees delineating these accident sequences from accident initiation to radiological release from the containment. Qualitatively the event tree methodology utilized here is similar in most respects to that demonstrated in WASH-1400 and the CRBR safety study.

During this quarter, the draft Interim Report was completed and made available for extended review. The Interim Report presents event trees which were developed in three interacting but relatively distinct areas corresponding to Accident Initiation, Accident Phenomenology, and Postaccident Phenomenology.

In the Engineering Systems area, key systems or subsystems were identified as involved in accident initiation for a three-loop LMFBR. Because of limitations to date, the study emphasizes potential accidents involving the core during full-scale operation. Examining 4 basic reactor systems, 14 basic subsystems are identified as involved directly with control, generation, and transfer of heat. Accident "initiators" have been defined, consistent with these 14 basic subsystems, which if not appropriately mitigated by Engineering Safety Systems, can escalate into a core disruptive accident. The systems approach to accident initiators leads to a set of event trees representing a way to identify and evaluate initiation sequences.

In the Accident Phenomenology area, the event tree methodology proved useful in information organization and in representation of remaining uncertainties. Two limitations imposed on the methodology must be assimilated, however. First, some of the most important event tree branch points represent phenomenological uncertainties complicating the interpretation of tree quantification. Second, event tree formalism is not well suited to resolving complex questions involving a continuous range of values rather than just one or two. This work dramatically illustrates the significant uncertainties in knowledge of the controlling phenomenology in many accident sequences. Work on Accident Phenomonology continues in the effort to solidify the usefulness and applicability of event tree to accident analysis.

The Postaccident Phenomenology area is an attempt to outline the major cause and effect relationships in an accident sequence following a CDA. After defining the physical components of the containment system, event trees were devised to address the postaccident sequence. Four major areas of uncertainty were identified as requiring resolution. These areas are (1) debris bed coolability; (2) vessel head damage and quantity of sodium ejected in relation to CDA energetics; (3) chemistry and reaction kinetics of sodium and fuel debris attack on reactor cavity materials; and (4) response of the upper Reactor Containment Building to the introduction of sodium vapor, fission products, and hydrogen from the Reactor Cavity. Within these areas, significant improvement in understanding is anticipated in the near term. In particular, debris bed coolability is important to understand in order to better assess priorities of phenomenological questions. Additional analysis is still foreseen as necessary.

The event trees developed at this interim stage represent only a first step in an iterative process of accident delineation and ultimately risk quantification. Further development in all areas of accident description has been recognized as being necessary and useful.

8. Test and Facility Technology

8.1 ACPR Upgrade (ACRR) - Initial Test and Operations

After achieving criticality last quarter, the Nuclear Startup Tests were continued and completed this quarter. The approach to full Power Tests was initiated. Full steady-state power of 2 MW(t) was achieved on July 27, 1978 followed by a period of instrumentation modifications and adjustments, dosimetry and a complete power and temperature mapping of each element in one-sixth of the core. The pulse series was initiated with achievement of a maximum single pulse with a reactivity insertion of $2.95 on August 18, 1978. The multiple pulsing mode and the transient rod withdrawal mode were also characterized.

8.2 ACRR Fuel-Motion Detection Systems

A coded-aperture fuel-motion detection system is under development for the ACRR. The design of the system has been based upon the experience gained in experiments with shielding, collimation, coded-aperture development, and time-resolved pseudoholography at the ACPR, SPR-II, and ^{252}Cf facilities. The systems have been designed for high spatial and temporal resolution measurements of fuel motion in both transient and steady-state experiments, including bed-leveling and material-separation studies in the postaccident heat removal experiments. If successful, the system should provide three-dimensional images of fuel under simulated accident condition with both high spatial and temporal resolution.

The design of the system has been completed and most of the major components were received this quarter and are being checked and fitted together. The shield structure will be assembled first in the laboratory, and then will be reassembled in the reactor during October. Radiation background measurements and steady-state proof tests will begin shortly thereafter.

8.3 Large-Scale Test Assessment

Large-scale test assessment efforts are directed toward the definition of an experimental program such that test data obtained have the potential to confirm analysis and conclusions drawn from smaller scale experiments as related to CDAs. These considerations include the use of existing facilities as well as the definition of requirements for new facilities or modifications to existing ones.

A data base for LMFBR safety analysis should be established to accommodate design studies for test facilities in which key safety issues can be resolved. The facility designs are dependent upon various parameters of the tests planned to resolve these key safety issues. Identification of the major safety issues and programs to resolve them are now in progress.

LMFBR safety tests include small-scale phenomenological tests in- and out-of-pile and large-scale prototypic experiments to address Transient Overpower (TOP), Transient Undercooling, Transition Phase, Disassembly Phase, Energy Partition, Postaccident Heat Removal (PAHR), Extended Material Motion, and Radioactive Material Transport.

Analytical support of the international fast reactor safety exchange program continued.

BLANK PAGE

ADVANCED REACTOR SAFETY RESEARCH PROGRAM
QUARTERLY REPORT

1. ENERGETICS

1.1 Prompt Burst Energetics (PBE) (K. O. Reil, 4423; M. F. Young, 4425; J. T. Hitchcock, 4424)

1.1.1 Introduction

Prompt Burst Energetics (PBE) experiments are designed to provide information on the energetic response of various reactor fuel-clad-coolant systems to superprompt critical excursions. This program is directed at identifying and characterizing phenomena, resulting in pressure generation and the conversion of thermal energy to work. These experiments examine integral effects of fuel-clad-coolant interactions, fission gas release, and fuel and fission product vapor pressures during superprompt critical core disruptive accidents. The experimental work is closely interfaced with analytical modeling efforts to develop models which uniquely describe the observed phenomena for incorporation into predictive accident analysis. These experiments also provide information about the thermodynamic states and spatial distribution of fuel, clad, and coolant following a superprompt excursion. These data serve as initial conditions for postaccident heat removal (PAHR) studies.

In tests performed to date, single fuel pins were pulse-fission-heated in the Annular Core Pulse Reactor (ACPR) to temperatures resulting in fuel vaporization. The pins, which have been surrounded by helium or sodium, are contained in a rigid pressure vessel which is instrumented with thermocouples and pressure transducers and which is fitted with a movable piston at its upper end. Estimates of the conversion of thermal energy to work result from comparisons of the kinetic energy of the piston to the fission energy input to the fuel. Pressure, temperature, and piston displacement histories are determined for a variety of fuel-coolant systems and initial conditions. A series of experiments with fresh uranium dioxide fuel and sodium coolant has been completed. Initial experiments with fresh uranium carbide fuel and sodium have been performed. Future experiments will examine fission product effects in preirradiated fuel. A seven-pin test vehicle for PBE experiments is under development.

During this quarter, activities were directed toward the analysis of completed experiments and completion of a topical report describing the fresh oxide/sodium PBE experiments. Preparations for upcoming experiments are also in progress. Modeling of the sodium pressurization arising from deceleration of the piston was performed for experiment PBE-9S. As in the experiment PBE-SG2, the amplitude of the deceleration pressure in the upper sodium slug was found to be small compared to the pressure transient observed coincident with piston stoppage. These results support the conclusion that the observed pressure transient resulted from an FCI triggered by the hydrodynamic pressurization.

The EXPAND pin failure modeling was extended to the double pulse oxide experiments. The results predicted no failure for experiments PBE-3S, -8S, and -10S and in fact, no failures were observed. For experiments PBE-9S, failure by stress rupture was predicted to occur about 9.6 ms after the power peak. When experiment PBE-9S was run, a pressure transient (indicating pin failure) occurred approximately 1.8 ms before the power peak. The observed difference in predicted and experimental timing (approximately 11.4 ms) for experiment PBE-9S is much larger than corresponding differences between experiment results and EXPAND predictions for other PBE experiments. Further, the energy input at 1.8 ms before the power peak is not sufficient to melt a 20% enriched pin in experiment PBE-9S. Possible explanations for these discrepancies are being investigated and include the possibility that the test pin was of a much higher fuel enrichment than 20%.

At the request of the staff at HEDL, EXPAND was used to predict pin failure in the pending UC-fuel TREAT experiment AX-1. Clad failure was predicted to occur about 90 ms before the peak-of-the-power transient.

Estimates of the work potential in the oxide/sodium experiments were derived from the measured pressure histories. Results show substantial agreement with results derived from measured piston motion for those experiments in which piston motion reflected the entire pressure history. For experiments PBE-9S and -12S, in which the pistons moved full travel and stopped while the channels were still pressurized, greater energy conversion efficiencies were estimated from the pressure integral analysis. These estimates yielded a maximum value of 0.54% for experiment PBE-9S.

Postirradiation examination of the oxide experiments is continuing. Examination of experiment PBE-7S is nearly complete. Work has begun on experiment PBE-12S.

Preparations for upcoming experiments are continuing. These preparations include modification and expansion of the data acquisition system, the procurement of fuel and experiment components, and detailed experiment planning and safety analysis.

1.1.2 PBE Analysis

1.1.2.1 Piston Stopping Effects -- A coincidence has been observed between the stopping of the piston and a secondary pulse on the top pressure transducer in several experiments. In experiment PBE-9S, the secondary pulse was approximately 30 MPa. It was hypothesized that this was an FCI triggered by a pressure pulse in the top sodium slug generated by piston deceleration.

A calculation was done by using HONDO,[1-1] a transient finite deformation code, to determine the magnitude and duration of the pressure pulse caused by piston stoppage. The piston, deformable sleeve, and sodium column were modeled as in Figure 1.1-1.

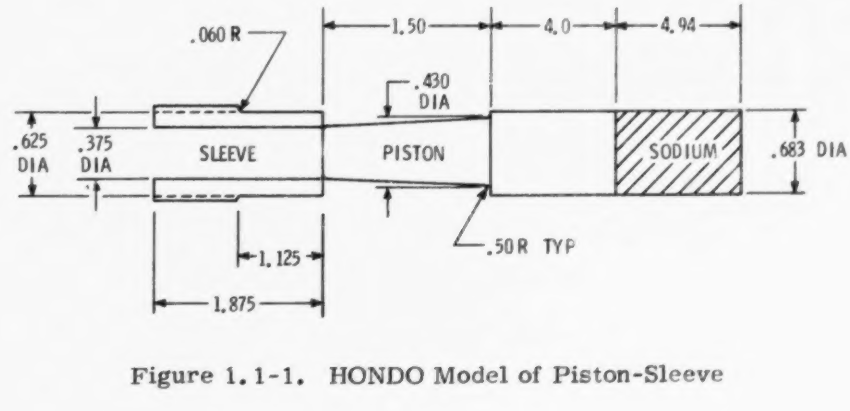

Figure 1.1-1. HONDO Model of Piston-Sleeve

Mechanical properties for the piston (Mallory M-1000 tungsten alloy) were evaluated at a temperature of 773 K, and mechanical properties for the sleeve (4130-D4 stainless steel) were evaluated at 593 K. The sodium slug was assumed to be at 773 K and to have a mass of 21 g. An initial velocity of 13.8 m/s was used. This velocity is the same as that observed in experiment PBE-9S. This piston-sodium slug was calculated to stop in 0.55 ms and to travel 0.54 cm into the sleeve. The distance actually traveled in the experiment was 0.8 cm. The bulk pressurization of the sodium slug is summarized in Table 1-I and shows pressure and pulse width at half maximum at several distances from the piston face. The pressure falls off linearly with distance, becoming zero at the end of the sodium column.

Table 1-I

Sodium Pressure at Several Distances from Piston Face

Peak Bulk Pressure (MPa)	Distance From Piston Face (cm)	FWHM (ms)
4.7	2.51	0.32
2.7	6.27	0.37
*1.8	8.78	0.38

*Peak occurs at 0.45 ms

The last entry (8.78 cm) is closest to the pressure transducer location. Comparison of the bulk pressure due to deceleration (1.8 MPa) to that recorded by the pressure transducer (32 MPa), shows that the piston stoppage is sufficient to generate a trigger pulse, but is not enough to account for the recorded pressure. Together with the absence of fuel vapor pressure at this time in the experiment, this strongly indicates the presence of an FCI. Recent work by Patel and Theofanus[1-2] in liquid-liquid systems gave an estimate of the trigger pressure necessary to cause vapor explosions in the Na-UO_2 system as around 4 MPa, of the same order as that caused by piston stoppage in PBE-9S. The pressure pulse calculated by HONDO for PBE-9S at the top transducer location is shown in Figure 1.1-2. Figures 1.1-3 and 1.1-4 show the piston velocity and displacement respectively.

Figure 1.1-2. Sodium Pressurization

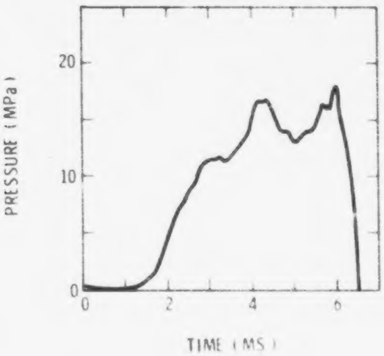

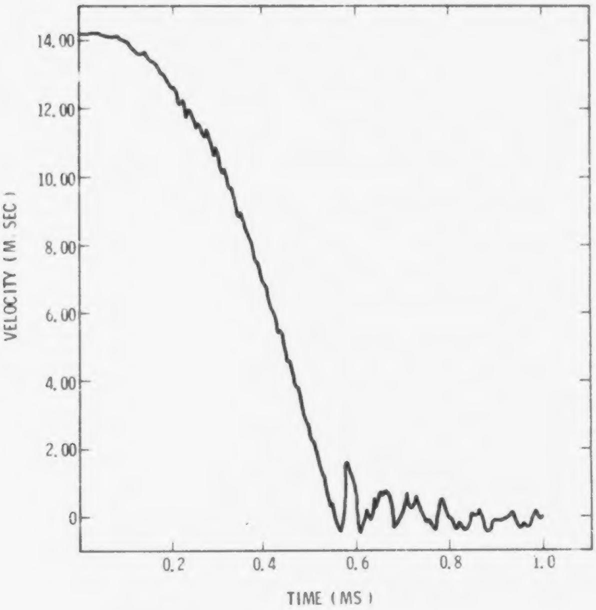

Figure 1.1-3. Piston Velocity

Figure 1.1-4. Piston Displacement

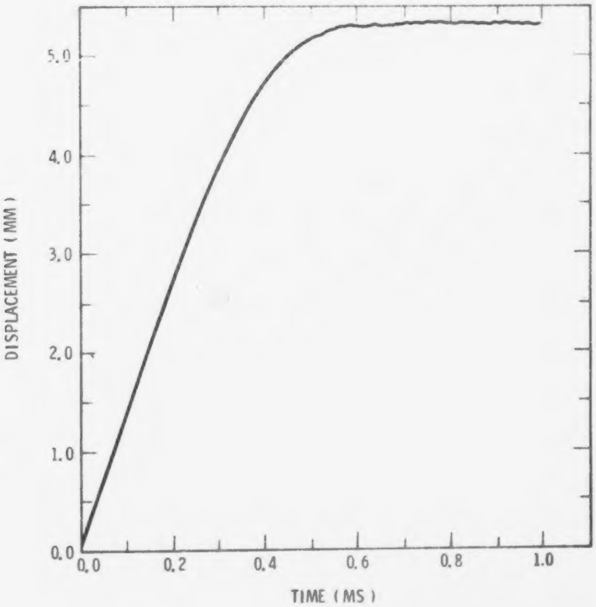

The top pressure histories recorded in PBE-5S, -6S, and -7S display pressure transients having amplitudes of 1 to 2 MPa, occurring coincident with the piston stoppage. These transients were apparently not sufficient to trigger FCI's in those experiments, but their occurrence supports the validity of the HONDO analysis.

In PBE-12S, the observed transient (coincident with piston stoppage) was approximately 4 MPa. This amplitude is greater than the calculated bulk pressure due to piston deceleration. The piston velocity in PBE-12S was approximately the same as the velocities measured in PBE-5S, -6S, and -7S. However, because of differences in the PBE-12S experiment geometry compared to the other experiments, the mass of the moving sodium (and fuel) column may have been greater in PBE-12S. Thus, it cannot be concluded that the coincident pressure maximum in PBE-12S resulted from a triggered FCI rather than from bulk pressurization of the sodium upon deceleration.

1.1.2.2 Pin-Failure Modeling of Double-Pulse PBE Experiments -- The EXPAND pin model[1-3] was used to calculate the double pulse UO_2/Na experiments PBE-3S, -10S, -8S, and -9S. Table 1-II compares EXPAND results and experimental data for these tests.

Table 1-II

Comparison of EXPAND Results with Experiment

PBE Case	Total Energy Deposition (J/g)	Failure (1) Time (ms)		Energy in at Failure (J/g)		Pressure at Failure (MPa)	
		A	B	A	B	A	B(2)
3S	2180	None	None	-	-	-	-
10S	2530	None	None	-	-	-	-
8S	2580	None	None	-	-	-	-
9S	2680	9.6	-1.8	1860	985	4.4	53.9
9S (50%)	3520	1.6	-1.8	1770	1290	5.0	53.9
9S (93%)	3870	-2.0	-1.8	1314	1420	1.8	53.9

---

(1) Referenced to main power peak
(2) Measured at lower pressure transducer
A = EXPAND calculation
B = Experimental result

The experimental results showing no failure were duplicated in experiments PBE-3S, -10S, and -8S. Experiment PBE-8S came closest to failure according to experimental results which indicated that the pin was severely distorted. The life fraction calculated by EXPAND for PBE-8S was 0.78. Experiment PBE-9S was predicted to fail at 10 ms after the power peak, considerably longer than the experimental time of -1.8 ms.

The EXPAND results for experiments PBE-3S, -10S, -8S, and -9S are summarized in more detail in Table 1-III. The failure times in parentheses are the result of varying energy deposition by ±5%. Varying the energy deposition by ±5% for experiments PBE-3S and -10S produced life fraction integrals from 0.0001 to 0.02 and no failure. PBE-8S failed at 58 ms for the +5% case. PBE-9S exhibited an asymmetric behavior, that is, a 5% increase in energy produced a 3-ms decrease in failure time , but reducing energy input by 5% resulted in a 50-ms increase. This difference is due to the fuel surface melting in the +5% cases increasing heat transfer to the cladding and resulting in early failure whereas in the -5% case there was no melting. If the fuel surface does not melt, the normal contact resistance and gas conductance are assumed for the clad-fuel gap, hence much less heat is transferred and the clad fails much later.

In PBE-8S, molten fuel did not contact the clad even for the +5% case; 51% of the fuel at the hottest node was at the solidus. The Larson-Miller parameter (LMP) life fraction rule predicted failure over a large fraction of the pin length (33%) again indicating that the PBE-8S pin was on the verge of failing.

Table 1-III shows that experiment PBE-9S had an average energy deposition (radial average at the axial peak) of 985 J/g at the experimental failure time. This is not enough to even melt the fuel (maximum calculated temperature was 2845 K). An anomaly, therefore, exists about clad failure at the indicated experimental time. Possible explanations for the observed behavior are being investigated. The most plausible explanation is that the fuel pin used in experiment PBE-9S was more than 20% enriched. Since 50% and 93% enriched fuel pins were fabricated at the same time as the 20% enriched pins, the energy deposition resulting from those enrichments was modeled for PBE-9S with EXPAND. The EXPAND results are shown in the last two lines of Table 1-II. Note that the 50% enriched case yields better agreement with experiment results than does the 20% result and the 93% enriched case yields very good agreement except for the pressure comparison. A mass spectrographic analysis of debris from experiment PBE-9S will be performed to verify the fuel enrichment.

Table 1-III

EXPAND Results

Case	Failure Time(1)	Pin Pressure at Failure (MPa)	Maximum Clad Strain (%)	Average Clad Temperature at Failure (k)	Energy Deposited to Failure (J/g)
3S	Life fraction = .001	-	0.5	-	2180
10S	Life fraction = .0002	-	1.3	-	2530
8S	Life fraction = 0.78 (58.1 - 00)(2)	-	8.6	-	2580
9S	9.6 (7.0 - 60)(2)	4.4	3.3	1135	1860

---

(1) Referenced to main power peak

(2) Energy varied ±5%

1.1.2.3 Experiment AX-1 Precalculation -- At the request of HEDL, a precalculation of the AX-1 experiment was done using EXPAND. This experiment involves three fresh He-bonded UC pins in the MARK-III sodium loop irradiated in the TREAT facility. The radial energy deposition profile in the pins is skewed due to the three-pin bundle geometry, so calculations were done for the highest peak/minimum ratio (facing can wall) and the flattest (facing center of bundle). The pins were predicted to fail at 87 ms before the power peak for Node 1 (facing center) and at 99 ms for Node 4 (facing wall). Both failures were burst ruptures due to thermal stress in the clad induced by molten fuel contacting the clad wall.

The failure criterion used was the LMP and life fraction rule. UC vapor pressure at failure was low; pin pressure was 0.4 MPa due almost entirely to fill gas. Note that the FWHM for this transient is 240 ms, considerably slower than the prompt burst regime EXPAND was designed to simulate.

1.1.2.4 Application of SIMMER-II to PBE Analysis -- Sandia staff members started investigating the applicability of SIMMER-II[1-4] to the post-pin-failure analysis of the PBE experiment series. Specifically, the goal is to use SIMMER-II to predict pressure generation and subsequent conversion of thermal energy to work in the experiments. Because SIMMER was written primarily to evaluate whole reactor problems on a macroscopic basis, difficulties are expected in modeling the single pin experiments.

During this reporting period, analysis of the PBE-5S experiment began. This experiment has been the subject of other modeling work.[1-3, 1-5] The initial model formulation surfaced several problems with the numerics in SIMMER. Work is currently underway to evaluate modeling approximations to eliminate these problems.

1.1.3 Pressure Integral Analysis

For the fission energy deposited in the fuel pin, estimates of the fraction that was converted to work can be derived from the measured piston motion.[1-6] The pistons in several experiments (PBE-9S, -12S, -SG1, -SG2, and -SG3) were observed to move full travel and to stop while the channels were still pressurized.[1-7, 1-8] Thus, the energy conversion ratios derived from piston motion do not reflect the total work potentials of those systems.

Estimates of piston kinetic energy and energy conversion ratio can be derived from integrals of the pressure histories. The impulse applied to the piston can be estimated from the pressure history measured at the top of the capsule as:

$$I(T) = A \int_0^T \Delta p(t)dt$$

where

$I(T)$ = impulse
A = piston cross-sectional area
$\Delta p(t) = P(t) = Po$
$P(t)$ = measured pressure history
Po = original system pressure $\simeq$ pressure behind piston.

(The pressure behind the piston is assumed to be a constant. Since the volume above the piston is large compared to the piston displacement, this assumption is approximately correct.)

Since the impulse represents a change in momentum, the velocity, V(t) of the piston can be estimated as:

$$V(T) = \frac{1}{M}\left[I(T)\right]$$

where M is the piston mass.

The piston kinetic energy, KE(T), is derived from the pressure integral as

$$KE(T) = \frac{1}{2M}\left[I(T)\right]^2 .$$

The energy conversion ratio is then estimated as

$$R = \frac{(KE)}{E}$$

where KE is the maximum derived kinetic energy and E is the total fission energy deposited when KE(T) achieves its maximum.

The results of this analysis for the PBE oxide/sodium experiments are summarized in lines 1 through 4 of Table 1-IV. Lines 5 through 8 of the table summarize the results derived from the measured piston motion. Comparison of the values of piston velocity and kinetic energy derived from this analysis with the measured values shows very good agreement among experiments PBE-4S, -5S, -6S, and -7S. (The integral for PBE-11S could not be evaluated because of a lack of resolution for the top pressure history.) The small, apparently systematic, differences among the results from the four experiments may arise from slight differences in pressures at the piston face and at the transducer location. For experiment PBE-12S the derived kinetic energy is approximately 50% greater than the measured value. For experiment PBE-9S, the estimate of the kinetic energy derived from the pressure integral is nearly 15 times greater than the measured value. This translates into a thermal to mechanical energy conversion ratio of 0.54% for experiment PBE-9S.

Table 1-IV

Energy Conversion Results for PBE Oxide/Sodium Experiments

	PBE-4S	PBE-5S	PBE-6S	PBE-7S	PBE-9S	PBE-11S	PBE-12S
1. Maximum pressure integral (kPa · S)	9.0	19.6	16.3	16.3	98.3	-	22.2
2. Derived piston velocity (m/s)	4.9	10.6	8.7	8.8	53.2	-	12.0
3. Derived piston kinetic energy (J)	5.2	24.5	16.4	17.0	613.	-	31.4
4. Derived energy conversion ratio	$5.1\text{x}10^{-5}$	$2.0\text{x}10^{-4}$	$1.25\text{x}10^{-4}$	$1.28\text{x}10^{-4}$	$5.4\text{x}10^{-3}$	-	$2.9\text{x}10^{-4}$
5. Maximum measured piston velocity (M/S)	5.4	11.4	9.8	9.2	13.8	2.2	9.8
6. Measured piston kinetic energy (J)	6.4	28.5	20.8	18.5	41.5	1.0	20.9
7. Total energy deposited at peak piston momentum (kJ)	102.4	123.1	131.2	132.4	98.9	107.7	107.9
8. Measured energy conversion ratio	$6.3\text{x}10^{-5}$	$2.3\text{x}10^{-4}$	$1.6\text{x}10^{-4}$	$1.4\text{x}10^{-4}$	$4.2\text{x}10^{-4}$	$9.4\text{x}10^{-6}$	$1.9\text{x}10^{-4}$

Note that computation of the pressure integrals after piston motion is complicated by the thermally induced transients in the pressure transducers. Thus, some uncertainties are introduced in the analysis. Note also that the system boundary condition changes when the piston stops, clearly affecting the measured pressure histories.

1.1.4 Postirradiation Examinations

Postirradiation examination (PIE) of experiment PBE-7S is nearly complete. During this quarter, an additional glove box containing a sectioning saw was reconditioned and modified to permit longitudinal sectioning of segments (4 to 10 cm long) cut from fuel pin housings. This equipment was subsequently used to section the top two segments cut from the experiment PBE-7S. These segments contain fuel and clad debris frozen along the plenum portion of the pin.[1-9] While the examination of those segments is not yet complete, several observations have been made. Partial melting of the cladding is observed in the plenum region due to freezing of fuel debris outside the clad. The structure that appears in radiographs to be intact cladding at the top of enriched fuel column is in fact a thin fuel annulus apparently formed as molten fuel froze against the inside of the cladding. The cladding subsequently melted off. Experiment PBE-7S postirradiation examination (PIE) will be completed next quarter.

The disassembly of experiment PBE-12S has been initiated with sectioning of the fueled portion. This work will continue next quarter.

The PIE of the carbide series experiments (PBE-SG1, -SG2, and -SG3) is awaiting completion of the large, inert-atmosphere, glove-box facility which should be available in Spring 1979.

1.1.5 Status

The topical report entitled Prompt Burst Energetics Experiments: Fresh Oxide/Sodium Series, SAND78-1561, was published in September. It contains experimental results and pin-failure analysis for the experiments PBE-1S through PBE-12S.

The application of EPIC[1-10] and SIMMER-II to the post-pin-failure analysis of PBE experiments will continue. The safety analysis and development of experiment plans for upcoming experiments will be completed, and safety reviews will be initiated during the next quarter.

The additional instrumentation and data acquisition equipment, including a second FM tape recorder, amplifiers and other components, has been received. The data acquisition system is being reconfigured with the new equipment to provide for the logging of up to 28 channels of analog information. New signal cable busses are being installed between the ACRR control room, Hibay, and Lobay facilities and to the Sandia Data Acquisition and Display System (DADS) computer.

Procurement of experiment components is continuing with no significant problems. Fuel pins and pressure transducers are to be delivered in early December. The response of the pressure transducers to transient mechanical loadings which are encountered in PBE experiments will be evaluated during the next quarter.

1.2 Equation-of-State (E. Bergeron, 4425; W. Breitung, 4425; J. Odom, 4424; D. A. Benson, 5534)

1.2.1 Introduction

Equation-of-state (EOS) represents a crucial relationship among materials in the determination of HCDA energetics in advanced reactors. In particular, the effective pressure source from fission products in irradiated fuels is important in determining the likelihood of either (1) terminating the accident via fuel dispersal prior to disassembly or (2) the early terminating of the disassembly by early fuel expansion prior to significant UO_2 vaporization. Baseline data has been obtained for fresh UO_2 fuels. Current studies are concentrated upon obtaining time scales and effective pressure sources for irradiated fuels. To accomplish these goals, a series of SPR-III irradiated-fuel EOS experiments has been designed and preparations have been initiated. The first such experiment is scheduled for the second quarter of FY79.

This report discusses the current status of the SPR-III experiments, neutronic design considerations, and analytical studies of a related set of aerosol source experiments. These activities collectively are intended to determine the potential importance of EOS rate effects during core disassembly. Under active analytical investigation, though not discussed in detail, are the equilibrium EOS of irradiated fuels, especially the potential influence on reactor time scales exerted by various fission product contributions to the vapor pressure.

1.2.2 Experiments

A series of vaporization experiments with prototypic fuels is in progress to determine the extent and rate of fission product release under prompt burst heating conditions. These tests are using the SPR-III reactor facility and fuel from the PNL-10 series of pins preirradiated in EBR-II. Since the SPR facility has not previously been used for high fission density experiments, a complementary program of experiments and analyses to prepare for such tests has been underway.

Analysis of several features in the preirradiated fuel tests was completed. First, an improved description of energy deposition for oxide samples in SPR was carried out by using both transport and Monte Carlo calculations with TWOTRAN and MORSE. Fission density profiles for both poly moderator and Cd-filtered moderator configurations were established. Initial calculations show considerable surface heating even in this thin (0.35 g) segment of fuel indicating peak-to-minimum energy deposition ratios of 1.6:1. Neutron filtering was examined which can reduce this ratio to 1.1:1, but with an associated decrease in energy deposition.

In addition to the energy deposition analysis, calculations of heat and oxygen diffusion within the irradiated fuel vessels are being considered. The liner of these vessels is a graphite layer which protects the diaphragm of the pressure transducer used for the vapor pressure measurements. The graphite establishes the possibility that CO gas may be formed by interaction between the atomic oxygen in the vapor and the graphite. Initial estimates of oxygen diffusion in the SPR capsules indicate that the binary diffusion process in the vapor presents a suitable rate-limiting step for this process so that the partial pressure of CO remains well below 1 atm for times of interest in these transient tests.

A sequence of experiments was completed in SPR during the past quarter to determine the energy deposition levels available for preirradiated fuels work and to evaluate the energy deposition diagnostics. The energy deposition levels are based upon posttest fission product analysis (FPA) of the samples. Initial tests in SPR have shown energy deposition levels ranging up to 700 cal/g by this method. Cross comparison of FPA work by using different detectors and counting geometries is underway to determine the experimental uncertainty which may exist in the energy measurements.

In the same series of tests, vapor pressure measurements over fresh fuel samples were made. An example of a pressure record from an eddy current-type gage (Kaman Type 1913) is shown in Figure 1.2-1. The initial negative pulse corresponds to the signal induced in the gage by the neutron pulse. Following this is a positive signal of about 0.12 V which corresponds to a pressure of 85 atm. The decay in this pressure signal over a period of about 10 ms is evident.

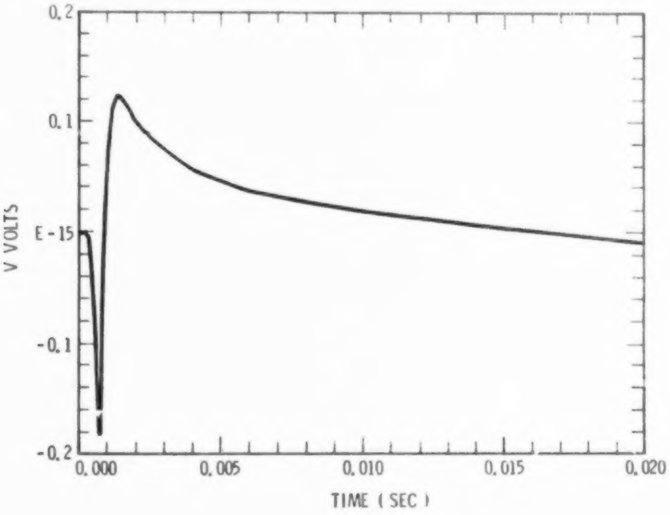

Figure 1.2-1. Pressure Transducer Signal of a Vapor Pressure Transient in the SPR-III Reactor. (The negative signal at the beginning of the pulse induced by the neutron pulse while the positive excursion describes the pressurization over a 0.35-g oxide sample. The pressure calibration for this transducer is 690 atm/v.)

Similar experiments incorporating a movable piston in the pressure vessel have uncovered a significant unexpected problem with the Kaman gages. The gages presently being used exhibit a sensitive microphonic behavior. It has been found that stray signals much larger than the pressure-induced signals are generated by the noise from the piston motion. In the case of the preirradiated fuels tests, this noise problem will be eliminated by removing the piston gage from the pressure vessel. Other problems may remain in the use of these types of pressure transducers. One of these problems is due to possible errors induced in the pressure measurements by nonuniform loading of the transducer face. A vapor pressure experiment preferentially loads the center region of the diaphragm. This is in contrast to the total fluid immersion loading commonly used to calibrate the transducers. Appropriate pressure testing fixtures to evaluate this behavior in the transducers have been built to permit eliminating loading-induced errors as a source of error in the irradiated sample tests.

In preparation for the preirradiated-sample tests, the design of suitable hot cell fixtures has been completed. Prototypes of these fixtures and the pressure vessel for the tests were fabricated and are being evaluated at LASL where the sample loading process will be carried out in the CMB-14 hot cell facilities.

The design of the pressure vessel, as well as the double containment for the mixed oxide samples were completed. Parts for the initial series of experiments are now being fabricated. The safety analysis for an experiment plan based on this design is now being prepared for these SPR experiments. The test will be carried out upon approval by the Sandia SPR and Nuclear Safeguards Committees.

1.2.3 Neutronic Considerations

Calculations were performed to determine the energy deposition profiles in the SPR-III irradiated fuel EOS experiments. Small samples of powdered UO_2 are placed in the SPR-III glory hole with a polyethylene moderator to increase the energy deposition by softening the cavity spectrum. The softened spectrum will also skew the sample fission density toward the surface. This skewing is undesirable from an experiment-analysis viewpoint. A thermal neutron filter can be placed inside the poly moderator to absorb some of the very thermal neutrons without filtering the epithermal contribution to the energy deposition. In this way, the energy deposition can be maintained, to a degree, while flattening the fission density profile.

Calculations were performed with transport and Monte Carlo computer codes TWOTRAN II and MORSE to evaluate the fission density profile in the UO_2 sample in Figure 1.2-2. The figure illustrates the convergence of the fission density profile with respect to angular quadrature used in the TWOTRAN II calculations. As a confirmatory calculation, the fission density was calculated by MORSE modeling of the test with a uniform isotropic surface source which is in good agreement with the transport calculation results.

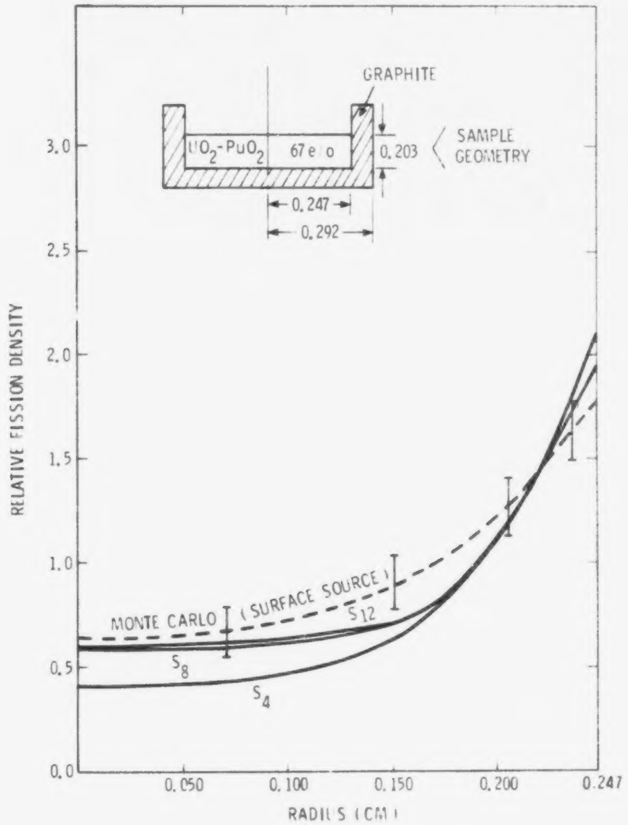

Figure 1.2-2. Fission Density Profiles in a UO_2 Sample Calculated by Transport Theory and Monte Carlo

Figure 1.2-3 details fission density profiles for a UO_2 sample under examination for another EOS experiment. The results shown are compared to results obtained from diffusion theory, DTF IV, for a spherical sample showing good agreement.

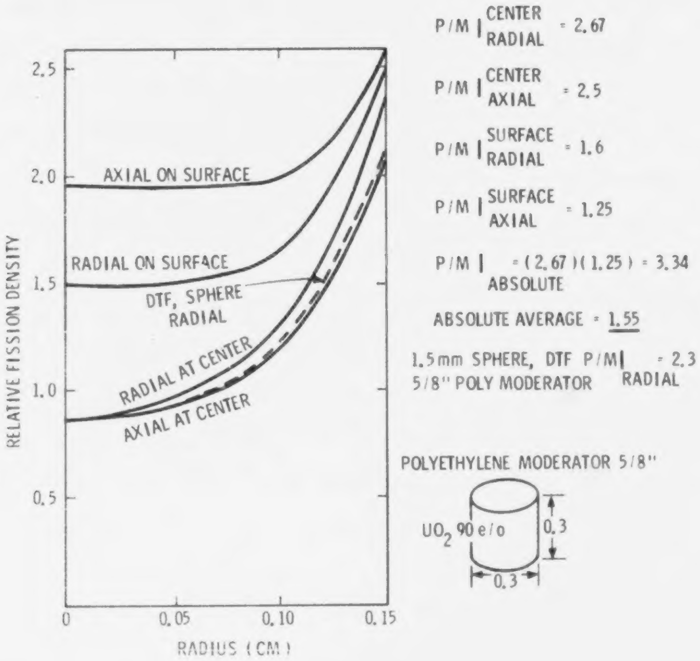

Figure 1.2-3. Fission Density Profiles in a UO_2 Sample Calculated by Transport and Diffusion Theory

Fission density profiles calculated for bare and cadmium filtered cases are shown in Figure 1.2-4. The dramatic fission density profile flattening with the cadmium filter is evident with a penalty in average energy deposition of a factor of 11.5.

The cadmium filter decreases the energy deposition unacceptably but does indicate the saturation cadmium filter design. A thinner filter will diminish the decrease in both the energy profile and deposition. Further analysis will be performed to calculate the filter design that will provide an acceptable energy deposition and fission profile.

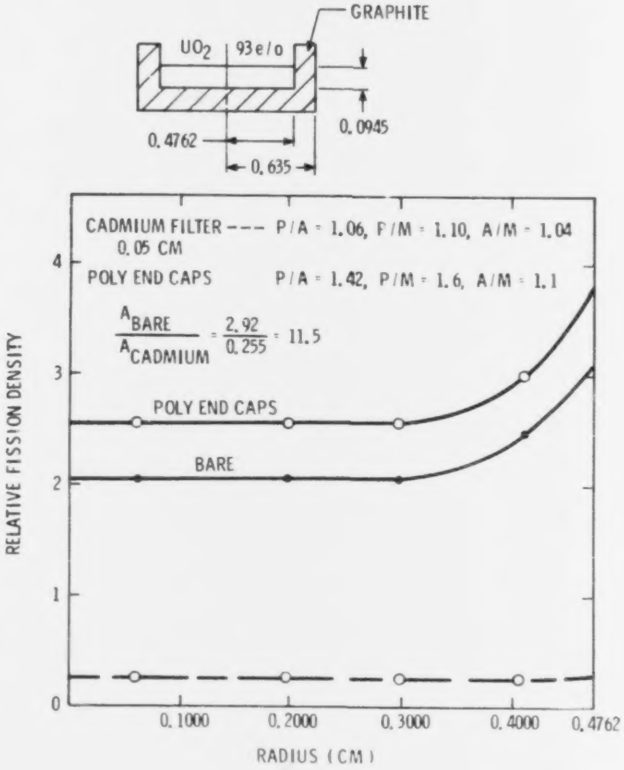

Figure 1.2-4. Comparison of Filtered and Bare Energy Deposition Profiles for a UO_2 Sample

1.2.4 Analysis of Possible Rate Effects in Aerosol Source Experiments

1.2.4.1 Introduction -- A principal effort this quarter consisted of using results from the ACPR aerosol experiments [1-11] to obtain indications of the size and importance of the dynamic heat capacity of UO_2.[1-12] The resulting calculations reported below show that the equilibrium EOS suffices for those experiments; that is, no evidence for rate effects was seen although these rate effects cannot be completely eliminated due to rather large temperature uncertainties in the experiments.

1.2.4.2 Experiments -- The experiments involve a 2.5-in.-long segment of a fresh UO_2 fuel pin pulse heated in the ACPR. The total energy deposition was 570 cal/g (determined from a fission product inventory), enough energy to eventually melt and vaporize the fuel. This energy deposition occurred in approximately 10 ms.

A series of films was taken of the pin during the reactor pulse. The early frames of these films were used to optically determine the temperature of the surface of the solid fuel. Additionally, both side views and end views were obtained. For the side views, the time of the first frame is not correlated with the reactor pulse; however, for the end views, the film sequence and the reactor pulse were correlated. A 1.1-in.-deep hole was drilled in the end of the pin segment so that end temperature readings included a center hole reading and an outside reading. The information made available by these temperature readings was a series of surface temperature vs time readings (an entire spatial profile of the side surface temperature was available for the fourth frame, $T \simeq 2800$ K) with the zero of time uncorrelated to the time of the reactor pulse. The shape of the reactor pulse as well as the total energy deposition was known. In addition, there is a sequence of two end temperature readings (center hole and outside) which has a zero of time correlated to the reactor pulse.

The optical pyrometry measurements are reliable to within an accuracy of ±75 K. The fission product inventory has an error of about 5%.

1.2.4.3 Calculations -- Attempts to analytically produce surface temperature vs time predictions for this experiment using both an equilibrium heat capacity model and a nonequilibrium model proceeded in the following manner. The temporal and spatial dependence of the energy deposition were assumed to be separable. Further, it was assumed that the temporal dependence was the same as that of the ACPR neutron pulse. This pulse is well described by the normalized function

$$G(t) = \frac{\dfrac{0.704\text{x}10^{3}}{\text{sec}}\; e^{-0.704\text{x}10^{3}(t-\tau)/\text{sec}}}{\left(1 + e^{-0.704\text{x}10^{3}(t-\tau)/\text{sec}}\right)^{2}} \qquad (1.1$$

where t is time measured from some arbitrary zero and τ is the center of the neutron pulse.

The relative spatial energy deposition was determined with the use of the neutronics code TWOTRAN. This is a two-dimensional code, a source of some error because the neutron source was not radially symmetric with respect to the fuel pin. However, Sandia modeled it as if it were radially symmetric and obtained a numerical energy profile which is well represented by the formula

$$E \propto \left\{ 1 + 0.462 \left(\frac{R}{R_0}\right)^2 + 0.09 \left(\frac{Z}{Z_0}\right)^2 \left(\frac{R - R_0}{R_0}\right)^2 + 0.00731 \left(\frac{R}{R_0}\right)^2 \left(\frac{Z}{Z_0}\right)^2 \right\} ; \tag{1.2}$$

where Z_0 is half the length of the fuel segment minus the radiation depth ($Z_0 = 3.155$ cm); Z is the axial distance measured from the center of the fuel segment; R_0 is the radius of the fuel segment minus the radiation depth ($R_0 = 0.226$ cm) and R is the radial distance from the center of the pin segment. Normalized over the entire volume of the fuel pin

$$E(R, Z, t) = \frac{E_{TOT} G(t)}{1.262} \times \left(1 + 0.462 \left(\frac{R}{R_0}\right)^2 + 0.09 \left(\frac{Z}{Z_0}\right)^2 \left(\frac{R - R_0}{R_0}\right)^2 + 0.00731 \left(\frac{R}{R_0}\right)^2 \left(\frac{Z}{Z_0}\right)^2 \right) , \tag{1.3}$$

where E_{TOT} is the total energy per unit volume deposited in the fuel pin, determined experimentally from the fission product inventory.

To apply the one-dimensional dynamic heat capacity code described in the previous quarterly[1-12] to the two-dimensional problem, Sandia staff personnel have superposed the two one-dimensional temperature profiles resulting from the energy depositions

$$E_R(R, t) = \frac{1}{1.262} \left(1 + 0.462 \left(\frac{R}{R_0}\right)^2 \right) \tag{1.4}$$

and

$$E_Z(Z,t) = \frac{1}{2.262}\left(1 + 0.09\left(\frac{Z}{Z_0}\right)^2\right) . \qquad (1.5)$$

The resulting one-dimensional temperature profiles, $T_R(R,t)$ and $T_Z(Z,t)$, were combined to produce the following two-dimensional temperature profile:

$$T(R,Z,t) = T_R(0,t) + \left[T_R(R_0,t) - T_Z(0,t)\right]\left(\frac{R}{R_0}\right)^2$$

$$+ \left(\frac{Z}{Z_0}\right)^2\left[0.081222\left(\frac{R}{R_0}\right)^2 + \left(\frac{R - R_0}{R}\right)\right]\left[T_Z(Z_0,t) - T_Z(0,t)\right]. \qquad (1.6)$$

That is, the superposed temperature profiles T_R and T_Z, which represent a rectangular geometry are transformed to cylindrically symmetric three-dimensional geometry by (1) assuming that the center temperature, $T(0,0,t)$ is given most accurately by $T_R(0,t)$ because most conduction heat loss will be in the axial direction, (2) assuming that the radial (axial) temperature profile is parabolic (reflecting the energy deposition) with the curvature determined by the calculated $T_R(R,t)$ $(T_Z(x,t))$, and (3) assuming that the "cross" term proportional to R^2Z^2 is in the same proportion to the $(R - R_0)^2Z^2$ term as the energy deposition.

Given the one-dimensional time-dependent energy depositions $E_R(R,t)$ and $E_Z(Z,t)$, the dynamic heat capacity code calculates the temperatures in a sample of UO_2 which has surface radiation and heat conduction. This calculation uses a dynamic heat capacity model whose relaxation time is a parameter of the code. Sandia has used temperature dependent values for the heat conduction[1-13] and surface radiation parameters.[1-14] For the thermal conductivity

$$H = \left[4 + 2.57 \times 10^{-2}T\right]^{-1} \times 10^7 + 0.73 \times 10^{-5}\, T^3 \text{ erg/sec/cm K} .$$

For the emissivity

$$\epsilon = 0.9 \quad (T < 1645\ K)$$

$$= 1.545 - 3.9215 \times 10^{-4}\ T\ (T > 1645\ K)\ .$$

Two extreme values of the material relaxation parameter were used to depict the system as being either in complete equilibrium or in complete nonequilibrium throughout the experiment. Use of the one-dimensional temperature profiles generated by the code and Eq (1.6) to predict surface and end temperatures of the fuel pin yields the temperature profiles in Figures 1.2-5 and 1.2-6 for the relaxed and unrelaxed systems. These profiles are to be compared to the temperatures measured by the experiment, represented in Figures 1.2-6 and 1.2-7. The zero times of theory and experiment in Figure 1.2-7 are correlated through the energy deposition profile but the time zeroes of Figures 1.2-5 and 1.2-7 have no such correspondence.

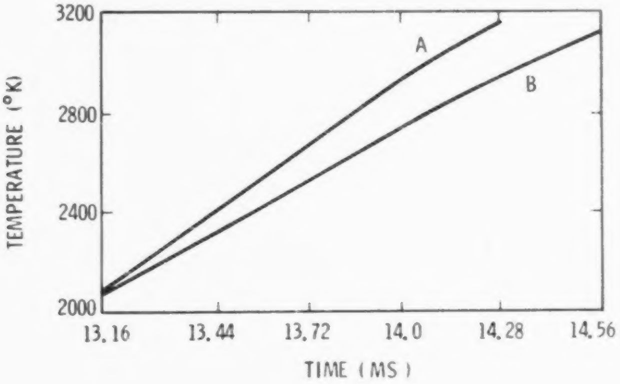

Figure 1.2-5. Calculated Temperature vs Time for Nonequilibrium Model (A) and the Equilibrium Model (B) of the Heat Capacity

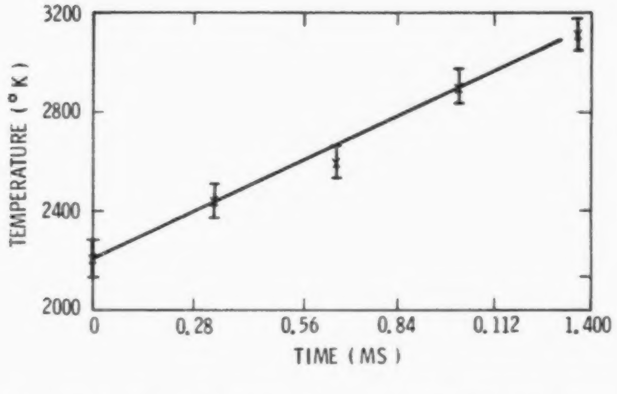

Figure 1.2-6. Measured Temperature vs Time for Frames 1 Through 5

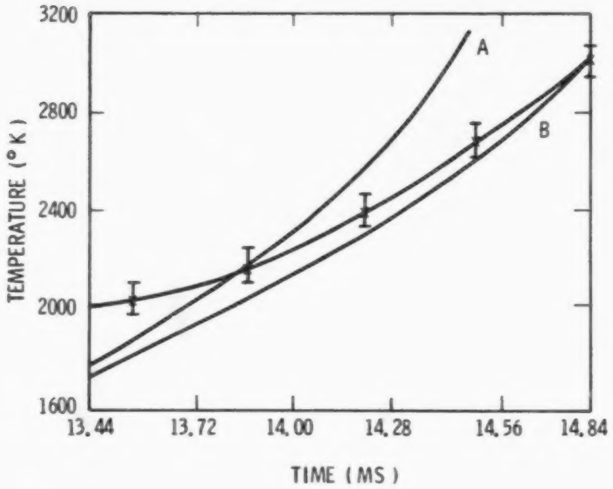

Figure 1.2-7. Theoretical Predictions of Center Hole Temperature on End of Fuel Segment for Nonequilibrium Model (A) and the Equilibrium Model (B) of the Heat Capacity, and Measured Values, Given by Xs for Odd Frames 1 Through 9

1.2.5 Conclusions

The conclusions that may be drawn from this analysis are that the equilibrium heat capacity of UO_2 seems to adequately reproduce the experimental results, although the large uncertainties in the experimental temperature measurements do not allow exclusion of the possibility of some dynamic effects in the heat capacity. Temperature spatial profiles predicted by the analysis seem to agree to within experimental error with those observed in the experiment. Thus within the level of accuracy of the experiment, all phenomena seem to be adequately well predicted by an equilibrium heat capacity model for UO_2. However, these results do not totally exclude the possibility of the existence of a dynamic heat capacity for UO_2, especially on time scales less than those of the experiment, a few milliseconds.

BLANK PAGE

References for Section 1

1-1. S. W. Key, Z. E. Beisinger, *HONDO-II - A Finite Element Computer Program for the Large Deformation Dynamic Response of Axisymmetric Solids*, SAND78-0422, Sandia Laboratories, Albuquerque, NM, 1978.

1-2. P. D. Patel, and T. G. Theofanus, "Fragmentation Requirements for Detonating Vapor Explosions," *Transactions of the American Nuclear Society* *28*, 451 (1978).

1-3. M. F. Young, "Fuel Pin Modeling for the Prompt Burst Excursion (PBE) Experiments," *Transactions of the American Nuclear Society* *28* (1978).

1-4. L. L. Smith et al, *SIMMER II Manual* to be published.

1-5. M. F. Young, "Hydrodynamic Analysis of the LMFBR Prompt Burst Excursion (PBE) Experiment," *Transactions of the American Nuclear Society* *27*, 508 (1977).

1-6. *Advanced Reactor Safety Research Program Quarterly Report*, April-June 1978, Advanced Reactor Research Department, SAND78-2001, Sandia Laboratories, Albuquerque, NM, to be published.

1-7. *Advanced Reactor Safety Research Program Quarterly Report*, July-September 1977, Advanced Reactor Research Department, SAND77-1975, Sandia Laboratories, Albuquerque, NM, May 1978.

1-8. *Advanced Reactor Safety Research Program Quarterly Report*, October-December 1977, Advanced Reactor Research Department, SAND78-0611, Sandia Laboratories, Albuquerque, NM, October 1978.

1-9. *Advanced Reactor Safety Research Program Quarterly Report*, January-March 1978, Advanced Reactor Research Department, SAND78-1421, Sandia Laboratories, Albuquerque, NM, February 1979.

1-10. P. A. Pizzica, P. B. Abramson, "EPIC-FCI A Numerical Model of Fuel and Coolant Motions Following Pin Failure," *NSE* *64*, 465 (1977).

1-11. *Advanced Reactor Safety Research Program Quarterly Report*, July-September 1977, Advanced Reactor Research Department, SAND77-1975, Sandia Laboratories, Albuquerque, NM, August 1978, p. 67.

1-12. *Advanced Reactor Safety Research Program Quarterly Report*, April-June 1978, Advanced Reactor Research Department, SAND78-2001, Sandia Laboratories, Albuquerque, NM, to be published, Section 1.2.

1-13. A.B.G. Washington, UKAEA Reactor Group, Risley, TRG-Report-2236, September 1973.

1-14. A. Alexis and W. Linder, J. Nuclear Mat. *64*, 220, 1977.

BLANK PAGE

2. FUEL DYNAMICS

2.1 Fuel Disruption (G. L. Cano, 4423; W. J. Camp, 4425; N. K. Hayden, 4425; R. W. Ostensen, 4425)

2.1.1 Introduction

The Fuel Disruption experiments, aimed at determining the response of irradiated fuel under LOF conditions, have entered a second stage with the successful completion of the first (FD-1) series of experiments. Except for limited posttest examination of the disrupted fuel, experiment data analysis is complete. Detailed neutronic and thermal analyses have been performed and predicted fuel and clad temperatures are in excellent agreement with experimental data. Experiment modeling has involved the development of a new fuel swelling code, FISGAS, and comparison of its predictions to experiment, as well as FRAS-2-type models. The first stage of FISGAS development is now complete as are detailed swelling predictions. Modeling of those experiments which led to strong fuel disruption has commenced and will continue.

The second series (FD-2) of experiments has gone through preliminary design stage. These experiments, which are to be carried out in the ACRR, will lead to substantial improvements in prototypicality (with respect to LOF phenomenology), and should allow Sandia to follow fuel disruption through clad melt, fuel swelling, and final fuel disruption. As part of the second stage of its development, FISGAS will be employed to predict the swelling portion of fuel disruption in these experiments.

2.1.2 Experiment

Planning and preliminary design of the forthcoming fuel disruption experiment series, FD-2, has continued.

TWOTRAN neutronic and TAC2D heat transfer calculations helped to define the experiment geometry. This geometry, coupled with the ACRR neutron fluence and spectra, produces essentially flat (within 15%) axial and radial energy generation profiles in the fuel and temperature profiles which are approximately prototypic of an LOF as defined by SAS calculations. Thermal neutron filtering is necessary to produce appropriate energy generation factors; cadmium lowers the energy-flux peak-to-average ratio to 1.15:1 (in FD-1, this ratio was as large as 2:1), and the peak-to-minimum ratio to 1.35:1 (in FD-1, this ratio was as large as 4.2:1). Exact filter type and features remain to be defined. The parameter of greatest uncertainty continues to be the heat transfer coefficient of the gap between the fuel and the stainless steel clad. Values which differ by as much as 100 are being used in the calculations. These selected values are used because specifics relating to gas type and amount are unknown as are such gap characteristics as width and fuel surface condition. In any case, the clad melts off about 1 to 3 seconds before the fuel disrupts, depending on gap conductivity and amount of neutron filtering for a given ACRR energy output. Work is continuing in this area.

A preliminary FD-2 test matrix which accounts for the fuel and ACRR parameters of interest has been formulated. Approximately 14 experiments will be conducted. The fuel amount, mounting, and lighting have been worked out; the fission-gas sampling still is under development. A laboratory mockup of fuel mounting, lighting, photography, and some diagnostics geometry has aided greatly in further improvement and development.

The light optical microscopy (LOM) and the scanning electron microscopy (SEM) performed on the fresh fuel used in experiment FD-1.9 were completed. The photographs show that the pellet interiors were melted in the heating phase. Upon solidification, the radial thermal gradient produced cracking, a central void, and three structural regions. The thermal history and profile allowed for typical grain growth and sintering to occur out to the specimen edge. The posttest analysis on the mixed oxide fuel used in experiments FD-1.4, -1.7, and -1.8 is in progress at LASL under Sandia direction. The respective pellets were extracted from their experiment canisters, photographed, potted, and sectioned. Final grinding and polishing are to be done upon LASL's receipt of magnifying stereo-optical equipment needed for remote viewing of the procedure and guidance. This work, to be completed within the next 3 to 4 months should yield information on melt fronts, voids and crack generation, and perhaps some limited fission gas bubble morphology.

A paper on the FD-1 experiment, results, and analysis was written and submitted to the Brussels (Belgium) conference on advanced reactor safety for publication in the proceedings. A joint LASL-Sandia paper on the hot cell remote handling of the FD-1 fuel has been accepted for presentation at the upcoming ANS winter meeting. Finally a topical report on the FD-1 series is being written.

2.1.3 Thermal Design Analysis of FD-2 Experiments

Based upon preliminary analysis, Sandia has chosen the geometry for the experiment to yield flat axial and radial profiles. After selection of the geometry, the next consideration is adjustment of the power factor by the use of filtering. In these calculations, the peak reactor power is assumed to be 200 MW. The power factor (PF) is in units of W/cm^3 deposited in a fuel pellet per MW of reactor power.

Correction of the power profile used in the first series of analyses for PFs ranging from 75 to 200 yielded center temperatures and surface temperatures which were, respectively, 33 and 20% higher than previously calculated at 5 s. Thus the decision was made to study cases involving PFs of 100 and 80.

The filtering required to obtain these PFs causes little change on the temperatures, time of clad melt, and fuel melting. The greatest difference between calculations made with a radial profile which accounts for the filter and those made with unfiltered radial profile is approximately 2%.

To obtain a PF of 100, a cadmium filter 0.0012 cm thick is needed, yielding a neutron flux with a radial peak-to-average ratio of 1.2. The thickness required for a a PF of 80 is 0.00267 cm, giving a peak-to-average ratio of 1.148. If cadmium is used as the filter, a PF of much less than 80 is not possible; an increase in cadmium thickness to as much as 0.005 cm will only reduce the PF to 78 or 79. It will not go below this.

The pulse used for the calculations has a peak power of 200 MW which occurs in a narrow pulse at 0.65 s. The average power from 0.8 to 3.0 s is 55 MW. From 3.0 to 5.0 s, the power falls off linearly from 50 to 28 MW, and falls from 28 at 5 s to 3 MW at 6.4 s. The integrated energy in this pulse is 265 MJ. The width of the initial peak is about 0.2 s and yields 32 MJ (12% of the total amount).

For each PF there are two parameters which most significantly affect the time of clad melt, temperature of fuel at clad melt, and peak temperatures reached in the fuel. These parameters are the conductivity of the gas (GC) in the gap between the fuel pellet and stainless steel clad, and the axial profile of the neutron flux. The axial profile, however, changes the expected result by 5 to 7%, whereas the difference in results for GC of 0.0001 and GC of 0.01 is as much as 47% in some cases.

Three axial profiles (AP) were considered. One was assumed to be perfectly flat. The other two arise because neutronic calculations give data points that can be interpreted as two different shapes. One is a smooth parabola (AP1). The other interpretation peaks at the ends, falls to minima near the endcaps, and rises in the center of the fuel (AP2). There seems to be no experimental evidence to suggest which interpretation is more accurate. In any event, the difference in calculations for the three different cases appears to be no more than 5 to 6%. In no case does it appear that the fuel will melt at the ends before the clad peels off and the center of the fuel also melts. (However, for the case in which the gap conductance is given by GC = 0.0001, the fuel is at melt temperature at the time of clad melt.)

The melt temperature for stainless steel used in these calculations is 1700 K, and for UO_2 it is 3020 K. The greatest effect of changing the GC is seen in the time at which the clad reaches 1700 K and in the surface temperature of the fuel at this time. Averaging the results from the runs performed with a PF of 80 and a PF of 100, as well as different axial profiles, the following comparisons can be made:

1. For a GC of 0.0001, the time of clad melt is 0.6 s later than for a GC of 0.001. For a GC of 0.001, the time of clad melt is 0.13 s later than for a GC of 0.01.
2. For a GC of 0.0001, the center temperature at clad melt is 11% higher than for a GC of 0.001. For a GC of 0.001, the center temperature at clad melt is 5.5% higher than for a GC of 0.01.
3. For a GC of 0.0001, the surface temperature at clad melt is 32% higher than for a GC of 0.001. For a GC of 0.001, the surface temperature at clad melt is 10.3% higher than for a GC of 0.01.

The gas conductivity does not have as large an effect on the fraction of fuel melted by 6.5 s. This seems to depend mostly on the PF. The time to center fuel melting and surface temperatures at that time are more erratic. As expected, the sensitivity to GC dies down at later times; temperature differences for different GCs vary at most by 1% at 6.5 s.

Calculations indicate that 75 to 80% of the fuel should melt when using a PF of 80. A PF of 100 increases this fraction, yielding a prediction that 90 to 93% of the fuel will be melted at 6.5 s. However, in one such case (PF = 100, GC = 0.001, AP1), the center temperatures at 6.5 s are slightly greater than 4000 K. Note also that in all cases the temperature of the fuel starts to fall after 6 s. Thus, with this power profile, the temperatures and fuel melt fraction would not increase if the calculations were extended to cover a longer period of time.

One final observation is that the ratio of temperatures at the axial ends of the fuel pellet to the temperature at the center depends on radial location. The ends are colder than the center throughout the time leading to fuel melt. Within a relatively short time period which includes the time at which the fuel melts, the annular region near the outer edge of the pellet around the axial ends begins to heat at an accelerated rate, becoming hotter than the corresponding region at the axial center. In the region surrounding the radial center of the pin, however, the axial ends always remain cooler than the axial center. For a PF of 80, the rate of temperature rise after 3.5 s is only 3.5% within a cylindrical region from a radius of 0.188 cm to the outer edge at a radius of 0.254 cm. For a PF of 100, this leveling off does not occur until 4.5 s. As noted earlier, after 6 s the temperatures will actually begin to drop.

In summary, the axial profile does not significantly affect the behavior of the experiment because it is sufficiently flat, even in the worst case, to preclude the fuel's melting out of the axial ends prior to clad melting. The uncertainties about the GC, however, seem to play an important role, especially in fuel behavior just before and during clad melting. A maximum of 94% of the fuel is predicted to reach melt temperature. By February 1979, the ACRR should have the capability to produce a 300- to 350-MJ energy pulse, 13 to 32% more energy than was used in the calculations just discussed. Further, these calculational runs indicate that the energy loss in the fuel will begin to exceed the energy deposited at approximately 5.9 s. This analysis shows that the present experiment design is adequate to duplicate LOF thermal conditions.

2.1.4 Analysis

Initial development of the FISGAS code was completed. Work during the last quarter involved the inclusion of a more sophisticated model of grain-boundary gas behavior. Gas on the grain boundary is now divided into two classes, grain-face gas and grain-edge gas.

Intragranular bubbles reaching the grain boundary are trapped on the grain face and are forced to migrate along the plane of the grain face. As previous quarterly reports describe, the migration and coalescence of bubbles on the grain face are calculated with the asymptotic model, independent of the calculation of intragranular gas behavior. Those gas bubbles which have migrated far enough to reach a grain edge (intersection of two grain faces) leave the grain face and are trapped on the grain edge. One additional mechanism is provided for transfer of gas from the grain face to the grain edge. When more than 50% of the area of the grain face is covered by gas bubbles, that excess gas is immediately transferred to the grain edge. This calculation is based on percolation theory which indicates that at about 50% areal coverage the bubble porosity should begin to link up into a network of connected porosity and vent to the grain edge. Such networks have been observed in posttest examination of transient tested fuel. With the FISGAS modeling, most of the gas transfer to the grain edge occurs by percolation rather than by gas bubble migration.

Gas which reaches the grain edge is assumed to be trapped there. Grain-edge bubble coalescense is based on the behavior of grain-face gas. That is, there is no independent calculation of migration and coalescence of grain-edge gas. Because of the rapid saturation of the grain faces with gas bubbles and percolation to the grain edge, most of the grain-boundary gas is on the grain edge. Thus, most of the fuel swelling is due to grain-edge gas.

Gas release from the fuel to ambient conditions is now modeled as percolation from the interconnected porosity on the grain edges. Grain-face gas does not directly participate in the final gas release from the fuel thus effectively slowing the release of gas and leading to greater values of predicted swelling.

Figures 2.1-1, 2.1-2, and 2.1-3 are comparisons of the experimental data for Tests FD-1.4, -1.7, and -1.8 to predictions by FISGAS and FRAS 2-type modeling. As noted in the previous quarterly report, FISGAS tends to overpredict the early swelling prior to the third pulse. This may be due to an error in the value of the bubble diffusion coefficient at low temperatures. FISGAS predicts an even faster swelling rate after the third pulse than that observed in the experiments. This is in sharp contrast to the FRAS 2-type results shown in the figures. FRAS 2 modeling predicts hardly any additional swelling after the third pulse. This shortcoming demonstrates the inadequacy, for fuel swelling calculations, of models which neglect grain-boundary gas. The overprediction of early swelling is duplicated by FRAS 2-type models. This indicates that excessive intragranular swelling is a primary cause of the overprediction of early swelling by FISGAS.

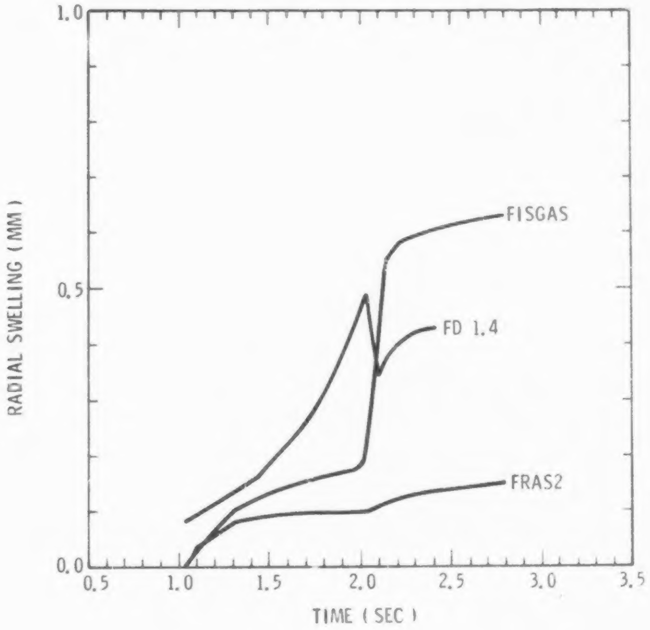

Figure 2.1-1. Predicted and Calculated Fuel Swelling - Test FD 1.4

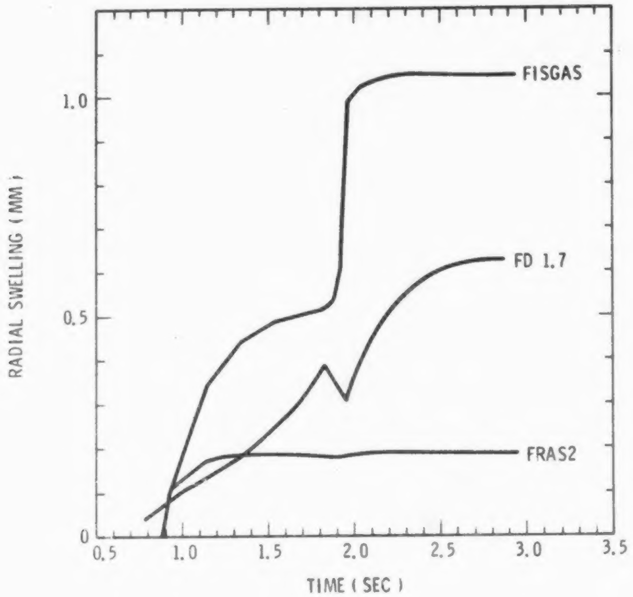

Figure 2.1-2. Predicted and Calculated Fuel Swelling - Test FD 1.7

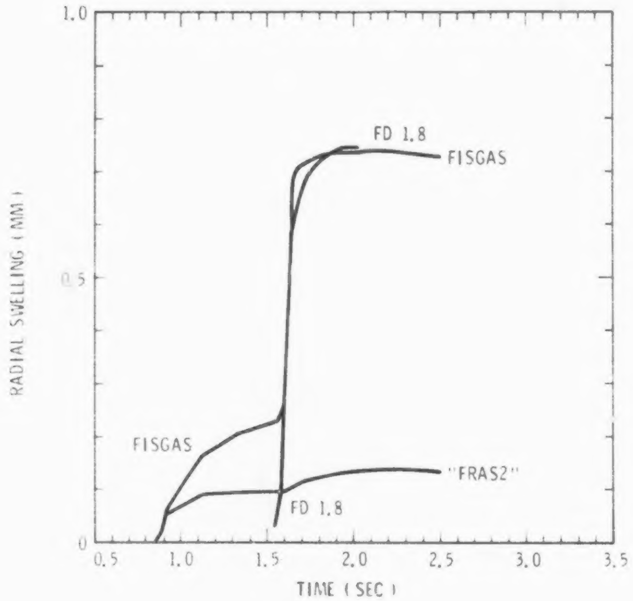

Figure 2.1-3. Predicted and Calculated Fuel Swelling - Test FD 1.8

To summarize, the comparison of FISGAS and FRAS 2-type predictions with the FD-1 test data demonstrates that the modeling of grain-boundary gas is necessary for the accurate prediction of fuel swelling in a LOF accident. In addition, the code calculations showing extremely rapid swelling are in substantial agreement with the rapid swelling observed in the tests. Thus, although prior to the FD-1 series, such rapid swelling was not anticipated, the speed of the swelling is seen, a posteriori, to be fully consistent with reasonable gas behavior models combined with high temperature UO_2 creep.

2.2 Transition Phase (S. W. Eisenhawer, 4422; R. J. Lipinski, 4425; R. W. Ostensen, 4425; D. O. Lee, 5511)

2.2.1 Introduction

Following the loss of initial geometry in a core disruptive accident and assuming that neither early shutdown nor rapid hydrodynamic disassembly takes place, the accident enters the transition phase. At this point, one or a number of subassemblies have melted down and radial propagation takes place as subassembly hexcans are melted through. The progression of the transition phase may strongly influence the severity of the accident, and it is therefore important to understand in detail the phenomena associated with this accident stage. In particular, several key questions need to be answered. First, in the early stages of the accident is the fuel dispersive, that is, how far can the molten fuel and fission gas mixture move axially before it freezes? Secondly, if blockages form and the core is bottled up, what is its configuration - does it remain boiled up, or does the pool collapse and a recriticality occur? Answers to these questions depend upon resolving the uncertainties in transition phase phenomenology. Work at Sandia is directed toward the mechanics of fuel blockage formation and boiling pool behavior. Both analytic and experimental studies are included in this effort. Activities this quarter were concentrated in three areas: application of the transpiration heat transfer model to the fuel streaming problem, initial experiments with the liquid-liquid ablation test rig, and a study of the behavior of a boiling pool having a partially stable fuel crust.

2.2.2 Liquid-Liquid Ablation Modeling Efforts

The formation of fuel blockages by freezing is an important aspect of the transition phase. Heat transfer between flowing molten fuel and ablating steel walls is affected by transpiration as molten steel moves away from the solid wall and is ablated into the bulk flow. This effect was examined in greater detail this quarter.

As discussed in a previous quarterly report,[2-1] the effect of transpiration on the heat transfer rate, q_w, on a melting wall in turbulent flow can be correlated by the expression

$$\frac{q_w}{q} = \frac{2}{(1 + \sqrt{1 + \frac{4}{k}}} , \qquad (2.1)$$

where q is the heat transfer rate without transpiration, and K (the Kutateladze melting number) is given by

$$K = \frac{L + C_s(T_m - T_0)}{C_l(T - T_m)} . \qquad (2.2)$$

In this equation, L is the heat of fusion, C_S and C_l are the heat capacities of the wall material in solid and liquid form, T_m and T_0 are the melting temperatures and initial temperatures of the wall, and T is the bulk stream temperature. This equation was based on experiments with gases.

An alternative expression for the effect of transpiration may be derived very easily if the transpiration flow, directed away from the wall, is assumed to be laminar instead of turbulent. This yields

$$\frac{q_w}{q} = K \ln (1 + \frac{1}{K}) . \qquad (2.3)$$

Equation (2.3) has been used, for example, in the USEFUL code for turbulent flow conditions. The use of Eq (2.3) in turbulent flow has been justified on the basis of agreement with experimental melting rates of icebergs in salt water.

Predictions of Eqs (2.1) and (2.3) are compared in Table 2-I. The Kutateladze number for a melting iceberg in cold seawater is in the range of 10 to 20. Note, from Table 2-I, that the effect of transpiration for such a system is almost negligible, so the previous justification given for using Eq (2.3) under turbulent conditions is spurious. However, over the range of relevant Kutateladze numbers (0.1 to 10 in simulant experiments and about 0.5 for the fuel blockage problem), the difference between a turbulent and a laminar calculation is not significant. This insignificance provides some confidence in extrapolating these equations to the more complex fuel-steel ablation problem. For the fuel blockage problem, transpiration would reduce the heat transfer rate to the wall by a factor of 2, according to Table 2-I. An integrated approach is now being followed which examines the combined effect of eddy diffusivity and transpiration on both sides of a distinct liquid-liquid interface at which entrainment occurs. For experimental purposes, the concept of an entrainment temperature is not necessary. A direct energy balance requires that the total heat drain, $\bar{q}$, is given by

$$\bar{q} = jC_p (T - T_w) + q_w \ , \tag{2.4}$$

where j is the ablation mass flux. This implies that

$$\bar{q}/q_w = 1 + \frac{1}{K} \ . \tag{2.5}$$

Thus the wall heat flux can be calculated from the temperature profile in the bulk stream without measurements of the actual wall ablation rate.

If Eq (2.5) is combined with Eq (2.1),

$$\frac{\bar{q}}{q} = \frac{2\left(1 + \frac{1}{K}\right)}{\left(1 + \sqrt{1 + \frac{4}{K}}\right)} \tag{2.6}$$

is produced. From Table 2-II, it may be seen that for the fuel blockage problem (a fuel-steel system with K about 0.5) the transpiration model predicts an increase in heat transfer rate of only 50% above the nonablation case. For high Kutateladze numbers, the ablation has almost no effect according to this model. Thus there may be some difficulty in reliably extrapolating from simulant experiments at high K to a fuel-steel system at low K.

Table 2-I

Comparison of Laminar and Turbulent Transpiration Effects

Kutateladze Number	$\frac{q^w}{q}$ (turbulent)	$\frac{q^w}{q}$ (turbulent/$\frac{q^w}{q}$ (laminar)
0.1	0.27	1.13
0.3	0.42	0.95
1.0	0.62	0.89
3.0	0.79	0.92
10.0	0.92	0.96
30.0	0.97	0.98

Table 2-II

Comparison of Total Transpiration Heat Transfer Rate
to Nonablation Heat Transfer Rate

Kutateladze Number	$\bar{q}/q$
0.2	2.15
0.5	1.50
1.0	1.24
2.0	1.10
5.0	1.02
10.0	1.01

2.2.3 Liquid-Liquid Ablation Experimental Work

The purpose of the liquid-liquid ablation experiments is to study the mechanics of heat transfer during the melting of a wall by a turbulently flowing liquid. During this quarter, the initial experiments with Refrigerant-11 and ice were performed. In these tests, the Re-11 is the molten UO_2 simulant and ice simulates the stainless steel. Calculations for this system assuming different modes of heat transfer were given in a previous quarterly report.[2-2]

A schematic of the test rig is shown in Figure 2.2-1. The construction details and operating procedures were described in the last quarterly report,[2-3] and only a brief review is given here. Re-11 flows from the supply reservoir through a flowmeter into an ice pipe with an initial internal diameter of 0.5 cm. The combined Re-11/water flow is then collected in catch basins attached to load cells. Pressure transducers are located at the inlet and outlet of the ice pipe; thermocouples are mounted in the ice as well as at both ends of the pipe.

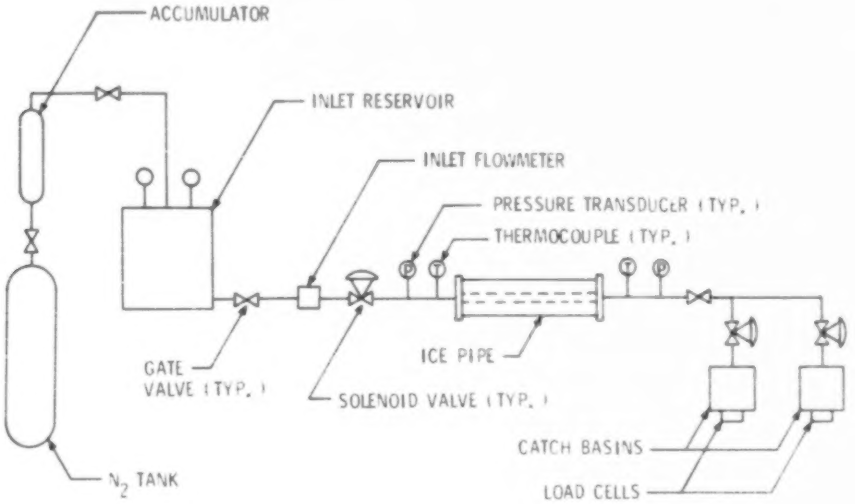
ACCUMULATOR
INLET RESERVOIR
INLET FLOWMETER
PRESSURE TRANSDUCER (TYP.)
THERMOCOUPLE (TYP.)
GATE VALVE (TYP.)
ICE PIPE
SOLENOID VALVE (TYP.)
CATCH BASINS
LOAD CELLS
N_2 TANK

Figure 2.2-1. Schematic of Liquid-Liquid Ablation Experiment Apparatus

Although Figure 2.2-1 shows the ice pipe positioned horizontally, the primary aim of the early experiments has been to determine the effect of gravity on the melting and entrainment processes. To this end, tests were run in all three principal flow orientations: horizontal, vertical upward, and vertical downward flow. During these runs, high speed (200 frames/s) motion pictures were taken. Several types of flow visualization were used. Dye of the same density as water was injected into the Re-11 with a hypodermic needle. However, the needle tends to disturb the flow. A less obtrusive technique was therefore used where low concentration blue dye (approximately 10 w/o) was frozen at selected locations in the ice pipe. The dye melts at the same rate as the surrounding ice and does not disturb the flow.

In addition the RE-11 itself is dyed red to increase the contrast between the channel and the ice. The blue dye in the ice (water) does not mix with the red dye in the Re-11 so the two components can be visually separated.

In the early experiments, the emphasis is on obtaining qualitative information. Later test series, to be reported upon in subsequent quarterlies will concentrate on more quantitative information. This approach has been taken based upon the wide differences in the melting process seen for the three flow orientations. The observations reported below are preliminary and should be viewed as such until additional quantitative results are available.

The tests discussed below were carried out for initial conditions in the following ranges:

Re-11 temperature	18 to 25°C
Reynolds number	40×10^4 to 75×10^4
Ice temperature	0 to -8°C

The initial internal diameter of the pipe in all cases was 0.5 cm (nominal). Each test lasted 90 s.

For all three orientations, two distinct regions can be clearly defined. Near the inlet is a region of strong turbulence characterized by rapid melting and considerable entrainment of the water at the wall. Beyond this is a downstream region where the exact behavior depends upon the flow orientation.

The melting pattern seen in the inlet is shown in Figure 2.2-2. Re-11 flowing into the ice pipe does so through a 0.5 cm brass nipple which extends approximately 1 cm into the ice pipe. The end of this nipple is actually the true beginning of the experimental channel. Clearly, the diameter here cannot change. However, beyond this point the diameter is determined by the melting rate. Hence the inlet acts like a nozzle. As expected, turbulence near the inlet is quite strong. Dye injection shows a clear recirculation region extending 5 to 10 cm downstream. Entrainment of the water film from the wall is pronounced. The combination of strong turbulence and rapid entrainment near the inlet promotes high heat transfer rates and the characteristic bell-mouth pattern observed in every test to date. The change in diameter at the point of maximum melting is in the range, $4 \leq DF/D_o \leq 6$, for the test conditions noted above.

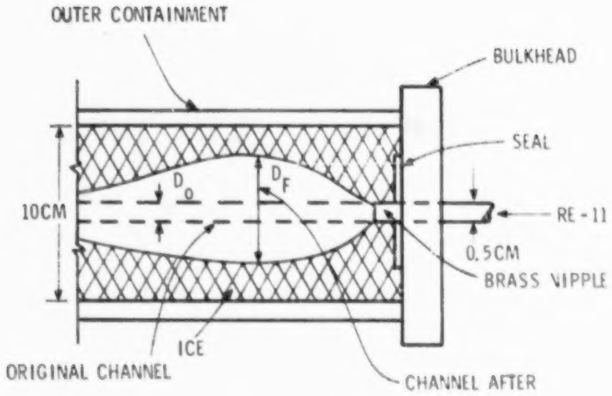

Figure 2.2-2. Observed Melting Pattern During Liquid-Liquid Ablation Experiments

Beyond the inlet section, the three flow orientations exhibit significantly different behavior. In a horizontal system, the difference in density (ρ (Re-11) = 1.59/cm^3) produces stratified flow. Water which is entrained near the inlet is observed to move to the top of the pipe in the downstream section. Of greater interest is the fact that water in the liquid film past the inlet region does not appear to be entrained. Instead a circumferential motion in the film is seen with a net flow of water toward the top of the channel. No entrainment of water from the water ribbon was seen, although interfacial waves are evident. Because of stratification, a circumferential variation in heat transfer to the wall exists. The upper water ribbon acts as an insulator so that the preferential direction of melting is downward.

The situation for vertical flows is somewhat different. The difference in density along with the importance of gravity in the film momentum equation leads to effects similar to those seen in gas-liquid annular flows. However, in the present experiments, the lighter component, water, appears as a film on the melting wall, and the heavier component flows in the core. Such a configuration is not possible (in equilibrium) in a gas-liquid annular flow and leads to an interesting result. The phenomena of flooding and film flow reversal associated with upward gas-liquid flow are of importance here with downward liquid-liquid annular flow when the lighter component is in the film.

Several characteristics of upward gas-liquid annular flow have been observed in downward liquid-liquid flow. Near the beginning of an experiment, interfacial waves of small amplitude and wavelength are observed. All of the experiments are performed with a constant Re-11 mass flow rate. As the ice melts the velocity then decreases as $1/D^2$ and the core Reynold's number as $1/D$. At the same time both the wavelength and amplitude increase. Amplitude on the order of 0.25 D have been observed. The slip ratio between the mean core velocity and the wave velocity appears to be on the order of 10.

Note that the film thickness is a dependent variable controlled by heat transfer to the wall and interaction between the film and the turbulent core. No attempt has been made as yet to measure the mean film thickness, although this clearly affects both the heat transfer and entrainment processes. The film thickness can be estimated by making various assumptions about the velocity profile in the film and the known water flow rate at the exit. These estimates are currently in progress. Near the end of several tests in downward flow, some evidence of entrainment is seen. However, this occurs at sections of the pipe where minor depressions are formed during melting. Water collects in these depressions and hence the film thickness here is large. Whether or not entrainment at such locations can be predicted with standard gas-liquid correlations remains to be seen.

10

Several experiments have also been performed in vertical upward flow. In this geometry, the buoyant force on the film is in the same direction as the flow. That is, if the flow stopped, the water in the film could rise to the top of the test section. Interfacial waves of small magnitude are also seen in this case. No estimate of the film-core slip has as yet been made. Apparently little or no entrainment occurs beyond the inlet region.

2.2.4 Reactor Recriticality With a Partially Stable Fuel Crust

Following a postulated whole-core meltdown, fuel dispersal from the vaporization of stainless steel entrained in the molten fuel is of prime importance in preventing recriticality. Heat losses to the sides of the pool could reduce the amount of vaporization and subsequent fuel dispersal. This radial and downward heat loss is largely controlled by the uncertain existence of a thermally insulating fuel crust overlying the steel containment vessel. At one extreme, with a perfectly stable crust which prevents any molten steel addition to the pool, fuel will easily disperse at less than decay-heat power levels, regardless of assumed flow regime. At the other extreme, with a crust so unstable that convective heat loss directly to the cool steel surface can be assumed, radial heat losses are so large that decay power is not sufficient to prevent recriticality. The present work investigates the middle ground by assuming the crust is stable for a specified growth period and then is removed, only to grow again.

When molten fuel comes into contact with steel above 900 K (627°C), the fuel immediately freezes while the steel simultaneously melts. The thickness of each layer increases with the square root of time (until boundary conditions begin to affect them). If, after a time τ, the fuel crust becomes unstable and is removed, both the crust and the cool underlying steel will enter the bulk liquid fuel and will serve as heat sinks. It is straightforward to determine that the average heat loss from the pool under these conditions is

$$Q_{\ell} = \mathrm{Nu}\,\frac{k}{d}\,(T_p - T_f)\,(\pi dh)$$

$$+ \rho_f \sqrt{\beta_f/\tau}\left(\pi dh + \pi\frac{d^2}{4}\right)\left(L_f + C_f\,(T_p - T_f)\right)$$

$$+ \rho_s \sqrt{\beta_s/\tau}\left(\pi dh + \pi\frac{d^2}{4}\right) C_s(T_p - T_s) \qquad (2.7)$$

where Nu is the pool Nusselt number, k is fuel conductivity, d and h are the pool diameter and height, T is temperature, ρ is density, β is the crust growth constant, τ is the average crust lifetime, L is latent heat, C is specific heat, and the subscripts p, f, and s refer to bulk pool, fuel crust, and steel melt layer respectively.

The minimum amount of vapor generation needed to prevent recriticality is with the bubbly flow regime for which the vapor flow rate is

$$j = \alpha(1 - \alpha)V_{\infty} \qquad (2.8)$$

where α is the void fraction and V_∞ is the terminal rise velocity of a single bubble. Thus, if α_c is the void fraction at which criticality occurs (ignoring shape effects), the heat that must go into steel vaporization to prevent recriticality is

$$Q_v = \alpha_c(1 - \alpha_c)V_\infty \left(\pi\frac{d^2}{4}\right)\rho_{sv} L_{sv} \tag{2.9}$$

where ρ_{sv} is the steel vapor density and L_{sv} is the heat of vaporization of steel.

Therefore, if the heat loss by convection to the crusted wall is ignored, the critical crust lifetime which will prevent recriticality may be determined by equating Q_v with the total heat generation minus the heat loss to the wall, Q_ℓ. This yields:

$$\tau_c = \left[\frac{\rho_f\sqrt{\beta_f}\left(\pi dh + \frac{\pi d^2}{4}\right)\left(L_f + C_f(T_p - T_f)\right) + \rho_s\sqrt{\beta_s}\left(\pi dh + \frac{\pi d^2}{4}\right)C_s(T_p - T_s)}{Sm - \alpha_c(1 - \alpha_c)V_\infty\left(\frac{\pi d^2}{4}\right)\rho_{sv}L_{sv}}\right]^2 \tag{2.10}$$

where S is the mass power density and m is the total mass of fuel.

The following values may be used for a typical 750 MW_{th} reactor at 3% decay power:

$d = 1.3$ m
$h = 0.91$ m
$m = 5000$ kg
$S = 4500$ W/kg
$\rho_f = 9500$ kg/m^3
$\rho_s = 6500$ kg/m^3
$\rho_{sv} = 0.24$ kg/m^3
$C_f = 500$ J/kg · K
$C_s = 787$ J/kg · K

$L_f = 2.76 \times 10^5$ J/kg
$L_{sv} = 7.5 \times 10^6$ J/kg
$T_p = 3070$ K
$T_f = 2385$ K
$T_s = 1700$ K
$\beta_f = 6.7 \times 10^{-7}$ m^2/s
$\beta_s = 7.1 \times 10^{-7}$ m^2/s
$V_\infty = 0.23$ m/s
$\alpha_c = 0.5$

Substituting these values,

$$\tau_c = \left[\frac{2.43 \times 10^7 + 2.98 \times 10^7}{2.25 \times 10^7 - 1.37 \times 10^5}\right]^2 = 5.9 \text{ seconds} \qquad (2.11)$$

Thus, if a fuel crust is stable for less than 6 s on the average, recriticality is possible. The crust thickness and melt layer thickness after 6 s are about 2.1 mm each. The stability of such a crust under the impact of a highly turbulent boiling pool needs investigation. The validity of these conclusions depends strongly on the entrainment of the fractured crust and underlying steel melt into the bulk pool. Whether each entrainment actually occurs will be partially determined by the future liquid-liquid ablation experiments.

2.3 Initial and Extended Fuel Motion (L. M. Choate, 4423; R. S. Howard, 1136; W. H. Sullivan, 4423; J. Odom, 4424; M. F. Young, 4425)

2.3.1 Introduction

Phenomenological investigations are being conducted in transient overpower (TOP), loss of flow (LOF), and LOF-driven TOP advanced reactor accident sequences. To support accident analysis detailed phenomena associated with core disruption must be identified and modeled. These phenomena include fuel motion inside the clad prior to failure, axial fuel failure location, mode of cladding failure, fuel disruption modes (reported in Section 2.1), rate of dispersal, fuel plateout, and extended fuel motion into the blanket (potential for blockage).

Current activities in the program are directed toward planning for up to 19-pin tests in the ACRR and participation in the NRC international exchange program on CABRI through preanalysis of the A-series tests (TOP tests with single-pin geometries). Some tests may be required that involve larger bundle sizes and full length pins. Facilities in which to conduct these tests are being evaluated on a continuous basis. Work on LOF and TOP accidents has been done in the DOE program in TREAT and will continue in the TREAT upgrade. This program will be coordinated with the DOE program in order to take maximum advantage of the available data.

The tests being planned for the ACRR will require a flowing sodium system, high power operating modes in the reactor, preirradiated fuel, hot fuel handling facilities, and a high-resolution fuel motion diagnostics system. The fuel motion system has been constructed and will be installed in early FY79. The capability of the ACRR to operate in high-power modes has been established and will be available in late FY 79. Work on the design of a flowing sodium system has begun and will continue into FY79. The availability of the loop is the item which determines the pace of this work. Some preliminary studies on the potential for using CABRI test pins in the ACRR have been completed.

2.3.2 In-Pile Flowing Sodium System for ACRR

The preliminary conceptual design of the in-pile flowing sodium system continued this quarter. Emphasis thus far has been directed at reviewing the scope of the experimental program with related test requirements as well as assessing various design criteria relating to those requirements. Closely coupled to the sodium loop design is the capability of handling preirradiated fuel during assembly and sodium fill, in the ACRR high-bay area and in the postmortem area. Currently, the capability of handling 19-pin preirradiated bundles in the postmortem area appears to be possible although there is still concern for the ACRR high-bay fuel area handling requirements. Consultations are continuing with ANL concerning loop design and fuel handling requirements, and also with AI concerning loop design.

2.3.3 Advanced Operating Modes for the ACRR

During this quarter work was initiated to implement needed hardware changes to the ACRR transient rod drive mechanisms. These changes are necessary to accommodate the advanced modes defined for the IEFM program, and involve increasing the transient rod motor drive speed. The present motor speed can possibly be increased by about 50% although calculations indicate a factor of 2.5 is necessary and a factor of 3 is desirable in order to achieve this required capability. Consequently, information on other possible drive motors and power supplies is being assembled for future application. Furthermore, the incorporation of a motor speed programmer into the ACRR control console is also required to meet the established operating capability. As presently envisioned, this programmer will consist of 8 to 10 preselectable stages which will increment the transient motor drive speed after predetermined time intervals. Although quite simple in principle, this programmer should provide the desired operating levels established for the program once the motor drive speed capability has been increased. Implementation and testing of these hardware changes will take from 6 to 9 months.

2.3.4 Compatibility of CABRI Test Pin With the ACRR

As a part of the International Fast Reactor Safety Exchange Program an analysis has been completed to determine the capability of performing tests on the ACRR with the CABRI common test pin. Because the ACRR core height is shorter than the active region of the CABRI test pin, axial moderation of the pin with polyethylene within the ACRR was necessary to simulate the CABRI cavity spectrum. The results of the calculations are presented in Figure 2.3-1. As can be seen from the figure, the ACRR can provide a near match of the test pin axial energy deposition profile in the CABRI reactor, thus allowing for a commonality point within the multinational CABRI program.

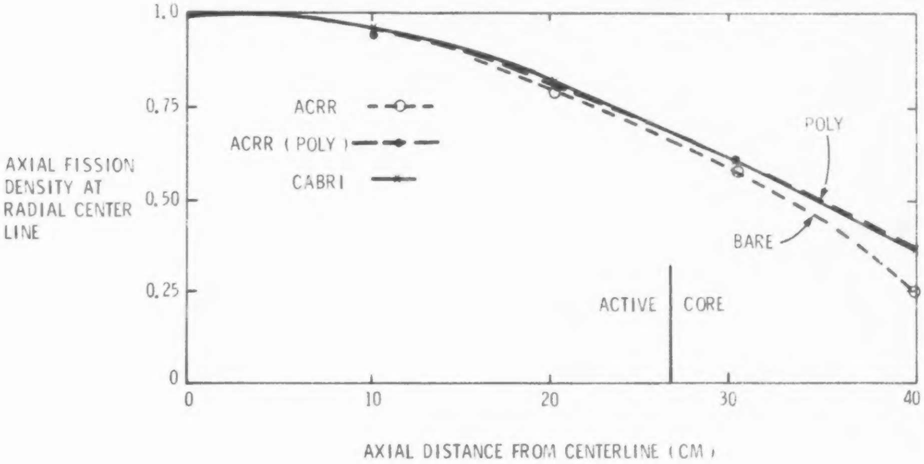

Figure 2.3-1. Axial Fission Density in CABRI A2 Test Pin in CABRI and ACRR (Polyethylene Moderated Test)

2.3.5 CABRI Analysis With EXPAND

Calculations were performed for CABRI Tests A1, A2, and A3 as part of NRC's contribution to the joint CABRI project using the EXPAND pin failure model. These calculations used the standard CABRI test pin and test reactor data as of

August 1978. The A-series tests are designed to simulate a TOP, using a single fresh UO_2 pin in a flowing sodium loop subjected to a single pulse of from 14 to 24 ms FWHM. Tests A1 and A2 are low and intermediate energy calibration tests, with Test A2 planned to just reach failure. Test A3 is to be the actual TOP simulation.

As stated in the experimental plan, Test A1 was not predicted to fail and had a maximum radial melt fraction of 27%. Test A2, which was intended to fail, was not predicted to do so; maximum life fraction and radial melt fraction were 0.004 and 69% respectively. Test A3 was predicted to fail at 208 ms past peak power with a maximum radial melt fraction of 82%.

Although Test A3 was predicted to fail, its result was a late failure and not a true simulation of a TOP failure. Because of lower than expected energy deposition in Test A1, the CABRI core is presently being reworked and the series will likely be repeated, starting with Test A1R (repeat of Test A1) using higher enrichment test pins.

2.4 Fuel Motion Detection (K. T. Stalker, 1253; J. A. Halbleib, Sr., 4231; J. E. Morel, 4231; L. M. Choate, 4423; D. A. McArthur, 4423; S. A. Wright, 4423; L. D. Posey, 4452; P. J. McDaniel, 4231)

2.4.1 In-Core Fuel Motion Detection

2.4.1.1 Introduction -- Fuel motion will be mechanically simulated in the SPR-III to test the feasibility of the in-core fuel motion detection method. Miniature in-core detectors, placed inside and around the fuel bundle, will monitor the flux changes caused by the fuel motion. The detector outputs will then be unfolded to determine an estimate of fuel motion which can be compared with the actual fuel motion. The key to this experimental program is the development of detectors which are sensitive to fuel motion and the development of unfolding techniques which can give good estimates of the fuel motion based on the detector responses. A brief description of the progress achieved in the experiment, the detector development, and the unfolding techniques will be reported.

2.4.1.2 SPR-III Fuel Motion Detection Equipment -- The start of the SPR-III fuel motion detection experiments was delayed by one quarter because of a higher priority given to a new task to develop fission couple detectors for use in the CABRI energy deposition calibration tests in France. This task is described in detail below.

During this quarter the experiment plan and safety analysis report for the seven-pin fuel motion detection experiments was presented to the SPR Safety Committee. The plan was accepted by the committee with only minor modifications and will now be presented to the Reactor Safeguards Committee. The Safeguards Committee will be asked to delegate authority to the SPR Committee to authorize approval of the 19-pin and 37-pin experiments. Following the completion of the seven-pin experiments, an addendum to the experiment plan will be submitted to the SPR Committee for approval of the larger experiments.

A few tasks need to be completed before the SPR experiments can begin. The remaining major tasks require completing the development of software for the data acquisition system, mounting the detectors in the test assembly, assembling the fuel pin position control system, and installing more instrumentation cables between the reactor and the instrumentation room. Each of these tasks is being pursued and it is hoped that the first fuel motion detection experiments can begin next quarter.

2.4.1.3 Detector Design and Development -- One of the key requirements for a successful in-core fuel motion detection program is the availability of detectors which are sensitive to fuel motion. Previous calculations showed that fast neutron detectors located near the moving fuel (a few cm) are sensitive to fuel motion.[2-4] For the past two years a development effort at Sandia has focused its attention on developing miniature fast-neutron-sensitive fission-couple detectors. Several miniature ^{238}U fission-couple detectors (FCD) were fabricated and successfully tested in the SPR-III reactor this quarter. These detectors, having an outside diameter of 1.6 mm and a length of 5 mm, are small enough to fit between the fuel pins. Because of their small size and fast-neutron sensitivity, these detectors will be sensitive to fuel motion when placed close to the fuel. Approximately 30 to 50 of these detectors are being fabricated for use in the SPR-III fuel motion detection experiments.

As part of the French CEA-GfK CABRI:USNRC ACRR International Exchange Agreement, the French have asked Sandia to help with the CABRI energy deposition calibration experiments. The purpose of these experiments is to determine the time and spatially dependent energy deposition within a fuel pin which is subjected to a simulated fast reactor accident.

To determine the time and spatially dependent energy deposition within the fuel pin, 10 neutron detectors will be placed near the fuel pin at different axial locations. The detectors will be placed in the sodium bypass loop approximately 15 mm from the fuel pin centerline. Five of the detectors will be commercially fabricated fission chambers. The remaining five detectors will be Sandia-fabricated fission-couple detectors. To be compatible with the CABRI reactor and test loop, these detectors must be sodium compatible at 300°C for 1 wk. They must also be able to withstand twenty 20-MW power runs, lasting for several minutes, followed by a reactor pulse of 7×10^{14} to 15×10^{14} nvt.

The fission chamber detectors will be specially designed to be linear in the flux range of from 2×10^{14} to 2×10^{17} nv for the CABRI spectrum. To be compatible with sodium, the detector package will be fabricated totally from Type 304L stainless steel. The detector outside diameter will be 6.35 mm; its active length will be 25.4 cm. Sandia is presently in contact with a commercial manufacturer about supplying detectors to meet Sandia specifications.

The fission-couple detectors originally developed for the fuel motion experiments will be modified to meet the requirements of the CABRI experiments. The major modifications require redesigning the detector package to make it sodium-compatible and require modifying the substrate design to increase the detector sensitivity while lowering the noise. Also, extensive testing of the detectors will be performed to test their reliability and to calibrate them.

During this quarter, new designs for the detector package substrate were made. The detector design is significantly larger than the fuel motion detector. The larger size is due chiefly to the requirement for sodium compatibility and the increased detector sensitivity. Also the uranium wire for the detectors was ordered. The wire was ordered in both naturally enriched uranium and fully depleted uranium. This allows the option of selecting the temperature rise experienced by the detector and the neutron spectrum observed.

Most of the detector design requirements have been obtained via regular communications with French co-workers at Cadarache and through the CABRI notes. Several pieces of information still need to be obtained, however, and are described below. The neutron spectrum, or group fluxes, along with the normalization is required. This information is necessary to determine the uranium enrichment in the detectors. Also, more details on the power profiles are needed to determine if the fission-couple can survive the steady-state power run and the reactor pulse. Finally, more details on the methods used to mount the detectors and bring the cables out of the sodium loop are needed. All of this information has been requested and should be coming shortly in a letter from France.

2.4.1.4 Fuel Motion Unfolding -- During this quarter, two papers were written and presented at the ORNL-RSIC seminar and workshop held in Oak Ridge, Tennessee, on the theory and application of sensitivity and uncertainty analysis.[2-4, 2-5] These papers summarized the results of the seven-pin "one energy group" model of the SPR-III fuel motion detection experiments. One of the papers described the detector response kernel generation methods, and the other paper described the unfolding methods.

At present, the "one-group" detector response kernels are available for use in the unfolding code. Previous analysis showed that the kernel generation techniques and the unfolding techniques are self-consistent and can be used to unfold noisy data. Since uncertainties in the detector response measurements carry through to the unfolded solution, there is no merit in generating detector response kernels to a greater precision than the uncertainties in the signals. Consequently, further refinements in the detector kernel techniques are not warranted until experimental data can be obtained. Experimental data should be available next quarter.

2.4.2 Electron Beam Flash X-Radiography

The investigation of the feasibility of using x-ray cinematography for material-motion detection continued during this quarter. The major emphasis of this work has been the detailed analysis of the measuring capabilities of x-ray cinematography as a diagnostic technique. The approach taken has been to identify the performance characteristics of state-of-the-art active detector systems, and then to couple these results with the resolution requirements established for DOE/NRC experimental program test matrix. In this way it has been possible to estimate performance characteristics for the x-ray source of this type of detector system.

During this quarter, work proceeded to determine the performance characteristics of a state-of-the-art active detector system with a LINAC x-ray spectrum. By coupling the performance capabilities of the active detector system to the established resolution requirements of the experimental program, the requisite x-ray source can be determined. Since the source determination is of major importance to this task, most of the work during this quarter, therefore, related to optimizing the active detector system design. The present detector system design consists of a scintillator (calcium tungstate, $CaWO_4$, was the best of many candidates studied), an optical image intensifier, and a fast framing camera with assorted coupling lenses and a mirror to turn the optical path 90° from the x-ray beam direction.

The performance studies with this active detector system have required the design and fabrication of electronic components to allow the active system to synchronously drive the linear accelerator. This is necessary to achieve a simultaneous pulse from the accelerator to a "shutter open" signal from the camera as well as in gating the image intensifier to "on" to reduce background noise between successive accelerator pulses. Figure 2.4-1 presents a schematic representation of this experimental arrangement. A brief description of the operation of the experiment apparatus is presented in subsequent paragraphs.

During this quarter, specific work with the active detector system was done to determine the minimum detectable dose necessary to produce a measurable and statistically significant change in the output film density. To determine this quantity experimentally, a series of experiments was performed at the Sandia NDT Linear Accelerator (LINAC) Facility. This facility normally provides 5, 7.5, or 10 MeV Bremsstrahlung radiation at pulse rates variable from a few up to 300 pps. To facilitate the use of this machine in these measurements, the electronics of the accelerator were modified such that the accelerator's trigger and drive circuits were under the control of an external oscillator as shown in Figure 2.4-1. By gating the external drive oscillator, a train of pulses of predetermined length could be obtained from the accelerator. Additionally, by flipping a switch, continuous accelerator operation could be restored. Using this capability, pulse trains of 1, 2, 4, 8, 16, 32, and 64 pulses were emitted, each 10 MeV Bremsstrahlung pulse being about

7 μs wide (FWHM). Use of a photodiode and oscilloscope revealed that the first pulse was either completely missing or had an energy level at least an order of magnitude lower than that of the second and subsequent pulses. The second pulse was generally about 50 to 80% of full power and after that, the pulses seem to have achieved full power. Measurements made with thermoluminescent detectors (TLD) confirmed the low power in the first pulse and subsequent power levels in the following pulse train.

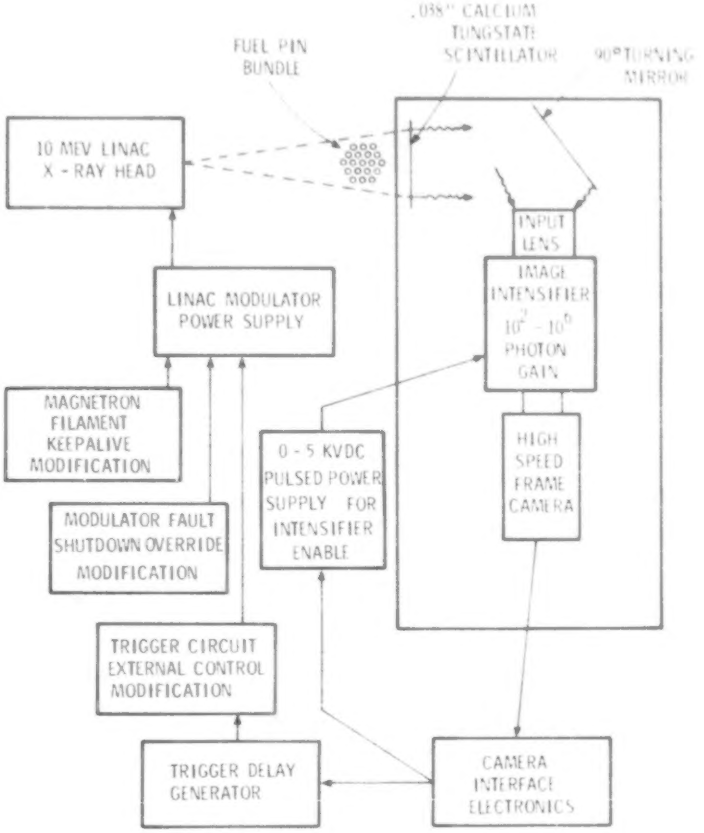
.038" CALCIUM TUNGSTATE SCINTILLATOR
FUEL PIN BUNDLE
90° TURNING MIRROR
10 MEV LINAC X - RAY HEAD
INPUT LENS
IMAGE INTENSIFIER 10^2 - 10^6 PHOTON GAIN
LINAC MODULATOR POWER SUPPLY
MAGNETRON FILAMENT KEEPALIVE MODIFICATION
0 - 5 KVDC PULSED POWER SUPPLY FOR INTENSIFIER ENABLE
HIGH SPEED FRAME CAMERA
MODULATOR FAULT SHUTDOWN OVERRIDE MODIFICATION
TRIGGER CIRCUIT EXTERNAL CONTROL MODIFICATION
TRIGGER DELAY GENERATOR
CAMERA INTERFACE ELECTRONICS

Figure 2.4-1. Fuel Pin Motion Flash X-Ray Cinematography

The target used for the preliminary tests consisted of several lead bricks placed on end to form an 8-in.-thick attenuating wall below beam center while leaving the uninterrupted beam to pass onto the scintillator above beam center (see Figure 2.4-2). The scintillator used was $CaWO_4$, about 0.6 mm thick. The actual detector system geometry (Figure 2.4-3) consisted of the scintillator, a turning mirror, an optical image intensifier, and a camera. For these tests, a 35-mm still camera was used instead of the 16-mm high-speed motion picture camera which will be used in the actual flash x-ray cinematography work. Although the cameras were different, the same film, Kodak 2484, was used in this experiment as will be used in the final cinematography system. The actual experiment consisted of firing 2, 4, 8, 16, 32, and 64 pulses through the target to the scintillator for each of three different intensifier tube voltage settings, 20 KV, 23 KV, and 26 KV corresponding to optical gains of approximately 10^2, 10^3, and 10^4 respectively. To determine the actual characteristic curve for the Kodak 2484 film under these particular experimental conditions, a calibrated density step wedge was contact printed onto a strip of the film by using a flash sensitometer which provided a close spectral match to the P-11 phosphor emission of the image intensifier tube actually used in the experiment. A 1-ms flash duration was used because this is the decay time of the phosphor and thus the exposure time for film exposed to short duration events. After exposure, the film was developed under the same conditions as the calibration test films.

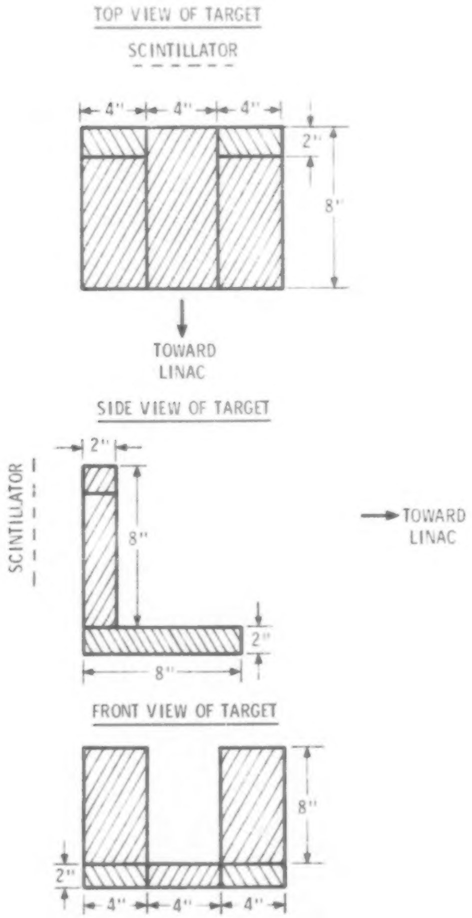

Figure 2.4-2. Lead Brick Target Used in Detector Studies With LINAC

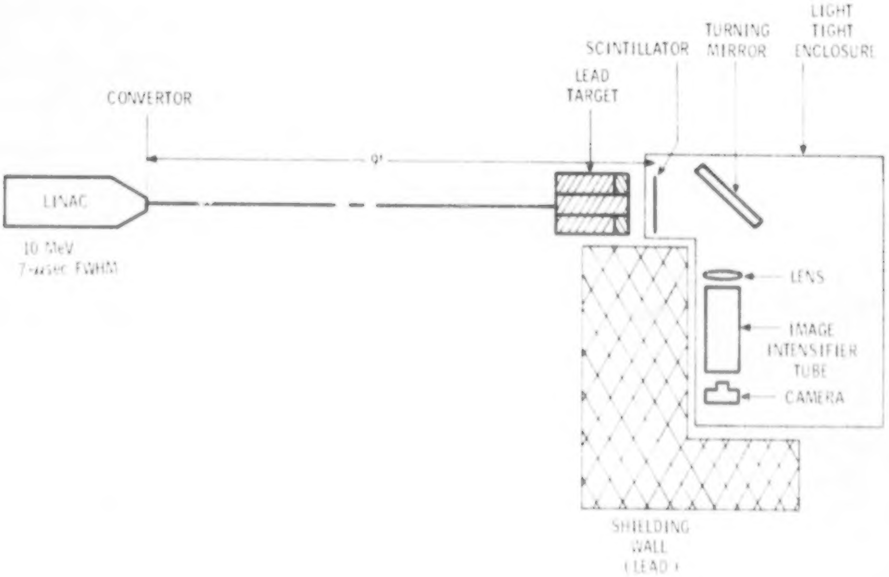
LIGHT TIGHT ENCLOSURE
TURNING MIRROR
SCINTILLATOR
LEAD TARGET
CONVERTOR
9'
LINAC
10 MeV
7-μsec FWHM
LENS
IMAGE INTENSIFIER TUBE
CAMERA
SHIELDING WALL (LEAD)

Figure 2.4-3. LINAC and Active Detector System Geometry (Top View)

The data analysis consisted of measuring the specular density of both the sample data obtained at the LINAC and the calibration step wedge with a Perkin Elmer PDS Microdensitometer. A 50-μm square aperture was used in the scanning which obtained 201 data points across each step of the calibration film as well as in each frame of film representing the scintillator of the active detector system uniformly illuminated by 10-MeV x-rays. Each scan was statistically analyzed to produce the mean, variance, and standard deviation of each set of 201 data values. The results of these scans produced the data in Tables 2-III and 2-IV and the film's characteristic curve for the particular experimental conditions shown in Figure 2.4-4.

Table 2-III shows that the standard deviation in film density, δ_D, is about 0.03 initially with a gradual rise to about 0.06 as film density increases. This standard deviation is a measure of the graininess of the film and agrees well with the published value from the Kodak literature for 2484 film. Table 2-IV shows the results from the LINAC data. This data shows a standard deviation which is measurably higher than that for the film exposed to light alone, and indicates the presence of other noise sources such as quantum statistics or electronic noise in the image intensifier tube.

CONTENTS

Page

FOREWORD 11 1/A12

EXECUTIVE SUMMARY 13 1/A14

1. ENERGETICS 39 1/C12
    1.1 Prompt Burst Energetics 39
    1.2 Equation-of-State 51 1/D12

2. FUEL DYNAMICS 67 1/E14
    2.1 Fuel Disruption 67
    2.2 Transition Phase 75 1/F8
    2.3 Initial and Extended Fuel Motion 85 1/G4
    2.4 Fuel Motion Detection 88 1/G7

3. CORE DEBRIS BEHAVIOR - INHERENT RETENTION 105 2/A12
    3.1 Molten Core Technology 105
    3.2 PAHR Debris Bed 127 2/C10
    3.3 PAHR Molten Pool 135 2/D4
    3.4 Containment Analysis 141 2/D10
    3.5 Fragmentation 142 2/D11
    3.6 Sodium Containment and Structural Integrity 147 2/E2

4. AEROSOL SOURCE NORMALIZATION 159 2/E14

5. ELEVATED TEMPERATURE DESIGN ASSESSMENT 163 2/F4

6. LMFBR ACCIDENT DELINEATION 175 2/G2

7. TEST AND FACILITY TECHNOLOGY 193 3/A8
    7.1 ACPR Upgrade - Initial Test and Operations 193
    7.2 ACPR Fuel-Motion Detection System 193
    7.3 Large-Scale Test Assessment 195 3/A10

Table 2-III

2482 Film Characteristics Scanned With 50- by 50-μm Aperture, 201 Data Points

Step No.	Log$_{10}$ Energy (ergs/cm^2)	Mean Density	Variance	Standard Deviation
1	-3.58	0.56	0.00102	0.0320
2	-3.43	0.57	0.00186	0.0431
3	-3.28	0.58	0.00082	0.0287
4	-3.11	0.61	0.00106	0.0325
5	-2.96	0.65	0.00097	0.0312
6	-2.80	0.73	0.00105	0.0324
7	-2.66	0.82	0.00132	0.0363
8	-2.49	0.98	0.00137	0.0371
9	-2.33	1.16	0.0070	0.0412
10	-2.16	1.34	0.00148	0.0384
11	-1.99	1.55	0.00170	0.0412
12	-1.82	1.76	0.00205	0.0453
13	-1.66	1.99	0.00277	0.0527
14	-1.50	2.24	0.00230	0.0479
15	-1.34	2.48	0.00261	0.0511
16	-1.17	2.69	0.00330	0.0574
17	-1.01	2.83	0.00526	0.0725
18	-0.86	2.96	0.00396	0.0628
19	-0.70	3.05	0.00391	0.0625
20	-0.54	3.14	0.00325	0.0570
21	-0.38	3.25	0.00348	0.0590
22	-0.22	3.32	0.00382	0.0618
23	-0.07	3.39	0.00314	0.0561
24	+0.09	3.45	0.00349	0.0591
25	+0.24	3.51	0.00305	0.0552

Table 2-IV

LINAC Film, 2484, Three Gains
Scanned With 50- by 50-μm Aperture, 201 Data Points

Gain Positive (kV)	Number of Pulses	Mean Density	Variance	Standard Deviation
20	2	0.48	0.00091	0.0302
20	4	0.55	0.00104	0.0323
20	8	1.04	0.00522	0.0723
20	16	1.64	0.00495	0.0704
20	32	2.11	0.00613	0.0783
20	64	2.42	0.00682	0.0826
23	2	0.66	0.00299	0.0547
23	4	1.82	0.00694	0.0833
23	8	2.42	0.00816	0.0903
23	16	2.90	0.00572	0.0756
23	32	3.16	0.00394	0.0628
23	64	3.33	0.00448	0.0669
26	2	1.27	0.00856	0.0925
26	4	2.79	0.00633	0.0796
26	8	3.22	0.00392	0.0626
26	16	3.35	0.00379	0.0616

To determine minimum detectable energy change at the scintillator, the mean density and a density one standard deviation above and below the mean are projected backward through the characteristic curve to determine the mean and an upper and lower bound for the logarithm of exposure (Log E) (see Figure 2.4-4). The Log E value is then converted to actual exposure followed by the use of the percentage uncertainty in exposure to produce the measured change in density of one standard deviation. By correlating exposure with dose to the scintillator for each gain, the uncertainty in dose corresponding to a one-standard deviation change in density can be computed. This computation was done and the results are presented in Table 2-V. Data derived from TLD measurements were used to accomplish the dose-exposure conversions. Table 2-V data indicate that the percent of uncertainty is approximately constant for a given gain setting within the linear portion of the characteristic curve. If the minimum detectable dose is defined as twice the uncertainty (two density values separated by their respective uncertainties can just be distinguished), the minimum detectable dose varies from about 0.6 mR for a 1.5-mR dose at a 26-kV gain setting to 30 mR for a 100-mR dose at a 20-kV gain setting. Although the conclusions to be reached from preliminary findings pertaining to source requirements necessitate further analysis, the data behavior can be explained. Since the film grain noise appears to be a major factor, the percentage uncertainty does not change significantly as the gain changes because grain noise is approximately constant; yet when the gain is raised there appears to be some slight increase in uncertainty corresponding to an increase in quantum fluctuations caused by the fewer quanta required to produce a given mean film density. As can be seen from this experiment, the film used is of great importance to the minimum dose measured because of both its granularity characteristics and the slope of its characteristic curve, the steeper the slope the less the Δ Log E for a given granularity-caused ΔD. Kodak 2484 film was chosen because of the high film speed required to produce motion pictures at one frame per 1.5 mR pulse of the LINAC. Since the granularity of other films in this speed range is about the same, film grain noise will continue to make a major contribution to the uncertainty in dose measurements made by this detector system.

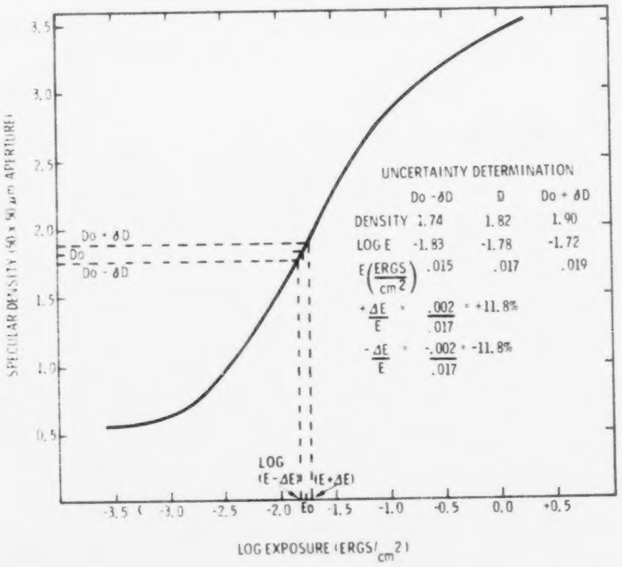

Figure 2.4-4. Characteristics of Kodak 2484 Film Developed for 6 Minutes in Developer D-19 at 68°F (20°C)

Table 2-V

LINAC Data, 2484 Film, Three Gains

No. of Pulses	Dose (mR)	Mean Exposure (ergs/m^2)	ΔExposure (%)	ΔDose (mR)
20 kV				
4	4.4			
8	8.7	3.6×10^{-3}	+14.82, -16.82	+1.29, -1.46
16	20.6	1.23×10^{-2}	+14.32, -11.90	+3.05, -2.45
32	48.6	2.63×10^{-2}	+12.20, -10.87	+5.93, -5.28
64	100	3.98×10^{-2}	+14.82, -12.90	+14.8, -12.9
23 kV				
2	1.5	1.258×10^{-3}	+25.9, -36.9	+0.39, -0.55
4	4.4	1.68×10^{-2}	+11.90, -10.71	+0.52, -0.47
8	8.7	3.98×10^{-2}	+23.03, -30.8	+2.0, -2.68
16	20.6	1.23×10^{-1}	+28.87, -35.4	+5.91, -7.3
32	48.6	3.16×10^{-1}	+20.3, -20.6	+9.9, -10.0
64	100	6.31×10^{-1}	+34.90, -24.01	+35, -25
26 kV				
2	1.5	6.0×10^{-3}	+18.8, -20.56	+0.28, -0.31
4	4.4	8.9×10^{-2}	+23.03, -22.38	+6.01, -0.98
8	8.7	3.76×10^{-1}	+30.32, -15.96	+2.67, -1.39

2.4.3 Coded Aperture Imaging

2.4.3.1 Introduction -- The Coded Aperture Imaging task is concerned with the imaging problems which are expected in large LMFBR safety test experiments (those with more than seven LMFBR fuel pins). Imaging in these large tests is anticipated to differ significantly from one-pin to seven-pin tests because of the greater scattering and absorption of the imaging radiation within the larger bundles of test fuel pins, and because of the greater complexity of the image itself. Coded aperture imaging of both gamma rays and neutrons is being studied.

In gamma-ray imaging studies, a 37-pin bundle was chosen as a representative example of a larger test. Calculational tools developed earlier in the program have been applied to analyze expected signal levels and signal changes resulting from voiding of fuel, sodium, and steel in various combinations and amounts. The calculations use realistic material compositions and geometries for the test fuel bundle and the coded aperture imaging system, and detailed Monte Carlo methods for gamma-ray transport. This detail in the calculations has permitted realistic treatment of scattering and absorption in the test fuel and its containment and has also allowed variation of coded aperture system parameters to optimize detection of changes in fuel geometry. These studies are expected to define the limitations of gamma-ray imaging, and the calculational results will be verified by experiments on reactor facilities such as PARKA. Successful completion of this program is expected to result in an optimized gamma-ray coded aperture system for high-resolution imaging in large-bundle tests.

During this quarter, a topical report on the gamma-ray transport calculations was prepared and detailed planning for verification experiments was begun.

Imaging of fast neutrons is desirable in large-bundle tests because fission neutrons have a somewhat greater scattering length than fission gamma rays, and because fast neutron emission is more directly characteristic of the fuel geometry. The goal of the neutron imaging portion of this program is to image fast neutrons with minimal backgrounds from slow neutrons or gamma rays, by making use of the greater sensitivity of the coded aperture technique.

Experimental and theoretical work is designed to investigate the feasibility of imaging fast neutrons with coded aperture techniques, and has been concentrated in two main problem areas: (1) development of coded apertures which have high spatial resolution (~ 2 to 3 mm) and a wide field of view, yet which can modulate fast neutrons sufficiently to yield good images; (2) development of a transient fast neutron detection system with minimum backgrounds caused by slow neutrons and gamma rays. Work performed in previous quarters has shown that steel, tungsten alloy, and polyethylene are good candidate coded aperture materials, and that a good threshold fast neutron detector for static images consists of a depleted uranium foil in contact with a sheet of Lexan plastic to record the image. Apparatus has been developed to make static fast neutron images of a ^{252}Cf source with candidate neutron coded apertures. The chemical steps in processing the Lexan have also been varied over a wide range in an effort to reduce spurious backgrounds in the Lexan.

During this quarter, a major milestone of the neutron imaging program was reached by successfully reconstructing a low-background-level image of the ^{252}Cf source by using only fast neutrons ($E_n \gtrsim 1.5$ MeV).

2.4.3.2 Gamma-Ray Coded Aperture Imaging -- A topical report on the gamma-ray transport calculations was completed during this quarter, and is now in the process of administrative review prior to publication. A much shorter report on both the neutron and gamma-ray work through December 1977 was also prepared.

Sandia staff personnel visited the PARKA facility at LASL to become familiar with operating limits, experiment design conditions, and schedule. The shielding and the amount of space available for experiments appear to be adequate. The present hodoscope collimator must be removed and replaced with a coded aperture collimator, a major effort since much shielding must be moved.

Because of fission product release limits, the power per resolution element of the test fuel obtained with PARKA appears to be only about 3% of that obtained with the ^{252}Cf source (for all day steady PARKA operation). Therefore, a scintillator/image intensifier system similar to that used on the new ACRR coded aperture system will probably be required for efficient data collection.

For the complex images expected from larger test fuel bundles, an off-axis Fresnel aperture has potential advantages during image reconstruction. Since the spatial frequency response of an off-axis aperture is not uniform, the image quality may suffer. This particular problem can be studied with optical mockups of both the coded aperture and the expected source distributions. Therefore, accurate optical transparencies of candidate off-axis apertures and of fuel pin bundles have been made in preparation for the detailed study of this problem.

2.4.3.3 Fast-Neutron Coded Aperture Imaging

2.4.3.3.1 Static Neutron Imaging Studies -- Figure 2.4-5 shows the reconstructed image of the ^{252}Cf source obtained by imaging neutrons with energies

$\gtrsim$ 1.5 MeV. The depleted uranium/Lexan fast neutron detector was used, and the coded aperture was an off-axis one-dimensional Fresnel code made of 2.54-cm-thick tungsten vanes, as described in the previous quarterly report. The calculated resolution of this aperture is 0.33 cm, but further measurements will be required to determine the actual resolution obtained in these initial experiments. This is believed to be the first coded aperture image obtained solely with fast neutrons. Although the image in Figure 2.4-5 has a low background, the signal-to-noise can in principle be improved a great deal before reaching the statistical limit set by the number of fission fragments detected. This improvement should be obtainable by optimizing the photographic processes to increase the brightness of the reconstruction and reduce optical noise.

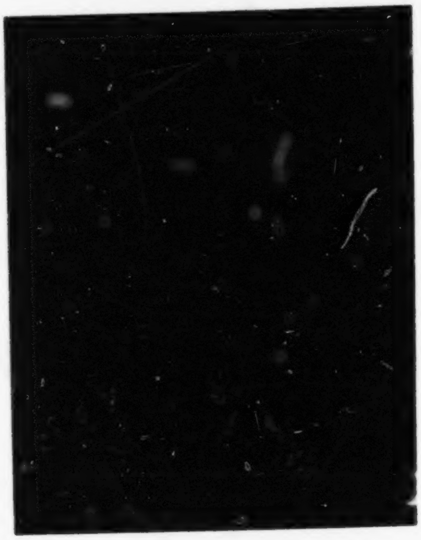

Figure 2.4-5. Reconstructed Image of the ^{252}Cf Source Obtained by Imaging Neutrons With Energies $\geq$ 1.5 MeV

This initial fast-neutron coded aperture image was obtained on a fine grain, high contrast film having a low-phase-distortion base material to make the pseudohologram (Kodak Minicard-II). The brightness of the reconstructed image was also greatly enhanced by bleaching the Minicard-II pseudohologram. The very slow speed of this film and its blue-sensitive spectral response required that a 35-mm projector lamp be used to illuminate the Lexan during photoreduction. The pseudohologram exposure must be correct within about a factor of 2 to obtain a high-quality image. With Minicard-II film a liquid gate does not improve the image quality significantly.

The major cause of the excess noise observed in these initial neutron image reconstructions seems to be spurious light scattering from the Lexan surface. This spurious scattering varies in intensity from sample to sample and seems to be caused by the protective paper applied to the Lexan during manufacture. This effect would be absent from the various transient fast neutron detectors being studied in the other phase of the neutron coded aperture program. However, some effort to reduce the spurious Lexan scattering will probably continue because the track-etch type detector using polycarbonates is so insensitive to gamma-ray and alpha particle backgrounds. Such a detector is therefore a very useful standard against which to compare the other transient fast neutron detector concepts.

The attainment of a reconstructed fast neutron image shows that one can modulate the fast neutrons adequately with structures containing high spatial frequencies and can record the resulting pattern in a form which readily allows analog reconstruction with a laser. Further work with static neutron imaging must be done to define the limits of spatial resolution obtainable and the relationship between image signal-to-noise and fast neutron fluence.

2.4.3.3.2 Transient Fast Neutron Detector Development -- The two general types of transient fast-neutron detectors under consideration are the thin-fission-fragment scintillator[2-6] and the recoil-proton scintillator. These two types of detectors will be used initially to make static neutron images of the ^{252}Cf source for comparison with the Lexan neutron images already being obtained. Substantial shielding of these scintillators and the camera system used to record the images may be required, because of the large gamma-ray background. The intensity of light emitted by the thin scintillator when irradiated by fission fragments must also be measured to determine the feasibility of this concept.

During this quarter, components of the remotely-operated 35-mm camera system to be used in the ^{252}Cf source experiments were tested and proved satisfactory. Theoretical detector efficiency calculations were performed for several possible detector geometries, to help define the expected limiting signal-to-noise in various imaging situations. The optimized detector geometries thus obtained will also be used to calculate the expected gamma-ray sensitivity of each detector concept. NE-102 and Pilot-B scintillators have been obtained, and experiments with the ^{252}Cf source should begin during the next quarter.

References for Section 2

2-1. Advanced Reactor Safety Research Program Quarterly Report, October - December 1977, Advanced Reactor Research Department, SAND78-0611, Sandia Laboratories, Albuquerque, NM, October 1978.

2-2. Advanced Reactor Safety Research Program Quarterly Report, January - March 1978, Advanced Reactor Research Department, SAND78-1421, Sandia Laboratories, Albuquerque, NM, to be published.

2-3. Advanced Reactor Safety Research Program Quarterly Report, April - June 1978, Advanced Reactor Research Department, SAND78-2001, Sandia Laboratories, Albuquerque, NM, to be published.

2-4. W. H. Scott, Jr., P. J. McDaniel, J. H. Renken, and S. A. Wright, "Sensitivity Analysis Applied to the Calculation of Detector Response Kernels," RSIC Seminar-Workshop on the Theory and Application of Sensitivity and Uncertainty Analysis, Oak Ridge, TN, August 22-24, 1978.

2-5. P. J. McDaniel and S. A. Wright, "Fuel Motion Unfolding Based on Point Detector Responses," Transactions of the Theory and Application of Sensitivity and Uncertainty Analysis Seminar, Oak Ridge, TN, August 1978.

2-6. B. W. Wehring, P. E. Rohan, N. L. Shapiro, and M. E. Wyman, Nucl. Instr. and Methods, 62, p. 330, 1968.

3. CORE DEBRIS BEHAVIOR - INHERENT RETENTION

3.1 Molten Core Technology (D. A. Powers, 5831; A. W. Mullendore, 5832)

3.1.1 Introduction

The agressive behavior of molten materials has been the focus of the study of the interaction of core materials with concrete. However, a phase arises in any core-meltdown accident at which the internal heat generation by fission products is insufficient to maintain the core materials in the molten state. The convenient assumption is often made that significant core debris/concrete interactions cease when this state is reached. Such an assumption ignores the observed temperature ranges of concrete melting which are less than the solidification temperatures of core-melt constituents.

3.1.2 Status of the "BURN" Test Series

The "BURN" series tests are small-scale experiments intended to develop instrumentation and techniques for the quantitative study of melt/concrete interactions. Major issues being explored in this test series include:

- Development of sustained material interactions methods
- Development of x-ray techniques for real-time monitoring of melt/concrete interactions
- Study of the interaction between hot, but not necessarily molten, core debris and concrete.

Several of the BURN tests have been described previously.[3-1] In this report, descriptions of other tests are presented, and the results of all tests are summarized. Results of the tests have shown the need for further experimentation, and future tests in the BURN series are described.

3.1.3 Experimental Methods

Crucibles used in the experiments were cut from 6-in.-diameter, 12-in.-long concrete testing cylinders cast when other concrete fixtures used in the experimental program were fabricated. Crucible cavities are typically 3-1/2 in. in diameter and 6 to 7 in. long. Instrumentation used in the tests has been varied according to the needs of the experiment. All tests were instrumented with thermocouples necessary to monitor the directional nature of concrete erosion and concrete thermal response.

Tests conducted thus far in the BURN series are summarized in Table 3-I. Tests BURN 1 and BURN 2 have been discussed elsewhere[3-1] and are addressed further in this report. Other BURN tests are also discussed and the results of Tests BURN 0, 3, and 4 are described below in detail.

Test BURN 1 was a successful demonstration of an x-ray technique that allows real-time, continuous observation of a high-temperature melt in contact with concrete. Melt behavior, gas flow behavior, and concrete interfacial behavior were readily visible in this test. All of these processes must be adequately known if a computer model is to be devised to extrapolate experimental results to realistic situations.

The success of Test BURN 1 led to plans for additional tests using the x-ray technique. Not all the details of these experiments have been resolved. Three tests are planned and a possible test matrix for this test series (the x-ray series) is shown in Table 3-II. Sustained melt/concrete interaction tests are not among these alternatives due to equipment limitations.

The other BURN tests have been attempts to determine what techniques may be used to sustain interactions between molten core materials and concrete. To do this requires that additional heat be supplied to the melt. Two techniques for supplying this heat have been tried:

Joule heating - Test BURN 0
Induction heating - Tests BURN 2, 3, and 4.

Induction heating was clearly successful in heating metallic core materials in contact with concrete. Rapid heating of cold metal on concrete (0.3 to 3°C/s) could be achieved up to the point at which concrete adjacent to the metal began to melt.

Table 3-I

Summary of BURN Tests

Test	Concrete	Objective	Remarks
BURN 0	Limestone	Sustain a thermitically generated corium melt at temperature, using Joule heating supplied via two tungsten electrodes buried in concrete. Also observe interaction between corium melt and candidate refractories - W_2B, HfC, Y_2O_3, ZrO_2 (CaO).	Wild variation in resistivity of oxidic phase made control of the DC power supply difficult. After ~ 30 s overload occurred and the test was terminated.
BURN 1	Limestone	Use x-ray imaging technique to observe melt/concrete interface in real-time.	Test BURN 1 was quite successful. Brief results and collateral data reported in Reference 1.
BURN 2	Limestone	Use inductive heating to warm steel up to near its melting point while in contact with concrete. Test simulated both the interaction of fragment debris beds with concrete and the interaction of core melts late in an accident when melt solidification occurs and the concrete has been largely dehydrated.	Test BURN 2 was quite successful. Data have been reported in Reference 1. Erosion of concrete began at ~1300°C - a temperature below the liquidus of concrete but well above solidus. Downward erosion ~ 3 cm/hr. Radial erosion, 1.7 cm/hr.
BURN 3	Generic Southeastern United States Concrete	Similar to Test BURN 2 with a more refractory concrete and with more extensive instrumentation.	Result analogous to those of Test BURN 2 reported below.
BURN 4	Generic Southeastern United States Concrete	Deposit a thermitically generated melt into concrete and sustain that melt by inductively heating metallic phase.	Prompt gas release at the time of melt impact on the concrete caused the melt to be expelled from crucible cavity. Instrumentation leads from crucible were destroyed and the test was terminated.

Table 3-II

Summary of Planned X-Ray Tests

Test	Concrete	Crucible	Objective
XR-1	Basaltic	16 in. diameter; 18 in. high cavity; 8 in. diameter; 12 in. high. Melt head to be at least 4 in.	Determine radial and downward erosion rate. Use cavity diameter sufficient to include at least three nodes predicted by the gas film model for heat transfer from melt to concrete. Have sufficient melt head that gas bubble diameters in the melt are small. Measure heat flux and correlate result with observed melt behavior. Correlate gas behavior observed in the melt with gas composition and flow rates.
XR-2	Limestone	Identical to XR-1	
XR-3	Basaltic	Spherical cavity 8 in. in diameter.	Same as Tests XR-1 and XR-2. Also determine influence of geometry and melt head on results.

At this temperature, the metal temperature stabilized and additional heat supplied to the metal was conducted away by liquified concrete and consumed at least partially in melting more concrete. When the melting temperature range of the concrete was below the solidification temperature of the metal (Test BURN 2), the metal remained solid. When concrete melted at temperatures above the liquidus of the metal (Test BURN 3), a fully developed two-phase molten pool formed.

The inability to superheat the melt may be due to equipment limitations, experimental design, or the operative physics during melt/concrete interactions. Further, tests using inductive heating will minimize the second of these possibilities and hopefully maximize the use of existing equipment capabilities. An important milestone in this test program will be reached when experiments with larger crucibles are completed.

The BURN tests in which the core materials were heated from a cold start have yielded very useful information. Test BURN 2 demonstrated that core materials need not be molten to erode the concrete or to cause the liberation of substantial volumes of gas. Tests BURN 2 and 3 showed that the onset of erosion is dependent on the melting properties of the concrete. Erosion of any significant nature began at temperatures above the solidus temperature of concrete yet below the liquidus temperature of the concrete as determined by differential thermal analysis. These observations will have significant impact on modeling long term behavior of melt/concrete interactions and the interaction of fragmented debris beds with concrete.

Adequate modeling of the processes observed in Tests BURN 2 and 3 cannot be done at this time without improved data concerning upward heat fluxes. Data from Test BURN 3 suggest that the time variation of this upward heat flux is complex.

Little success has been achieved in first forming a high-temperature melt, then depositing it into concrete, and sustaining it inductively. A considerable redesign of the test arrangement used in Test BURN 4 will be necessary if this experimental operation is to be useful. Gases liberated during the initial contact between the melt and concrete must be vented without being allowed to expel melt from the heating region of the induction coil. Melt generation within the crucible cavity is not especially useful since the volume of melt created would be too small for adequate inductive coupling. Techniques such as those used in the NSS test series[3-2] may be useful in solving this problem.

Test BURN 0 was an attempt to use Joule heating to sustain a thermitically generated corium melt. This test failed due to limitations in the experimental equipment which did not permit rapid control of current flow between tungsten electrodes used in the test. Attempts are now being made to overcome these equipment limitations. Some combinations of inductive and Joule heating may be a suitable solution. Joule heating is a subject of some interest since it can be used to simulate internal heat generation in oxidic phases.

Future tests planned in the BURN series are summarized in Table 3-III. Tests BURN 5 and 6 will be similar to Tests BURN 2 and 3. Instrumentation applied to these tests will include monitors of gas generation, gas composition, and upward heat flux. The latter is proving to be an essential parameter to performance of heat balance calculations on the tests.

Test BURN 7 will interact powdered UO_2 and granular stainless steel with concrete. Power will be supplied to the system by inductively coupling to the metal phase. Specific phenomena to be addressed in the test are:

- Crust formation via sintering in UO_2
- Core debris stratification
- UO_2 dissolution in molten concrete
- Steel oxidation.

The initial bed is planned to be well mixed. Evidence from other sources[3-3] indicates that upon melting the stainless steel stratification will occur. As melting of the concrete begins, the core debris may stratify into a three layer bed.[3-4] Ultimately, the debris will evolve into a liquid metal layer covered by a liquid oxide layer.

Test BURN 8 will be similar to Test BURN 7 except an attempt will be made to use both inductive heating and Joule heating. The metal phase will be inductively heated to about 1273 K (1000°C). At this point, the oxidic phase will be conductive and may be heated by Joule techniques.

Table 3-III

Future BURN Series Tests

Test	Concrete	Objective
BURN 5	Basaltic	Similar to Tests BURN 2 and 3. Rates of gas evolution as well as concrete erosion will be monitored throughout the test.
BURN 6	Generic Southeastern United States Concrete	Similar to Test BURN 5.
BURN 7	Choice based on results of BURN 5 and BURN 6	Interaction of corium E composition powder bed with concrete. Heating supplied by inductively heating metallic phase which will consist of 100 mesh, Type 304 stainless steel powder. Both Tests BURN 7 and 8 will follow test in the CATH series being done for the Advanced Reactor Safety Branch of the NRC.
BURN 8	Choice based on results of BURN 7	Similar to Test BURN 7 except additional heat provided by Joule heating of oxidic material in melt.
BURN 9, 10	Basaltic and Limestone	Sustained interaction of thermitically generated melt. Inductive heating techniques will be used. Crucible design will be quite different than in other BURN tests.

The small size of the crucibles used in the BURN series tests may not permit sustaining interactions for periods long enough to allow all pertinent phenomena to fully develop. For this reason, Tests BURN 3 and 10 will use crucibles with cavities 8 in. in diameter and 12 in. long. Melt masses will be on the order of 13.6 kg (30 lb).

3.1.4 Preliminary Results of Sone Tests in the BURN Series

Preliminary results from Tests BURN 0, 3, and 4 are presented below.

3.1.4.1 Test BURN 0 -- A schematic diagram of the crucible used in Test BURN 0 is shown in Reference 3-5. A limestone concrete crucible 6 in. in diameter and 12 in. long with a 3-13/16-in. diameter, 5-1/4-in.-deep cavity was used. Half-inch-diameter holes about 1-1/8 in. long were drilled in the bottom of this cavity. These holes were filled with 1/2-in.-diameter rods of the following refractory materials:

- ZrO_2 (CaO stabilized) (rod 1.545 in. long)
- Y_2O_3 (rod 1.50 in. long)
- WB_2 (rod 1.695 in. long)
- HfC (rod 1.610 in. long)

A photograph of samples of these materials in place is shown in Figure 3.1-1. These materials were tested for compatibility with the high-temperature corium melt during the test.

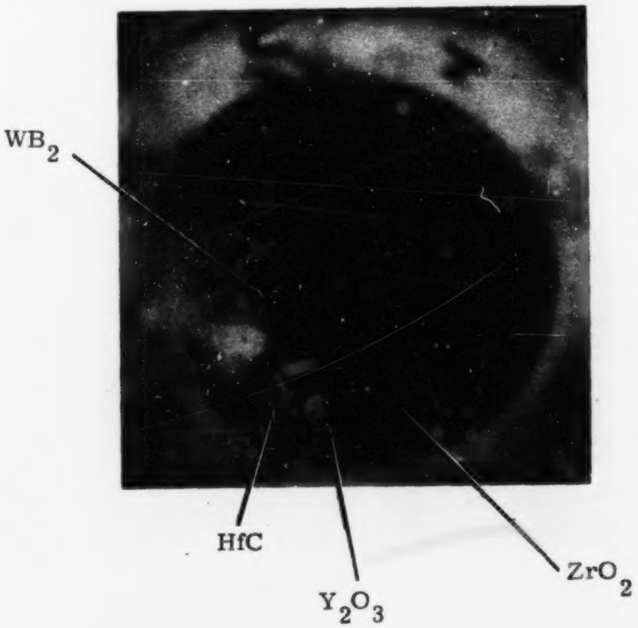

Figure 3.1-1. Locations of Refractory Specimens in Test BURN 0

On opposite sides of the crucible cavity, 1/2-in.-diameter holes were drilled through the crucible walls. Tungsten electrodes (< 1/2-in. diameter) sheathed with SiO_2 tubes having 1-mm thick walls were cemented in these holes with Saureisen No. 63 castable refractory. The electrodes were connected to a 300-A direct current power supply.

The crucible was capped with an instrumentation tower similar to, but smaller than, that used in the NSS test series. No instrumentation was mounted in this tower. The test was an attempt to demonstrate Joule heating techniques and somewhat incidently the compatibility of refractories with the melt.

The initial melt was generated by using 5 kg of the corium thermitic composition described elsewhere.[3-5] Under ideal conditions, the melt would have a composition of 54 weight percent UO_2, 17 w/o ZrO_2, and 30 w/o stainless steel. The reaction mixture was ignited with Pyrofuze.

About 15 s after ignition, the tungsten electrodes were energized. The electrodes were operated at 10 to 20 V for about 30 s. At that time excessive power demands were placed on the power supply and the test was terminated.

Posttest x-rays of the crucible are shown in Figures 3.1-2 and 3.1-3. From these x-rays, the following observations concerning refractory compatibility with the melt may be made:

- Zirconia rod is gone - probably floated during test
- Yttria rod thermally fractured
- Tungsten boride rod chemically attacked
- Hafnium carbide rod thermally fractured and chemically attacked.

3.1.4.2 Test BURN 3 -- Test BURN 3 was quite similar to a previously described Test BURN 2, except that the crucible was fabricated from the so-called CRBR composition concrete. A steel slug within the cavity of the crucible was heated by an induction coil energized with a 50-kW 3000-Hz Inducto 50 power supply.

The induction coil and crucible were packed in dry-ram insulation as depicted in Figure 3.1-4. Physical sizes of the experimental fixture are listed in Table 3-IV.

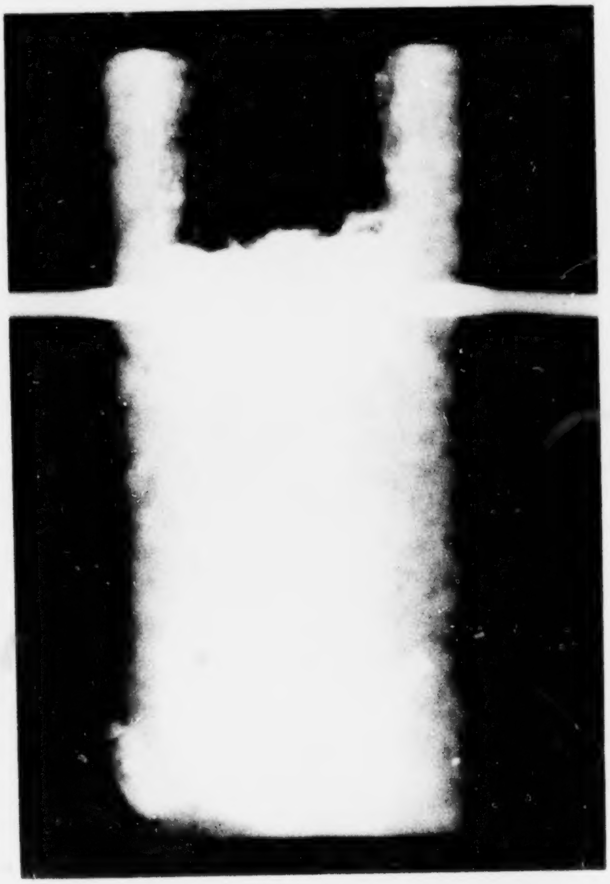

Figure 3.1-2. Posttest X-Ray of BURN 0 Crucible

Instrumentation used in the test consisted of thermocouples embedded in the concrete to detect movement of the melt. Locations of these thermocouples are described in Table 3-V.

An attempt was made to monitor differentially the response of concrete to the heat flux from the inductively heated steel. A thermocouple located within an aluminum oxide filled, 1/4-in.-ID fused silica tube mounted 1 in. below the bottom of the crucible cavity was differentially coupled to a thermocouple in the concrete. The thermocouple in the concrete was also 1 in. below. The bottom of the crucible cavity in a 0.083-in. diameter hole packed with concrete powder.

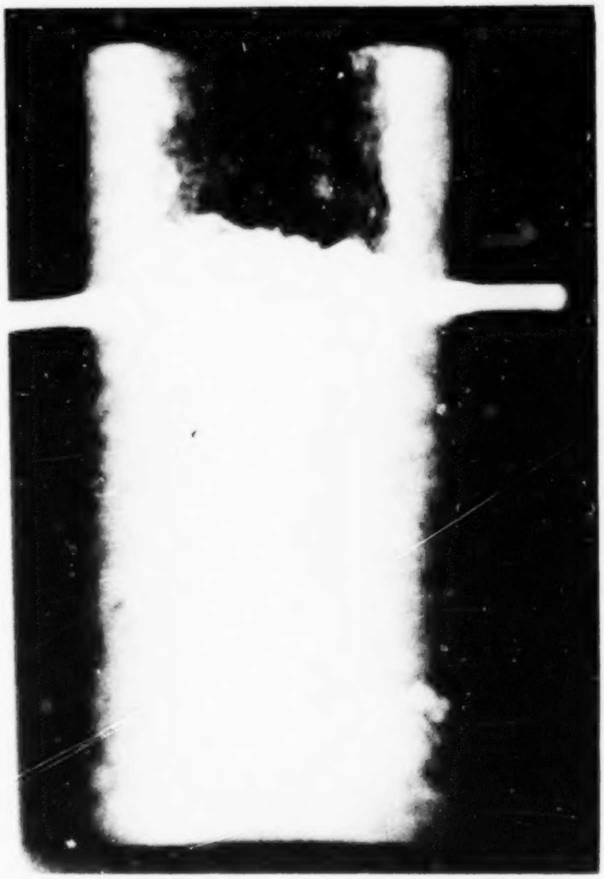

Figure 3.1-3. Posttest X-Ray of BURN 0 Crucible

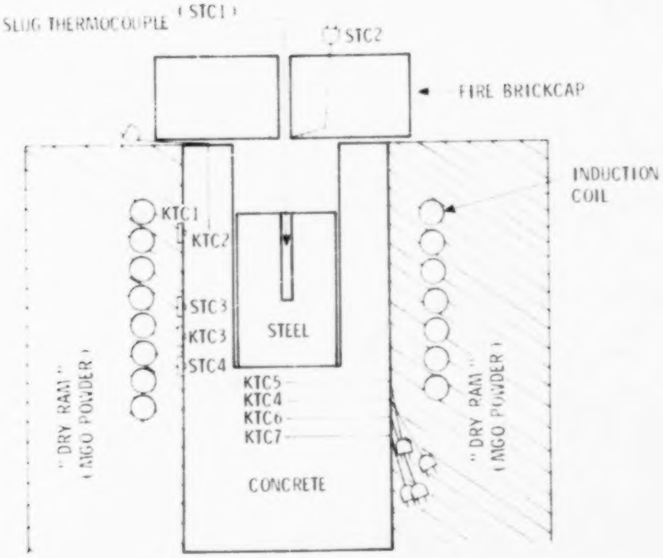
SLUG THERMOCOUPLE (STC1)
STC2
FIRE BRICKCAP
INDUCTION COIL
KTC1
KTC2
STC3
KTC3
STC4
STEEL
KTC5
KTC4
KTC6
KTC7
CONCRETE
"DRY RAM" (MGO POWDER)
"DRY RAM" (MGO POWDER)

Figure 3.1-4. Schematic of Test Fixture Used in Test BURN 3

Table 3-IV

Test BURN 3 Fixture Dimensions

Crucible length	12 in.
Crucible diameter	6 in.
Cavity depth	6-1/2 in.
Cavity diameter	3-1/4 in.
Slug length	4-1/2 in.
Slug diameter	3 in.
Slug weight	5 kg
Depth of thermocouple well in slug	2-1/2 in.
Thickness of firebrick cap on crucible	2-1/2 in.
Top of induction coil from top of crucible	2-1/2 in.
Bottom of induction coil from top of crucible	8-1/2 in.
Induction frequency	3000 Hz
Concrete type	Generic Southeastern United States calcareous

Only thermocouples whose outputs were recorded after acquisition by integrating digitizers yielded useful data. Thermocouples connected directly to recording devices became coupled to the induction heater and yielded data too noisy to be of use. Useful data from the following thermocouples are shown in the indicated figures:

- Thermocouple in the steel slug (Figure 3.1-5)
- Thermocouple in the firebrick capping assembly (Figure 3.1-6)
- Thermocouple on the external crucible wall 1/4 in. above the bottom of the crucible cavity (Figure 3.1-7)
- Thermocouple on the external crucible wall 1 in. above the bottom of the crucible cavity (Figure 3.1-8)
- Thermocouple 1 in. below the bottom of the crucible cavity near the centerline of the crucible (Figure 3.1-9).

Table 3-V

Thermocouples Used in Test BURN 3

Thermocouple	Type	Location[(a)]	Data
STC-1	Bare Type S wires in alumina insulator.	Within slug on aluminum oxide pedestal.	Yes (see Figure 3.1-5)
STC-2	Platinum sheathed MgO insulated types.	In capping assembly.	Yes (see Figure 3.1-6)
STC-3	Bare Type S wires sheathed in SiO_2.	On crucible wall[(b)] 2 in. above original cavity bottom.	No
STC-4	Bare Type S wires sheathed in SiO_2.	On crucible wall 1/4 in. above original cavity bottom.	Yes (see Figure 3.1-7)
KTC-1	0.040 in. OD stainless steel sheathed MgO insulated Type K.	On crucible wall 4 in. above original cavity bottom.	No
KTC-2	Same as KTC-1.	3/4 in. from original cavity wall 4 in. above original cavity bottom.	No
KTC-3	Same as KTC-1	On crucible wall 1 in. above the original cavity bottom.	Yes (see Figure 3.1-8)
KTC-4	Same as KTC-1	1 in. below original cavity bottom; junction at centerline of crucible.	Yes (see Figure 3.1-9)
KTC-5	Same as KTC-1	1/2 in. below original cavity bottom; junction at centerline of crucible.	No
KTC-6	Same as KTC-1	1-1/2 in. below original cavity bottom; junction at centerline of crucible.	No
KTC-7	Same as KTC-1	2 in. below original cavity bottom; junction at centerline of crucible.	No

(a) See thermocouples oriented horizontally, except KTC-1 which was vertically oriented.

(b) Wall thermocouples mounted as described in Reference 3-1.

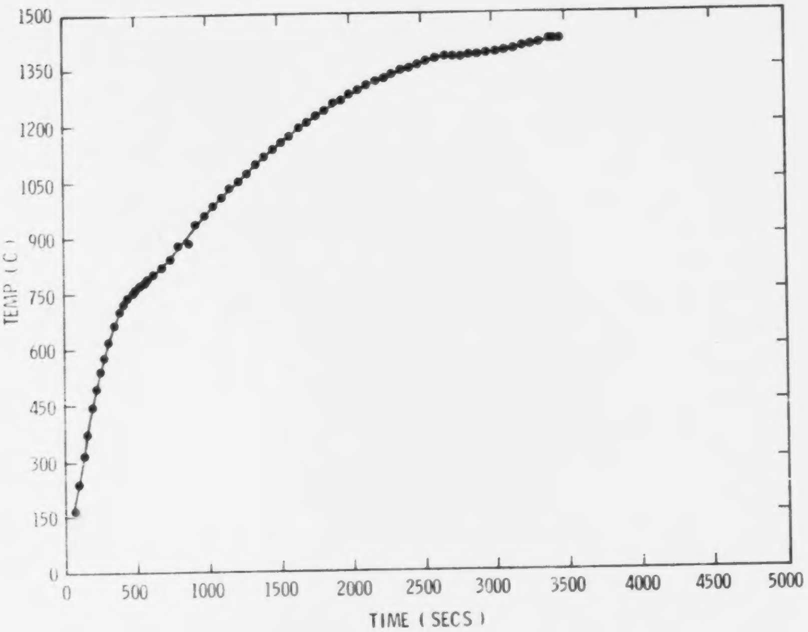

Figure 3.1-5. Test BURN 3 - Steel Temperature (°C)

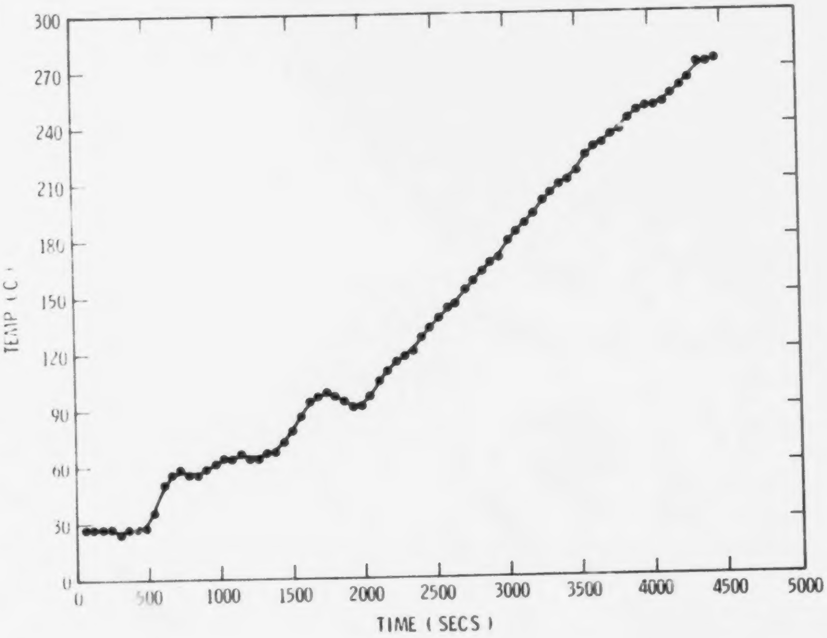

Figure 3.1-6. Test BURN 3 - Cap Thermocouple

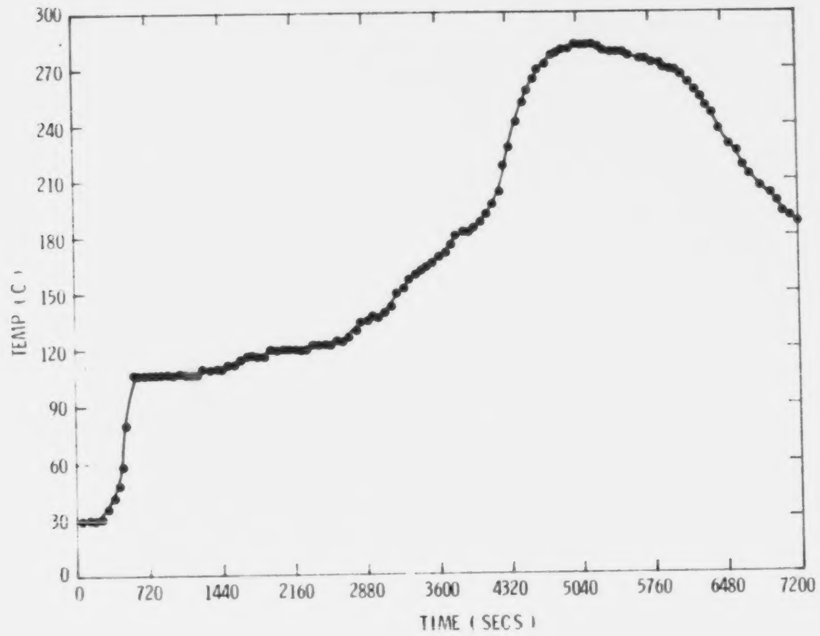

Figure 3.1-7. Test BURN 3 - Wall Thermocouple 0.25 In. Above Cavity Bottom

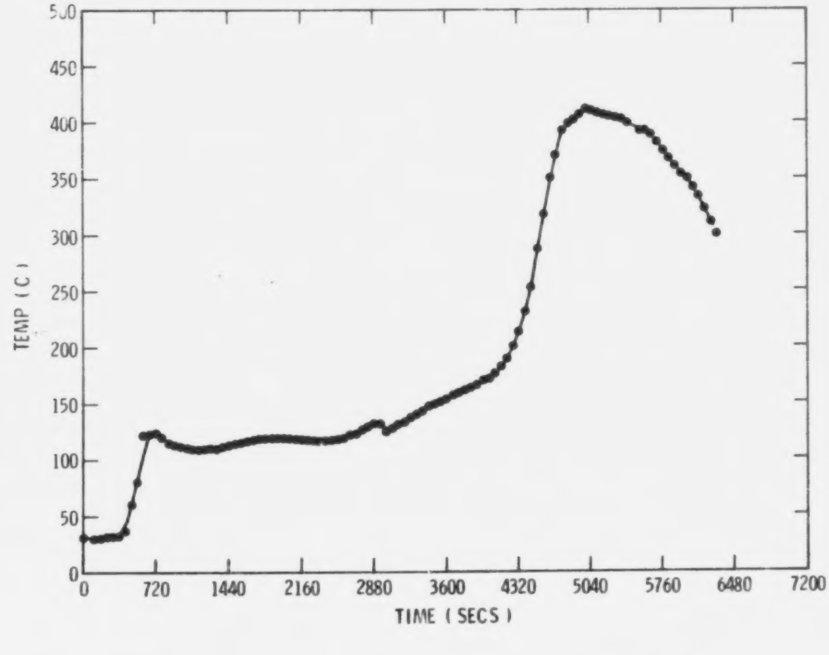

Figure 3.1-8. Test BURN 3 - Thermocouple 1 In. Above Cavity Bottom

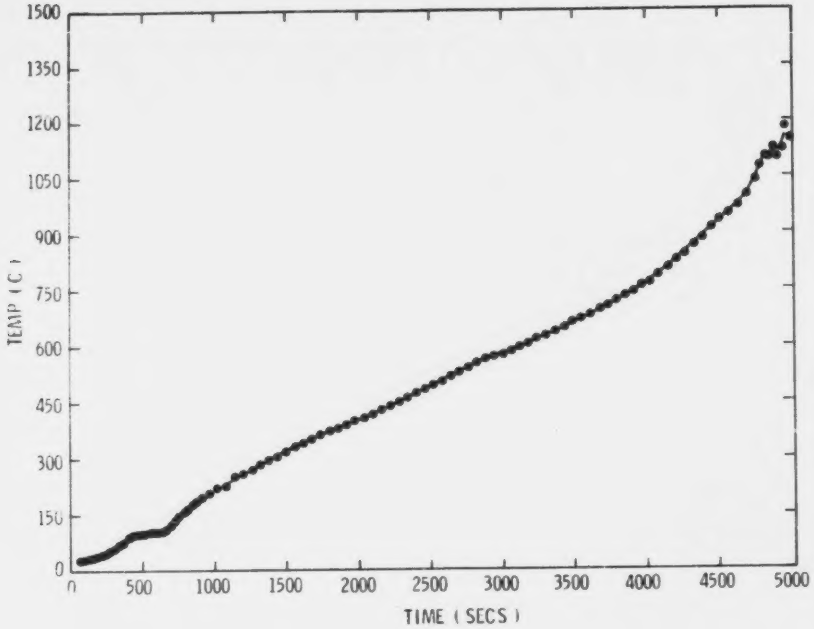

Figure 3.1-9. Test BURN 3 - Thermocouple 1 In. Below Cavity Bottom

The steel slug was heated at a rate of ~ 2°C/s from 303 K (30°C) to 973 K (700°C). This corresponds to a power input of about 7.1 kW, if the system is assumed to be adiabatic. Once the Curie temperature of the steel was exceeded, the quality of inductive coupling became degraded and the steel could be heated only at a rate of 0.35°C/s. This indicates a minimum power input of about 1.1 kW.

At about 1673 K (1400°C), the heating of the steel slowed even further as both steel and concrete began to melt. The onset of melting erosion of concrete was taken to be 2500 s after the start of the test.

Posttest inspection of the crucible contents showed that the steel had completely melted. This melting of the steel was expected since the liquidus temperature of the CRBR concrete has been estimated to be about 1873 K (1600°C).[3-6] Some of the steel formed a rough disk 5.8 to 5.4 in. in diameter and weighing 2615 g. This disk was found at the bottom of the crucible cavity. A second steel piece of very distorted shape was found near the top of the crucible within solidified slag. This second piece weighed 725 g. Photographs of the steel pieces are shown in Figures 3.1-10 and 3.1-11.

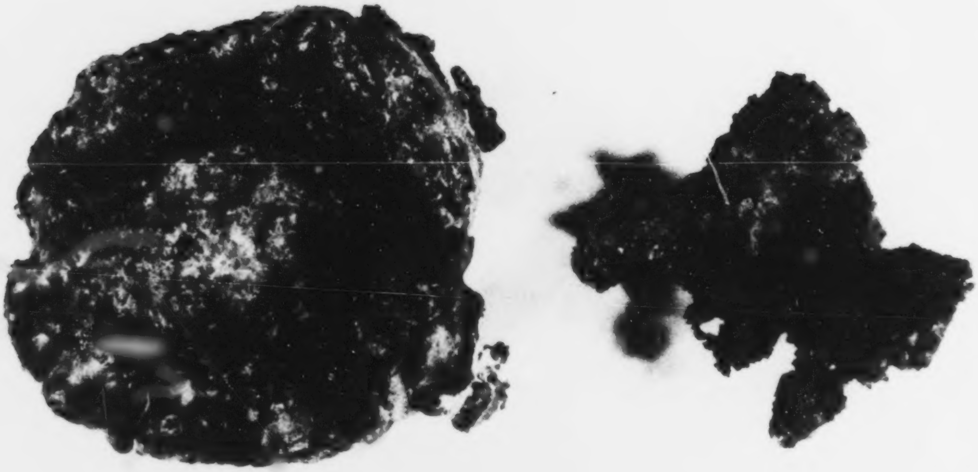

Figure 3.1-10. Top View of Steel From Test BURN 3

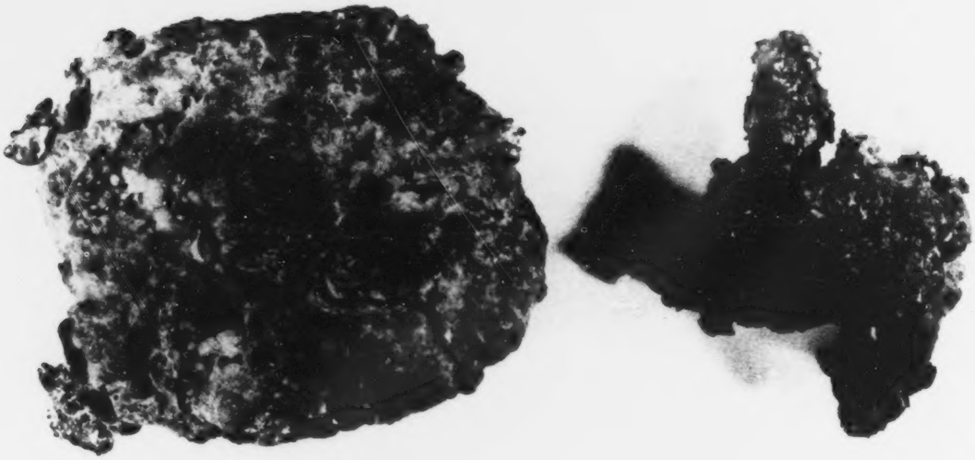

Figure 3.1-11. Bottom View of Steel From Test BURN 3

The balance of the steel (about 1.7 kg) used in Test BURN 3 was not located. It was either distributed within the slag as fine particulate or had oxidized.

The posttest configuration of the steel was not suitable for intense inductive heating. The largest mass of steel was only about 1 in. thick and was very near the bottom of the induction coil, well out of the uniform electro-magnetic field of the coil. The very small mass of the steel was also an impediment to effective inductive heating.

The very low temperature measured by the thermocouple in the capping assembly indicated that this sensor was not well situated for measuring upward heat flux from the melt. Temperatures were fairly constant at about 301 K (28°C) up to 480 s after the start of the test. The temperature then rose sharply to about 333 K (60°C). Temperatures rose slowly, but not monotonically to about 373 K (100°C) over the period 490 to 2000 s after the start of the test. After 2000 s, this thermocouple indicated a fairly linear temperature rise of about 0.1°C/s to a maximum temperature of about 543 K (270°C).

The temperature data show that the thermocouple could not have been directly exposed to the very hot melt in the crucible. It must have been sensing the temperatures of gases evolved during the test. Water liberated as steam from the concrete and condensing on the top hat would account for the low temperatures recorded for the first 2000 s of the test.

The thermocouple 1 in. below the original bottom of the crucible cavity rose in temperature to an arrest at 375 K (102°C) that occurred about 420 s after the start of the test. This arrest lasted for about 250 s. The temperature rose smoothly after the arrest until the thermocouple failed at 1473 K (1200°C) about 4950 s after the test began. This failure indicates an erosion rate of 3.7 cm/hr which is somewhat greater than the rate of 3.2 cm/hr observed for attack on ordinary limestone concrete Test BURN 2. This difference may be attributed to the higher temperature, molten steel developed in Test BURN 3.

Thermocouple outputs from sensors located on the walls of the crucible were quite different from the output of the thermocouple below the crucible cavity.

Temperatures at the locations of these wall sensors rose rapidly to an arrest at about 375 to 393 K (102° to 120°C), 450 s after the start of the test. Temperatures rose no more than 20°C for the next 2000 s. Then temperatures increased at a rate of 2.5°C/min up to about 443 K (170°C). At this point, the temperatures rose quite sharply. Neither of the wall thermocouples failed so that a radial erosion rate could not be calculated from the temperature sensors.

The observed behavior of the wall thermocouples may be rationalized in terms of gas cooling. The concrete walls of the crucible cavity were not in contact with the steel while it was solid. Steam and gases liberated from the concrete passed through the gap between the steel and the concrete and kept the walls cool. No such cooling mechanism was available at the bottom of the crucible cavity which was in intimate contact with the steel. Once concrete began to melt, liquid-phase heat transfer from the steel to the concrete accelerated temperature rises in the wall concrete. The liquid phase reduced the cooling effect of gases passing upward along the wall. Collapse of the steel prevented any very large temperature rise in the "1/4-in. wall thermocouple."

Posttest inspection of the test fixture showed a frozen slag layer between the steel and concrete at the bottom of the cavity. This frozen layer was 0.25 to 0.4 cm thick. Frozen slag layers on the walls of the crucible cavity were 0.4 to 1.6 cm thick. Heat-affected (but not melted) concrete on the walls was 0.2 to 0.5 cm thick. Radial erosion rates calculated from these posttest measurements were 4.1 to 4.6 cm/hr. These erosion rates are greater than the observed axial erosion rate of 3.7 cm/hr. This result differs from the results of Test BURN 2 in which the radial erosion rate was only 70% of the axial erosion rate.

The fact that the melt migrated so easily in the radial direction is strong evidence that neither Lorenz forces produced by the coil, nor the water-cooling of the coil had strong influence on the nature of the melt concrete interaction.

Results of Test BURN 3 are indeed curious and bear repetition. Some modifications that have been arranged for the repeat tests include:

- Low pass filters for thermocouples to eliminate induction noise

- Reorientation of induction coil so that axial erosion of concrete does not move the steel out of the effective heating zone of the coil
- Improved melt temperature measurements
- Capping system that allows gas generation rates to be monitored.

3.1.4.3 Test BURN 4 -- The experimental and instrumental arrangements used in Test BURN 4 were quite similar to those used in Test BURN 3. However, the melt to be sustained in Test BURN 4 was generated metallothermically in a generator similar to that used in the PLATE test series. A melt-out plug in the generator allowed the melt to flow into the awaiting concrete crucible. Once in place, the melt was to be sustained by induction coils wrapped around the crucible.

The metallothermic generator was used in lieu of igniting the metallothermic reaction within the concrete crucible so that the crucible could be filled with melt. Powder densities of the reaction constituents are too low to generate sufficient melt in-situ.

Unfortunately, gas generation initiated by the melt when it entered the crucible was so great that nearly all the melt was expelled from the crucible. The melt destroyed most of the instrumentation sensors used in the test. Insufficient melt remained for sustained interaction by induction heating. Consequently, the test was terminated. Figure 3.1-12 shows a posttest x-ray of the crucible.

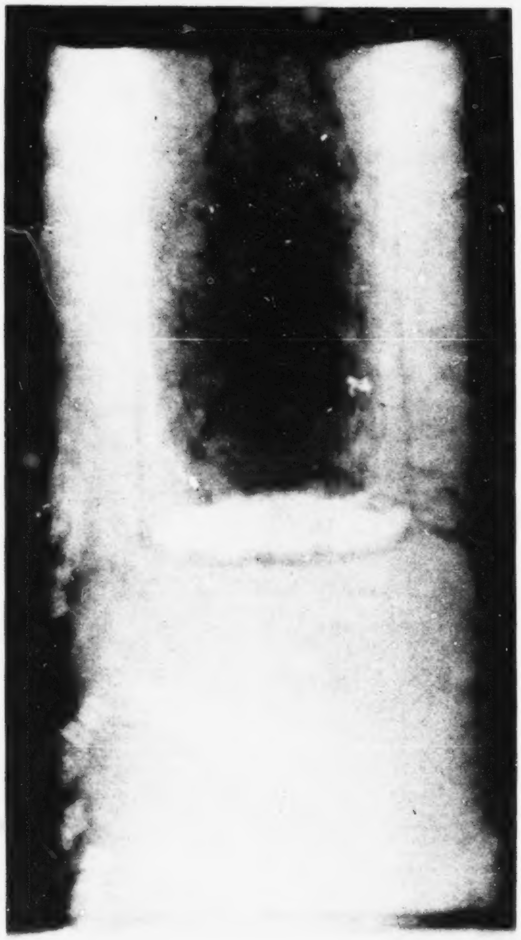

Figure 3.1-12. Posttest X-Ray of the Test BURN 4 Crucible

3.1.5 Status of the CATH Test Series

The BURN series tests deal exclusively with core debris/concrete interactions. A parallel series of tests, the CATH series, deals with core debris interactions with materials other than concrete. These alternate materials have become interesting as possible means of avoiding the gas generation and erosion phenomena associated with melt/concrete interaction. As with the BURN series, the CATH test series is devoted to the development of techniques for quantitative exploration of phenomena.

The first two CATH tests were transient interactions between thermitically generated melts and commercial magnesium oxide bricks. Results of these tests were reported previously. Future tests in the series are summarized in Table 3-VI. These future tests all involve sustained melt interactions.

Table 3-VI

Summary of Planned CATH Tests

Test	Crucible	Objective
CATH 3	MgO orifice of crucible cavity filled by an MgO brick also exposed to the molten mixture.	Observe "slag line" attack on MgO at temperature above 1700°C.
CATH 4	MgO perforated at the bottom so that MgO bricks are exposed to the melt. Bricks oriented so that a crack between the bricks is exposed to the melt.	Similar to Test CATH 3. Also flow of melt through cracks, etc will be observed.
CATH 5	Borax	Sustained interaction of inductively heated mixture of stainless steel powder and UO_2 with borax.
CATH 6	MgO	Sustained interaction of a mixture of UO_2 and stainless steel particular with MgO. Actual crucible design based on results of Tests CATH 3 and 4. Test to be correlated with in-pile experimental results when they are available.
CATH 7	High alumina cement	Similar to Test CATH 6.

Test CATH 3 will involve sustained interactions between molten stainless steel and magnesium oxide. The main interest in this test lies in the dissolution of MgO by molten products of the oxidation of steel, the so-called slag-line attack. This type of attack may be more important than thermal attack on the degradation of MgO. Test CATH 3 will use inductively heated stainless steel melts contained within MgO crucibles. If this technique proves useful, Test CATH 3 may spawn a much larger series of tests for exploring the kinetics of slag-line attack.

Test CATH 4 will be similar to Test CATH 3 except the MgO crucible will be perforated so that melt will contact MgO bricks. Flow of the melt into cracks between the bricks will be an issue of interest in this test.

Test CATH 5 will explore sustained interactions between inductively heated stainless steel granules and borax. Uranium oxide will also be present in the cavity so that dissolution of the uranium oxide in borax may be evaluated.

Test CATH 6 will be an attempt to duplicate, as completely as possible, tests to be run in-pile as part of an allied research program at Sandia. Comparison between the in-pile and out-of-pile results will allow an evaluation of the extent of realism to be associated with the nonprototypic heating techniques used in the out-of-pile experimentation. Precise details of the test await final designs for the in-pile experiments. The test will involve UO_2 and stainless steel interactions with MgO oxide. The atmosphere present during the interaction will very likely be helium. Heating rates in the core material will be imitative of those observed during the in-pile experiment.

The final test, CATH 7, will involve sustained interaction between core materials and high alumina cement. This test will be quite similar to tests in the BURN series. Much higher temperatures will be encountered due to the refractory nature of the high alumina cement.

3.2 PAHR Debris Bed (J. B. Rivard, 4422)

3.2.1 Introduction

The objective of the experimental studies of debris beds is to provide information on the behavior of fragmented reactor materials following a core-disruptive accident in a fast reactor. Because fuel debris will continue to generate power due to the decay of contained fission products, high temperatures and resultant melting could threaten containment if the generated heat is not removed. Initially, it is desirable to ascertain the cooling capability which debris beds may possess due simply to natural processes--i.e., cooling which is not aided by forced circulation or other imposed measures.

During the report period, further analysis of the results of the initial D-series experiments[3-7, 3-8, 3-9] has been performed. Some of this analysis is reviewed below. Added detail is contained in the topical reports.[3-8, 3-9]

3.2.2 Analysis of Bed Dryout

The general behavior observed in debris bed experiments D-2 and -3 has indicated that the power being generated within the dryout zone is unidirectionally transferred out of the zone by a process which may be approximated by a one-dimensional conduction-type process. (Radiation-heat transfer may augment the process, but is not directly considered here). In the following analysis a one-dimensional slab is assumed for ease in computation.

If the dryout zone is assumed to be established quickly with a constant vertical thickness, a plausible explanation of the temperatures observed during dryout would be given by the temperature response at a fixed location (z) within a medium of thickness (Z) which is suddenly subjected to internal power generation at a constant rate (q) (per unit volume), while one boundary (z = Z) of the medium is maintained at a fixed temperature corresponding to the sodium saturation temperature. The other boundary (z = 0) of the medium is considered adiabatic. A simple conduction model of this process (Figure 3.2-1) is

$$\frac{\partial \theta}{\partial t} = \alpha \frac{\partial^2 \theta}{\partial z^2} + \frac{q}{\rho c}$$

for the temperature elevation $\theta(z, t)$ above the sodium saturation temperature. The initial condition

$$\theta(z, 0) = 0$$

and boundary conditions

$$\frac{\partial \theta(0, t)}{\partial z} = 0, \quad \theta(Z, t) = 0$$

complete the specification of the problem for adiabatic and isothermal boundaries.

The solution for this problem is given by[3-10]

$$\frac{\theta(z, t)}{qZ^2/k} = \frac{1}{2}\left[1 - \left(\frac{z}{Z}\right)^2\right] - 2\sum_{n=0}^{\infty} \frac{(-1)^n}{(\lambda_n Z)^3} e^{-\alpha \lambda_n^2 t} \cos \lambda_n z \qquad (3.1)$$

where the eigenvalues are:

$$\lambda_n Z = (2n + 1)\pi/2, \quad n = 0, 1, 2, 3 \ldots$$

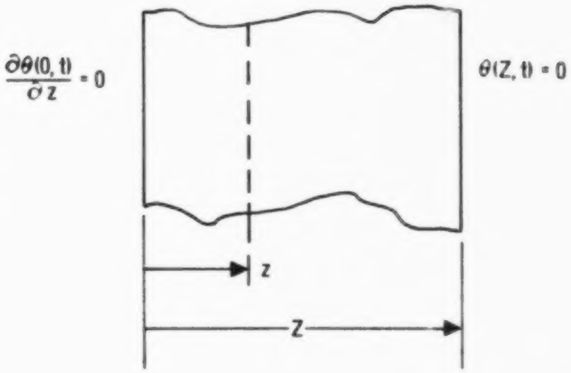

Figure 3.2-1. Conduction Model of Dryout Zone, Initial Hypothesis. (Bottom of the bed is at left.)

Figure 3.2-2 shows temperature elevations at a particular value of z vs time given by Eq (3.1) for three values of Z, namely 5, 10, and 15 mm.

Figure 3.2-2.

Calculated Temperature Elevations (Eq 3.1) vs Time at 1.5 mm Above the Bottom of the Bed for Three Thicknesses of Dryout Zone, Compared With Observed Temperature Transient During Dryout of the D-3 Experiments (circles).

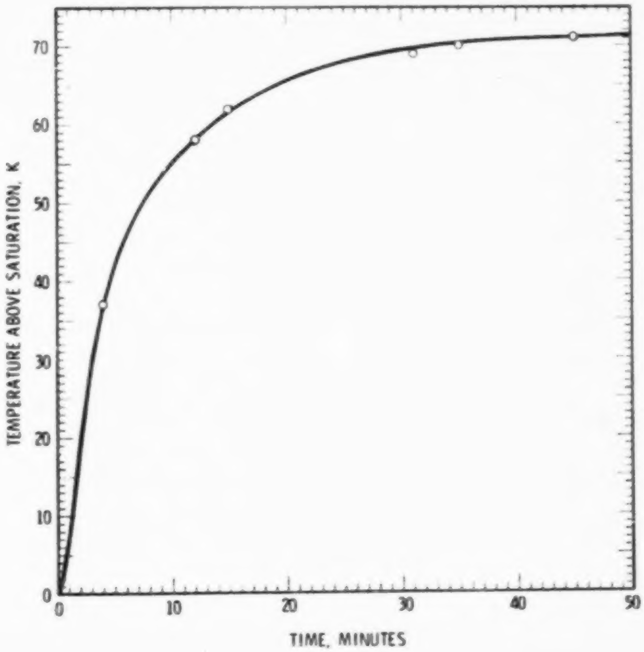

An alternate theory which requires only minor alteration of the original hypothesis is obtained if the thickness of the dryout zone is assumed to be established more slowly. This is conceptually equivalent to considering the thickness (Z) in the original mathematical formulation, Eq (3.1), a variable function of time (t) (Figure 3.2-3). Recalling that, for a general function F(X, t), where X is a function of t,

$$\frac{dF}{dt} = \frac{\partial F}{\partial X}\frac{dX}{dt} + \frac{\partial F}{\partial t} ;$$

the formulation (symbolically) for the temperature response (θ_2) at a fixed location in a medium of variable thickness, $Z(t)$ becomes

$$\theta_2(Z,t) = \int_0^t \left[\frac{\partial\theta}{\partial Z}\frac{dZ}{dt'} + \frac{\partial\theta}{\partial t'}\right] dt' \quad . \tag{3.2}$$

Applied to the solution of the original problem, this formulation yields

$$\frac{\theta_2(Z,t)}{q/K} = \int_0^t Z\left\{\frac{dZ}{dt'} - 2\sum_{n=0}^{\infty}\frac{(-1)^n}{(\lambda_n Z)^3}\, e^{-\alpha\lambda_n^2 t'} \left[\left[2\frac{dZ}{dt'} + \alpha\lambda_n^2\left(2t'\frac{dZ}{dt'} - Z\right)\right]\cos\lambda_n z + \frac{dZ}{dt'}\sin\lambda_n z\right]\right\} dt' \tag{3.3}$$

where Z and its derivative are understood to be functions of time.

A necessary test of the hypothesis consists of finding Z such that Eq (3.3) gives values which match the observed dryout responses. Since Eq (3.3) is not in general analytically integrable, a numerical integration technique was employed. Also, in order to allow precision in the taking of the derivative, an analytical formulation of Z was used. Because of the shape of the observed temperature response curves and to allow sufficient freedom in the matching effort, the function chosen for Z was

$$Z = A(1 - e^{-\beta t}) + B(1 - e^{-\gamma t}) \quad . \tag{3.4}$$

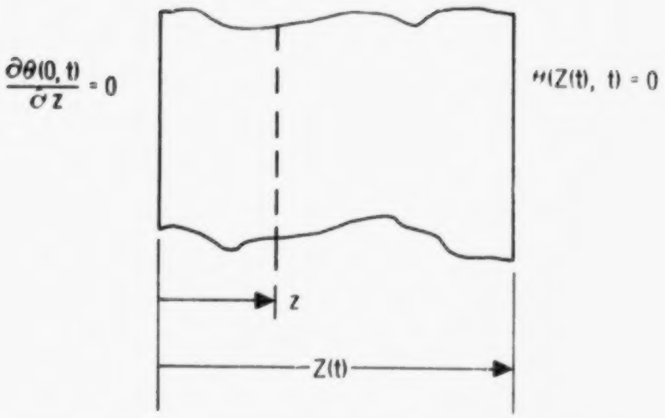
$\frac{\partial\theta(0,t)}{\partial z} = 0$
$\theta(Z(t), t) = 0$
z
Z(t)

Figure 3.2-3. Conduction Model of Dryout Zone, Second Hypothesis

Figure 3.2-4 shows the solution to Eq (3.3), using chosen values in Eq (3.4), as compared with data points from Dryout 4 of the D-3 experiment. The corresponding Z for this and three additional dryout transients are given in Figure 3.2-5.

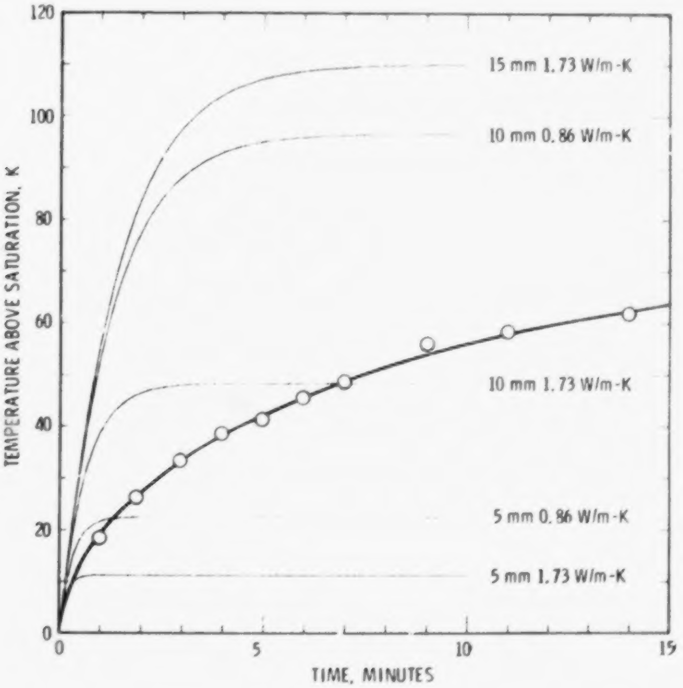

Figure 3.2-4. Calculation (solid line), Using Eqs (3.3) and (3.4), Compared With Data Points From Dryout 4, D-3 Experiment

The curves given in Figure 3.2-5 are not unique in the mathematical sense. At this time, the boundary movement, as embodied in the function Z, cannot be shown to be entirely responsible for the observed temperature behavior. In particular, the above analysis has not considered variation of the effective thermal condutivity of the zone. Nevertheless, this explanation for the behavior is plausible, and is appealing because of the obvious necessity for the dryout zone to achieve some thickness over time to provide even a rudimentary explanation of the observations, and because of the failure of the simpler initial hypothesis to adequately explain those observations.

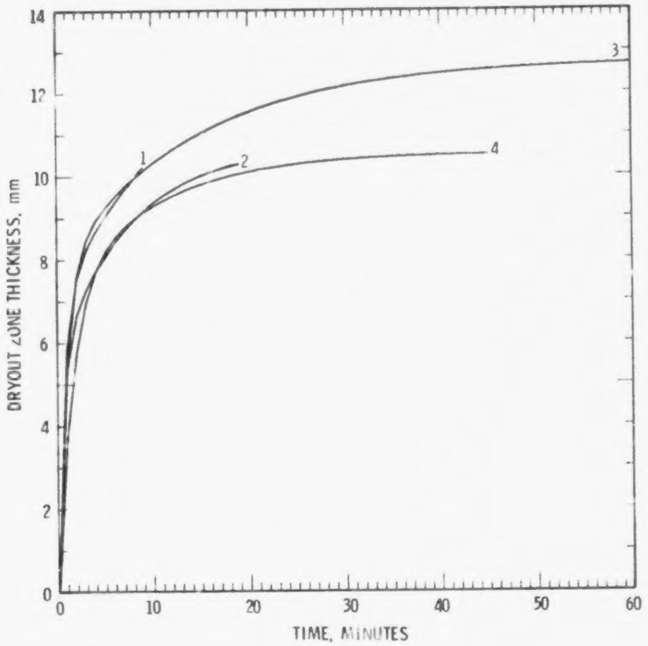

Figure 3.2-5. Values of Variable Dryout Zone Thickness (Z) Calculated for Dryouts 1 Through 4 for the D-3 Experiment

An additional consideration generated by this model of dryout behavior is the deviation from the equilibrium temperature distribution within the dryout zone. A measure $\xi(Z,t)$ of the nonequilibrium is given by

$$\begin{aligned} \xi(Z,t) = \frac{1}{2}\left[1 - \left(\frac{z}{Z}\right)^2\right] - \int_0^t Z \Bigg\{ \frac{dZ}{dt'} - 2\sum_{n=0}^{\infty} \frac{(-1)^n}{(\lambda_n Z)^3}\, e^{-\alpha\lambda_n^2 t'} \\ \Bigg[\left[2\frac{dZ}{dt'} + \alpha\lambda_n^2\left(2t'\frac{dZ}{dt'} - Z\right)\right] \cos \lambda_n z \\ + \lambda_n z \frac{dZ}{dt'} \sin \lambda_n z \Bigg]\Bigg\} \, dt' \end{aligned} \qquad (3.5)$$

where Z and its derivative are understood to be functions of time (t). Evaluation (with the previously used assumptions) shows ξ to be negligibly small for the four expansions given in Figure 3.2-5. This tends to support the contention that zone expansion is not driven by thermal imbalance within the zone; rather, the zone is thermally stable for the conditions of the calculation and the heat generated within the zone is transferred in a quasi-steady manner to the upper boundary of the zone.

This effect is examined further in Figure 3.2-6, which was generated by using the derived expansion for dryout transient 4. The upper curve represents the power generated in the dryout region. The two lower curves represent the power which is absorbed in performing the work of displacing the liquid sodium column upward (lowest curve) and in vaporizing the sodium supplied to the expanding zone (intermediate curve). The small amplitude of the abosorbed power (both in the absolute and in the relative sense), combined with the fact that the region is thermally in quasi-equilibrium, means that dryout does not significantly alter the power transferred--only the mode of its transfer.

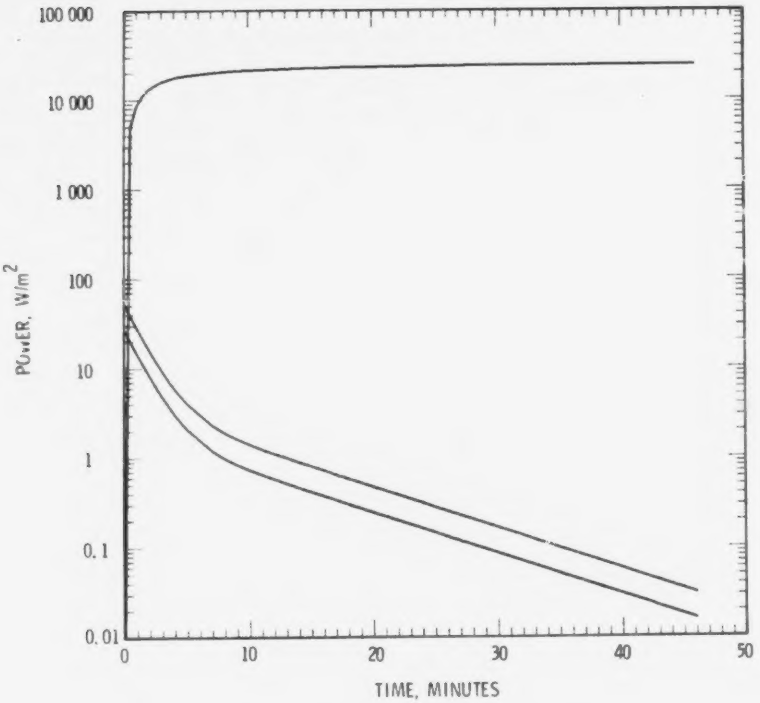

Figure 3.2-6. Power Partitioning During Dryout as Calculated for Dryout Expansion 4. (The upper curve is the power generated in the dryout zone; the intermediate curve is the power used in performing the work of displacing the liquid sodium column upward.)

3.2.3 Summary

A one-dimensional synthesis of the thermal behavior during dryout shows that the observed temperature transients are due to increasing thickness of the dryout zone rather than to thermal equilibration of a rapidly-formed zone. In addition, the analysis shows that the zone is in approximate thermal equilibrium during its expansion. Vapor generation and the work of displacing the sodium upward absorb little energy during the dryout process; thus, dryout does not significantly alter the power transferred--only the mode of its transfer. The main result of dryout is the shortening of the convection flow paths in the region above the dryout zone, leading to a more stable hydrodynamic regime.

3.3 PAHR Molten Pool (H. G. Plein,[*] 4422; R. J. Lipinski, 4425; Tom Kerley, 4422)

3.3.1 Introduction

The in-core molten fuel pool experiment program is investigating the heat flux distribution and containment ablation potential of molten LMFBR debris materials under typical temperature and heating conditions. In addition, the portion of this task devoted to the development of high-temperature thermometry has led to a study of the application of ultrasonic thermometry not only to molten fuel pools, but to debris bed and extended-dryout experiments.

The major activities this quarter included the evaluation of refractory metals to be used as high-temperature ultrasonic thermometers in debris bed and extended-dryout in-core experiments, the high-temperature material interaction studies of mixed UO_2--stainless steel particulates and of particulate UO_2 on solid MgO (Harklase) brick, the preparation for upcoming in-core experiments, and the continued modeling of molten pool formation and growth.

Other activities this quarter include the preparations for the next in-core experiment, the initial studies on the use of a continuously rotating ultrasonic thermometer sensor, the first tests of an ultrasonic thermometer to be used as a sodium level gage, the continued high-temperature experiments on interaction of particulate UO_2 and solid MgO (Harklase), and detailed analysis of the thermal conductivity of porous fuel beds.

3.3.2 High-Temperature Materials Interaction Studies

Experiments continued with the object of defining the high-temperature behavior of UO_2 particles in contact with Harklase (98% MgO) brick. The MgO is a candidate sacrificial material for use in containment of core debris.

Furnace tests were conducted in a helium atmosphere with depleted UO_2 particles on a solid disk of Harklase. Maximum temperatures reached in the recent series of tests were 2773 K (2500°C), 2830 K (2557°C), and 2877 K (2604°C).

---

[*] Deceased

Significant diffusion of the UO_2 into the MgO occurred at 2773 K and 2830 K; however, the fuel easily separated from the MgO following the experiments. The 2877 K experiment resulted in a fusion of the UO_2 and MgO void spaces were left in the mixture following the experiment. These recent tests when combined with earlier data result in a temperature for the fusion of particulate UO_2 and MgO in an inert atmosphere of 2848 K (2575°C) ±40 K. This fusion temperature is significantly higher than would be expected from earlier studies[3-11] of UO_2 and MgO where the eutectic occurred at approximately 2553 K (2280°C). This higher fusion temperature indicates that MgO should contain UO_2 in an accident situation. However, other considerations must be evaluated including the presence of steel in the fuel pool, the atmosphere expected during the interaction, and the problem of hot molten fuel impacting directly on the MgO.

The experiments conducted on UO_2 and MgO consisted of a slow heating to maximum temperature and not a sudden impact of hot fuel onto the MgO as might be possible in a LMFBR accident. The thermal shock of molten UO_2 falling onto MgO was examined in the work by Swanson, et al.[3-12] In this work, very large temperature gradients, 2273 K (2000°C)/cm, made determination of the interaction temperature difficult.

3.3.3 Report Preparation

Two reports are in preparation describing work completed in this project. The first, entitled "Refractory Metals for Ultrasonic Thermometry Applications," describes an experimental study conducted to develop an ultrasonic thermometer sensor for use in the debris bed and extended dryout experiments. This study also provided the necessary information to choose a material for use as the ultrasonic thermometer sensor in the sodium level gage described in Section 3.3.5 below.

A second report, entitled "An Ultrasonic Thermometry System for Measuring Very High Temperatures in Reactor Safety Experiments," describes the technology developed for the in-core molten pool experiments and the application of the ultrasonic thermometers in experiments MP-1, -2, and -3.

3.3.4 Ultrasonic Thermometer Development

The most significant problem encountered with the use of ultrasonic thermometers is the sticking of the sensor to the sheath used to protect the metal sensor. Since this sticking is especially bad with metal sheaths at high temperatures, ThO_2 sheaths were used in the molten pool in-core experiments. However, even the ceramic sheaths will stick to metal sensors at very high temperatures.

A possible solution to the sticking problem involves continuously rotating the sensor within the sheath. A rotation rate of about 2 rps appears to be sufficient to prevent most sticking.

Several preliminary experiments were conducted with a thoriated tungsten sensor in a molybdenum sheath. Essentially no sticking was seen in furnace experiments to 2473 K (2200°C) for the rotating sensor. Serious sticking occurred for a stationary sensor at various temperatures below 2473 K.

Experiments will continue with rotating ultrasonic thermometer sensors in tungsten sheaths to temperatures up to the furnace limit of approximately 3173 K (2900°C). Further tests will use a rotating sensor with sheath in depleted, particulate UO_2 to the UO_2 melting temperature of 3123 K (2850°C). Eventually, this improved technology will be incorporated into the molten pool and possibly the debris bed in-core experiments.

3.3.5 Ultrasonic Sodium Level Gage

A diagnostic is needed which indicates the volume of the dried-out region in a porous debris bed. During dryout, the liquid sodium is displaced by sodium vapor within a portion of the bed volume. The sodium level is now higher in the closed vessel above the fueled region. The sodium level change is proportional to the volume of the bed which has dried out. Thus a measurement of the change in sodium level is a diagnostic of the volume of the fuel bed which is vapor-filled.

An ultrasonic thermometer is being studied which will locate the bulk sodium liquid/vapor interface. Since the sodium is heated, the bulk sodium liquid/vapor interface may have a significant gradient across that interface. As the bulk liquid sodium level rises during dryout, the ultrasonic sensor will see an increasing average temperature over the length of a sensor element.

Several initial experiments were conducted with a Type 302 stainless steel ultrasonic sensor. The stainless steel has a better temperature sensitivity than do most other metals. The shape and amplitude of the ultrasonic signals are not affected by immersion of the sensor in water. However, a slight attenuation of the signals occurs when the sensor is immersed in room temperature mercury. These two liquids provide an easy way to test the expected response of the sensor to a moving liquid level.

An experiment is planned to study the response of the stainless steel ultrasonic thermometer sensor in a sodium pool with a changing level. This test will use both a bare sensor rod and a sensor rod within a steel sheath. One of the questions to be examined in this test is the survivability of the sensors while the sodium freezes and thaws.

3.3.6 Thermal Conductivity of a Powdered Bed

The conductivity of a dry bed of fragmented UO_2 must be known to accurately model the molten-pool experiments. A review of the literature was made, and the most appropriate formula for conduction in a mixture of powdered oxide and gas was found to be that of Godbee and Ziegler.[3-13] Their model included effects from the gas and solid conductivities, void fraction, average particle size, particle size distribution, and rarified-gas effects in small spaces. Predicted conductivities generally agreed with their experimental results within ±5%. However, their experiment did not offer a severe test for heat transfer by radiation. Since thermal radiation could be dominant near the fuel melting point, a separate review for radiation in a powder was made. Vortmeyer makes the most recent review of past work.[3-14] Most authors agree that radiative heat transfer can be accommodated by an effective conductivity which is proportional to the cube of temperature times some function of emissivity, void fraction, and transparency of a single layer of particles. The most accurate model which includes all these effects is that of Kasparek[3-15] in which the radiative conductivity is

$$k_r = \left(\frac{\epsilon + \tau}{1 - \tau}\right) 4\sigma\, DT^3$$

where ϵ is the emissivity, τ is the layer transparency, σ is the Stefan-Boltzmann constant, D is the particle diameter, and T is the temperature. The transparency is a function of the void fraction. Kasparek considers only opaque particles. However, partially transparent particles may be accommodated by adjusting the particle layer transparency as follows. For a single sphere with radius R and a radiation extinction coefficient of the material β, the transmission through the sphere is

$$\tau = \frac{1}{\pi R^2} \int_o^R e^{-2\beta\sqrt{R^2-r^2}} \, 2\pi r \, dr \quad .$$

With the variable change $Z = \sqrt{R^2 - r^2}$, this becomes

$$\tau_s = 2(1 - (1 + 2\beta R) e^{-2\beta R})/(2\beta R)^2 \quad .$$

For a layer of spheres, some radiation passes between the spheres; this is the transparency for opaque spheres, τ_o. Thus, the total transparency is

$$\tau = (1 - \tau_o)\tau_s + \tau_o \quad .$$

For rhombic packing, $\tau_o = 1 - \pi/\sqrt{12}$ and the void fraction $\alpha = 1 - \pi\sqrt{18}$; for cubic packing, $\tau_o = 1 - \pi/4$ and $\alpha = 1 - \pi/6$. Extrapolation between those points yields the approximation

$$\tau_o \doteq \alpha/2 \; .$$

The debris used in experiments MP-1 and -2 was characterized as follows: The material was 92.3% dense $UO_{2.00}$ fragmented to an overall density of 5700 W/ kg/m^3. The particle size distribution was linear from 108 to 1750 μm on a semilog plot of diameter vs mass fraction less than the size. The median particle diameter was 435 μm and the void fraction between particles was 44%. With these characteristics and with the temperature dependent material properties from References 3-16 and 3-17, the following expressions were obtained as fits to the formulae for heat transfer by conduction alone in UO_2-helium, UO_2-argon, and UO_2-sodium vapor:

$$k(UO_2 - He) = 0.891 + 2.001 \times 10^{-3} T - 2.064 \times 10^{-6} T^2 + 7.710 \times 10^{-10} T^3 - 8.912 \times 10^{14} T^4$$

$$k(UO_2 - A) = 0.491 + 1.581 \times 10^{-4}\,T - 4.580 \times 10^{-8}\,T^2 - 7.512 \times 10^{-3}\,T^3$$

$$+ 3.941 \times 10^{-15}\,T^4$$

$$k(UO_2 - Na) = 1.501 - 1.461 \times 10^{-3}\,T + 5.462 \times 10^{-7}\,T^2 - 4.1841 \times 10^{-11}\,T^3$$

$$- 5.355 \times 10^{-15}\,T^4 ,$$

where k is in W/m · K and T is in K.

The radiation extinction coefficient is estimated in Reference 3-18 to be about 5000 m^{-1}. Recent measurements of molten UO_2[3-19] indicate a total conductivity of 10.2 W/m · K. The measurement was performed between two close parallel plates, for which

$$q = \left(\frac{4n^2 \sigma T^3}{2/\epsilon - 1 + 3 \quad \beta d/4} + \frac{k_c}{d} \right) \Delta T = \frac{k_{total}}{d} \Delta T \quad ,$$

where n is the index of refraction, σ is the Stefan-Boltzmann constant, ϵ is the emissivity of the plates, d is the plate separation, and k_c is the modular conductivity. Using $n = 2.3$, $T = 3250$ K, $\epsilon = 0.9$(UO_2 Crust), $k_c = 3.5$ W/m · K, and $d = 0.00081$ m, yields $\beta = 6200\ m^{-1} = 1/(0.16\ mm)$. This agrees with Reference 3-20. Using $\beta = 6200\ m^{-1}$ yields a total layer transmission for the MP-1 and -2 debris of

$$\tau = (1 - 0.22)\,(0.2157) + 0.22 = 0.39 \quad .$$

Thus, the radiative conductivity is expected to be

$$k_r = 2.12 \times 10^{-10}\,T^3 (W/m \cdot K) \ .$$

For the UO_2-He mixture used in MP-1 and -2, the radiative conductivity equals the mixture molecular conductivity at 2000 K. Thus, the radiation effect should be observable, and the experimental results should serve as a good test of the theory. In particular, the influence of a wide distribution in particle size will be of interest.

3.3.7 Activity for Next Quarter

Preparations for the next in-core molten pool experiment, MP-4, will be completed to accommodate an experiment date of January 1979. MP-4 will be an experiment with particulate UO_2 on a solid MgO disk to determine melting interaction to be expected for intrinsically heated fuel. The report on refractory metals for use as ultrasonic thermometers will be published. Work will continue on the continuously rotating ultrasonic thermometer sensor. The ultrasonic sodium level gage will be studied for inclusion in the next debris bed in-core experiment, D-4. Final design of the ultrasonic thermometers for the measurement of fuel temperature gradients in D-4 will be completed. Comparison of the porous fuel bed thermal conductivity model will be made with the measured fuel temperatures in the three in-core molten pool experiments.

3.4 Containment Analysis (R. L. Knight, 4424)

The Containment Analysis program has been directed toward review and evaluation of phenomenological models for the CONTAIN code during the past quarter. The development of melt-sodium-concrete interaction models has also continued. The review and development of individual phenomenological models have been done in the context of the two primary submodels for CONTAIN/SINTER (Cavity Debris Pool/Material Interactions Model) and the cell atmosphere model (sodium burning, aerosol, and heat transfer models).

A significant part of the SINTER effort involved improvements to the concrete thermal response model in anticipation of incorporating this model into SINTER. Mass transfer routines for both the wet and dry regions of concrete for the sodium-concrete interaction case have been developed and incorporated. An improved algorithm for treating boundary conditions for the energy equation at ablating surfaces has been programmed and inserted into the code, as has a subroutine to calculate temperature-dependent Darcy coefficients.

For applications involving extensive real time calculations, such as the CONTAIN code, the time step required by the existing fluid flow portion of the concrete response model is relatively small. To avoid the problems associated with modeling fluid flow, a steady-state solution of the mass transport equations has been formulated. The new code is presently being programmed and should provide a good comparison with the present code for code verification.

The initial version of the cavity debris pool model is to be based on the existing melt-concrete interaction code, INTER. Considerable revision of the original code has been performed in order to treat sodium as a pool component in the layered structure. This revised version has been restructured into a more modular code with improved heat transfer and layer structures. The details of the sodium-concrete chemistry have not yet been included in this version. The modified cavity pool model will be combined with the concrete thermal response model to form the first version of SINTER.

The cell atmosphere model effort has focused on the review of existing models and the development of the superstructure for the atmosphere model. Generalized implicit heat transfer routines have been written and incorporated into a cell description which allows arbitrary specification of materials and cell liners. The first stage of model integration has been completed to couple the general cell description (heat transfer and mass balance) to the sodium burning models of SPRAY-3 and SOFIRE-2. The basic calculational routines of SPRAY-3 have been incorporated with extensive modification, while the SOFIRE-2 model has been completely reprogrammed for inclusion into the code. The current version is now being checked against sample problems for "stand-alone" versions of these codes. The aerosol review for the CONTAIN code is now being documented and will form the basis for deciding if European models (or a recently completed code from Cal Tech) should be considered for inclusion into CONTAIN instead of HAARM-3. The aerosol model will be incorporated into the cell atmosphere model during the next quarter.

3.5 Fragmentation (T. Y. Chu, 1537; R. L. Coats, 4422)

3.5.1 Introduction

Most severe accident scenarios for advanced sodium-cooled reactor systems involve the production of significant amounts of molten fuel and steel. The ultimate dispersal of this molten material often depends on either bulk freezing of the melt or the establishment of coolable particulate beds. Scenarios which differentiate between the dispersal modes involve questions of the fragmentation of substantial quantities of melt when contacted with sodium.

Two experiments, FRAG 3 and FRAG 4, using UO_2 producing metallothermic mixtures, were performed during this reporting period. The fragments from the second fragmentation experiment, FRAG 2, were classified according to size. Some scanning electron microscope (SEM) examinations of the fragments were also made.

3.5.2 Experiments

On July 31, the first attempt was made to interact a large mass (22.73 kg, 50 lb) of thermitically generated UO_2 melt with about 20 kg (44 lb) of sodium. Unfortunately, a surface layer of solid UO_2 formed prior to plug melt out and the melt was prevented from leaving the burn chamber. This was FRAG 3.

Experiment FRAG 4, which took place on August 28, was a repeat of FRAG 3. A small amount of additional MoO_3 was added to enhance the reaction. At a sodium temperature of 693 K (420°C) the metallothermic mixture (at 323 K, 50°C) self-ignited, precluding the collection of interaction data. Visual observation indicated that the interaction was much milder than in the previous experiments using nontherm-ic mixture. Core samples of the debris bed were taken. The bed was found to vary slightly in thickness at the five locations studied, measuring 1.6 in. in one location and 2.3 to 2.8 in. at the other four locations. A typical fragment weight fraction is shown in Figure 3.5-1. In the bottom of the bed, the fraction is essentially constant at 80%. Current experiments are underway to characterize the average density of the fragments. Knowing density, it is possible to convert the information in Figure 3.5-1 into void fraction which is more useful for debris bed cooling studies. Visual inspection indicates that the degree of size stratification was far less in the experiment reported here than in the previous, more energetic test (FRAG 2). Apparently, energetic events cause more thorough mixing and accentuate terminal velocity effects.

A differential thermal analysis technique has been used to determine the temperature of spontaneous ignition of a metallothermic mixture prepared for Test FRAG 3. The results indicated that the self-ignition was definitely not caused by temperature effects. An investigation of the experimental circumstances indicates that the ignition was probably due to moisture release from the thermite crucible.

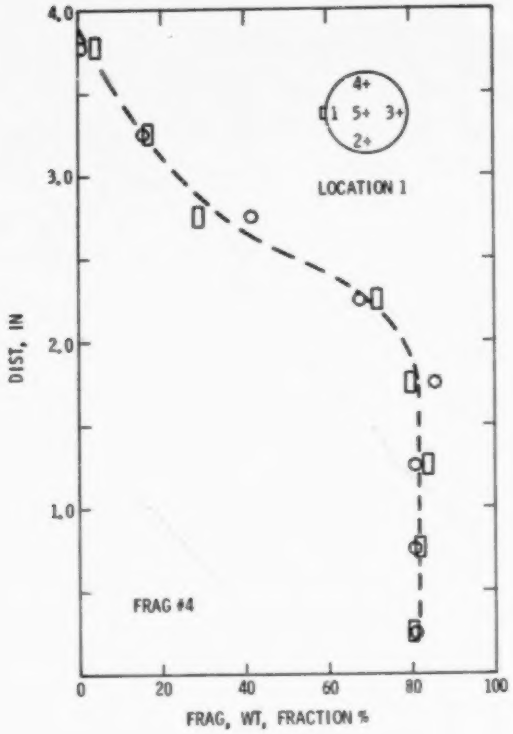

Figure 3.5-1. A Typical Fragment Weight Fraction

Considerable effort was expended modifying the apparatus for dual range instrumentation. This became necessary since the magnitude of the interaction was unpredictable. In future experiments, the pressure will be measured by two transducers with maximum ranges of 100 and 3000 psi respectively. Force will be measured with transducers having maximum ranges of 5000 and 80,000 lb.

3.5.3 Analysis of Results of Test FRAG 2

In Test FRAG 2 approximately 13 kg (28.6 lb) of molten iron and aluminum oxide (produced by an alumino-thermic reduction of magnetite) were released into 23 kg of sodium at 753 K (480°C). The interaction resulted in five separate pressure pulses with magnitudes considerably exceeding 300 psi and probable slug impact which caused permanent deformation of the test vessel head.

The fragments from this test were classified by sieving. The results are shown in Figure 3.5-2 and are tabulated below.

Particle Size	Mass Fraction Less Than Indicated Size (%)
2820	92.7
1190	63.5
850	54.6
600	42.6
425	30.7
212	11.9
106	5.5
45	1.0

Also presented in Figure 3.5-2 is a comparison of the present data with M series from ANL.[3-21]

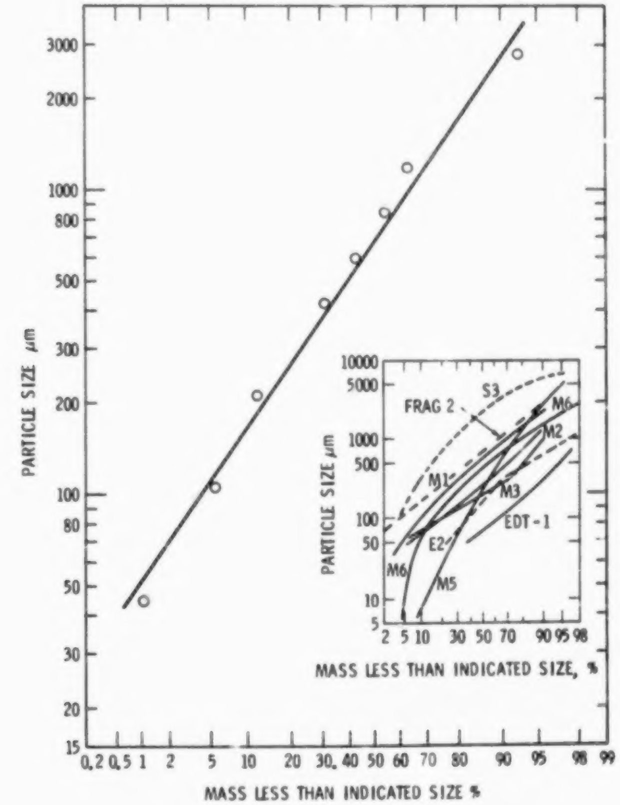

Figure 3.5-2. FRAG 2 Fragments as Classified by Sieving. (The inset shows particle distribution from large-scale out-of-pile experiments.)

As shown in Figure 3.5-2, the particle size distribution can be approximated by a log-normal distribution. The density function can be expressed as:

$$f(\log D) = \frac{1}{\sqrt{2\pi\sigma}} \exp\left[-\frac{1}{2}\left(\frac{\log D - \mu}{\sigma}\right)^2\right]$$

μ = 2.83 (mean particle size 680 μm)

σ = 0.477

D = particle size in μm.

Figure 3.5-3 shows typical SEM from Test FRAG 2. Two-phase particles typical of energetic interactions are shown.

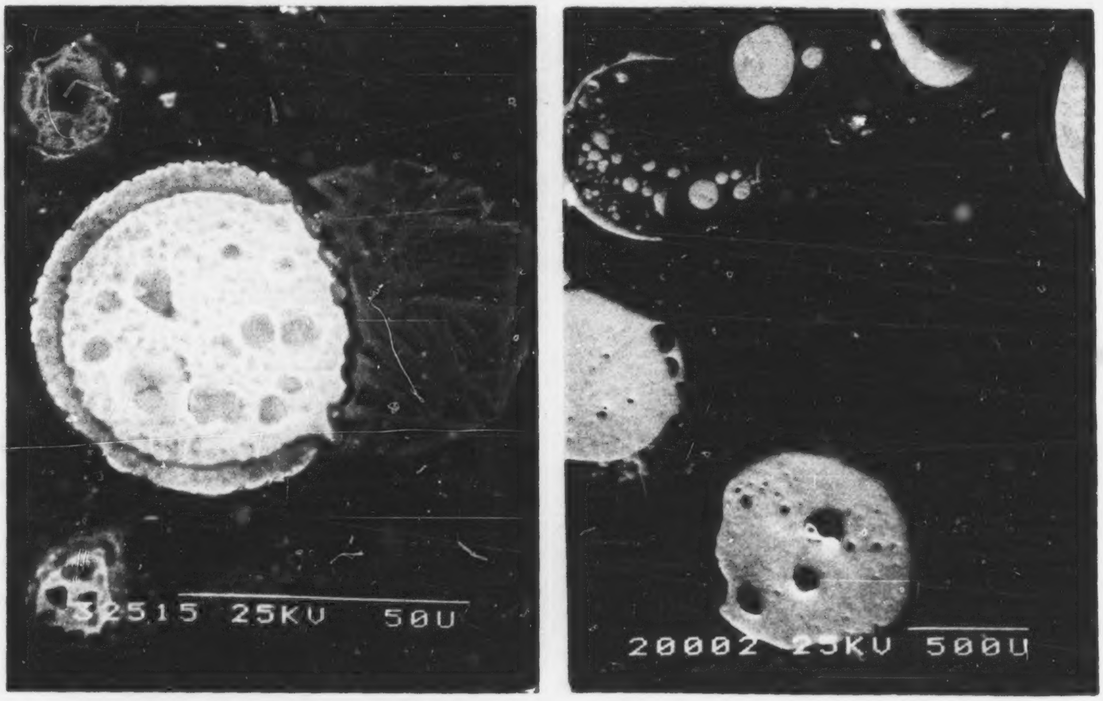

Figure 3.5-3. Typical SEM From FRAG 2 Showing Two-Phase Particles, Typical of Energetic Interactions

3.5.4 Other Activity

The reverse experiment apparatus is being fabricated. Combined interaction experiments with concrete bottom crucibles are being designed. More UO_2 tests will be performed in future quarters and data analysis will continue.

3.6 Sodium Containment and Structural Integrity (R. U. Acton, 1537; R. L. Coats, 4422; N. R. Keltner, 1537; L. A. Kent, 1437; R. A. Sallach, 5846; J. E. Smaardyk, 5534; C. M. Stone, 4431; D. L. Wesenberg, 4431)

3.6.1 Introduction

In the event of vessel or pipe rupture, liquid sodium may come into contact with concrete or other containment materials. This task is aimed at identifying and quantifying the dominant phenomena involved in the erosion and possible breach of containment and in the liberation of gas which may contribute to the breach of containment.

Any loop-type LMFBR system must account for the interaction of hot sodium with cell liners and, given either a failed liner or a CDA, the interaction of hot sodium with concrete. The data base available for safety assessments involving these interactions is limited, especially for the concrete and failed-liner interactions. This program has been specifically developed to provide the research required to verify the data base from a confirmatory point of view.

Basalt aggregate was secured from the same source that furnished construction materials for the Fast Flux Test Facility (FFTF). A series of concrete crucibles using the basalt aggregate was cast for sodium interaction studies. A minimum of 90 days was allowed for curing before any of the crucibles were tested. During this quarter, two experiments were conducted: Tests 11 and 12.

The first instrumented steel plate test in a series of heat flux experiments has been performed at a flux of 10 W/cm^2.

3.6.2 Test 11

Test 11 incorporated the first concrete crucible made from basalt aggregate with FFTF mix design. One hundred twenty-eight kg of sodium at 873 K (600°C) were dumped into the bare cavity of the crucible resulting in a 13.2-cm-deep pool. The crucible cooled the sodium to 703 K (430°C) before the heater could restore the pool temperature to the 823 K (550°C) set point (see Figure 3.6-1). The pool temperature remained at 823 K until the 75-min mark when an exothermic reaction increased the pool temperature to 1043 K (770°C). This reaction continued for about 75 min. At 280 min, the heater failed, terminating the test (however, the sodium may have been exhausted at this time).

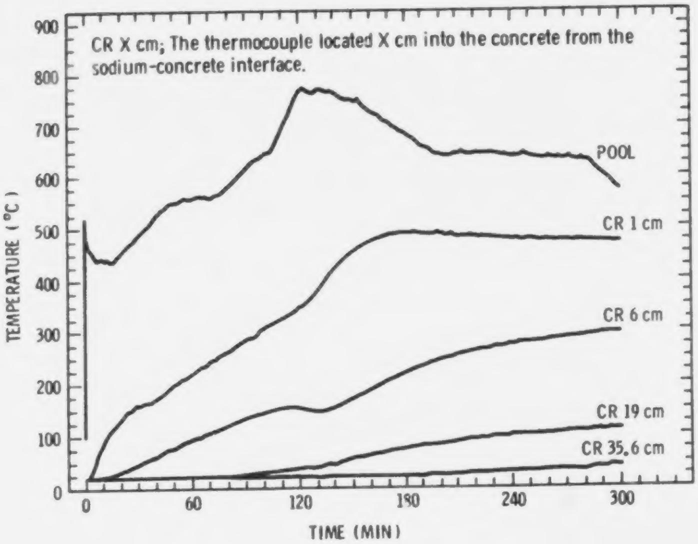

Figure 3.6-1. Crucible Temperatures and Sodium Pool Temperature, Test 11

3.6.3 Test 11 Results

Posttest examination revealed that all of the sodium had reacted with the concrete leaving a cinder-like bed of reaction products. The products at one edge of the cavity burst into flames after being exposed for about 1 min to the atmosphere. The crucible had numerous radial cracks extending completely through the cavity side walls (Figures 3.6-2, -3, and -4). Sodium had preferentially attacked the concrete along these cracks. A model for the exothermic reactions taking place has been developed resulting in the following tentative reaction sequence:

1. Water diffuses from the concrete into the sodium pool and reacts.

$$\mathrm{Na} + \mathrm{H_2O} \longrightarrow \mathrm{NaOH} + \frac{1}{2}\,\mathrm{H_2}$$

2. Sodium hydroxide accumulates in the sodium pool until saturation.
3. A reaction then starts between sodium hydroxide and the SiO_2 of the basalt.

$$\mathrm{2NaOH} + \mathrm{SiO_2} \longrightarrow \mathrm{Na_2SiO_3} + \mathrm{H_2O}$$

The heat generated by (3) above is not thought sufficient to raise the pool temperature the observed amount. Rather, the main heat source is believed to be the reaction of the released water of (3) with the sodium as in (1).

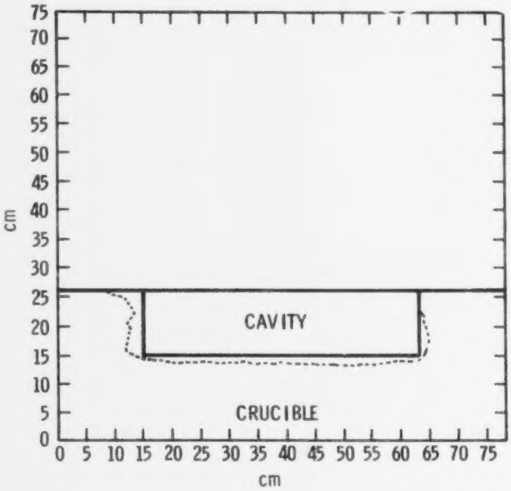

Figure 3.6-2. Basalt Concrete Crucible Penetration, Test 11

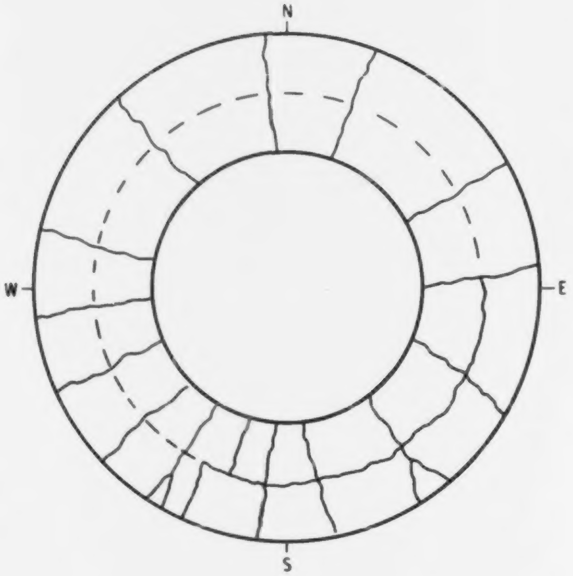

Figure 3.6-3. Top View of Crack Pattern of Basalt Concrete Crucible, Test 11

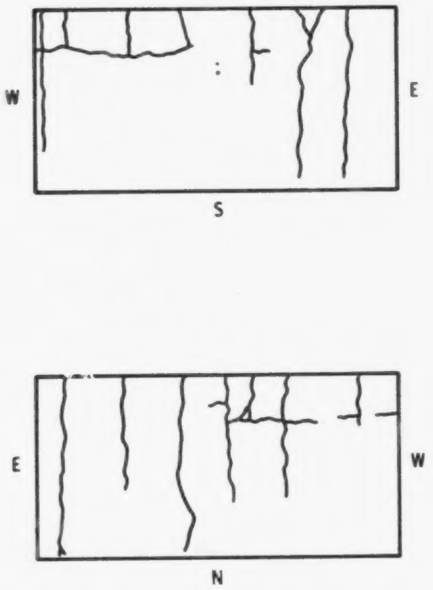

Figure 3.6-4. Side Views of Cracking Pattern of Basalt Concrete Crucible, Test 11

The chemical analysis of two samples of reaction products is given in Table 3-VII. One sample was obtained from the bottom of the crucible cavity near the center. The second sample was taken from the side of the crucible cavity near the top edge. Substantial amounts of NaOH were found along with some NaH. There was more NaOH in the bottom sample as would be expected from the hypothesized chemical reactions.

Table 3-VII

Chemical Analyses of Reaction Products, Test 11

	Crucible Cavity	
Constituents	Bottom/Center (%)	Side/Top (%)
$NaOH$ (+Na_2O)	40	18
NaH	3	3
Na_2CO_3*	10	6
SiO_2	20	40
Al_2O_3	9	10
Fe_2O_3	9	10
CaO	9	13
	100	100

*Probably from CO_2 in atmosphere reacting with NaOH of residues.

Other analyses (SiO_2, Al_2O_3, etc) were as expected from the concrete composition.

3.6.4 Test 12

For Test 12, the concrete crucible also was made with basalt aggregate to FFTF mix design. The crucible cavity was lined with two layers of firebricks and a steel insert to simulate FFTF cell design (Figure 3.6-5). The steel insert was purposely flawed to simulate a failed liner which would allow the sodium to contact the firebrick. The simulated flaw in the bottom of crucible was instrumented with strain gages to furnish data on thermal stresses in the insert and possible flaw propagation. In addition to the normal crucible thermocouples, thermocouples were also placed between the insert and the dense firebrick, between the dense firebrick and the insulating firebrick, and between the insulating firebrick and the concrete. Sixty-eight kilograms of sodium at 873 K (600°C) were dumped into the lined crucible cavity. Initial pool depth was 30.5 cm. Following initial cooling, after the heaters had restored sodium-pool temperature to 823 K (550°C) and maintained it for approximately 15 min, an exothermic reaction started in the first layer of firebrick (Figure 3.6-6). Temperatures in this layer reached approximately 1123 K (850°C). A short time later, a temperature excursion was detected in the second layer of firebrick, followed by an excursion at the firebrick-concrete interface. Here (3 hr into the test) the depth of the sodium pool had dropped 20.3 cm. A sodium-limited test was considered undesirable, so a second dump of 45.5 kg of sodium was made. Because of the time necessary to make the second sodium dump and because of the original sodium depletion, the experiment was cooling down. A large volume of gas vented from the test chamber when the second sodium dump was made, indicating that the crucible was badly cracked and was venting into the test chamber. The depletion of the original quantity of sodium may have caused a passivation of the reaction surfaces as the fresh sodium did not appear to restart the exothermic reactions. In the eleventh hour of the test, an explosion occurred in the test chamber, presumably caused by hydrogen gas, terminating the experiment.

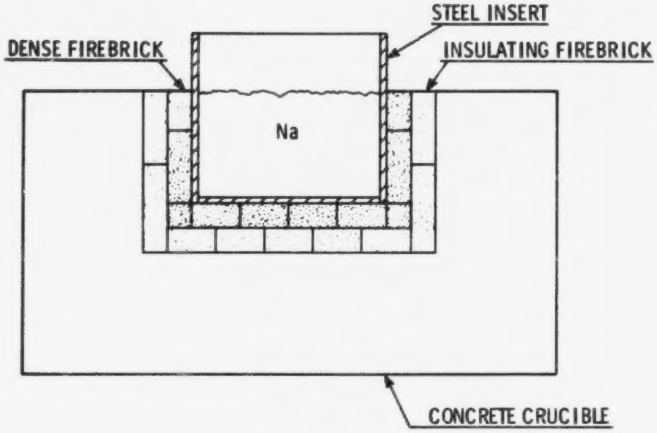
STEEL INSERT
DENSE FIREBRICK
INSULATING FIREBRICK
Na
CONCRETE CRUCIBLE

Figure 3.6-5. Arrangement of Firebrick and Insert in Concrete Crucible Cavity, Test 12. (TOPHAT and other test features not shown.)

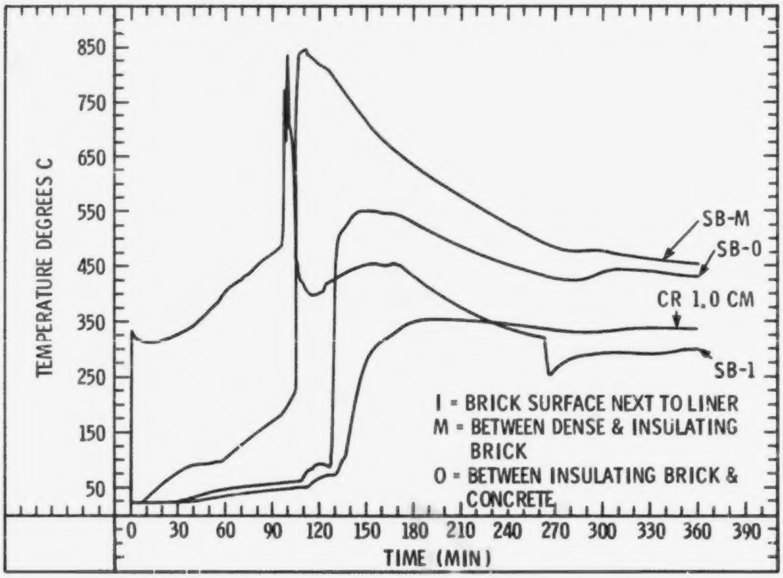

Figure 3.6-6. South Brick (SB) Temperatures and Crucible (CR) Temperature (South Side)

3.6.5 Test 12 Results

Posttest examination revealed that all 113.5 kg of sodium had been consumed. The reaction products from the sodium-firebrick interaction had bulged the bottom of the insert, in the direction of the cavity, about 4 cm, giving it the appearance of the bottom of an aerosol spray can (Figure 3.6-7). No radial distortion of the liner was noted. The upward force of the products was strong enough to break two of the four turnbuckles that were used to hold and seal the top hat-liner assembly to the concrete crucible. The concrete crucible was more severely cracked than the bare crucible of Test 11 (Figure 3.6-8). Crack widths at the outer circumference were as much as 2.54 cm. Because this test was sodium limited, the sodium had not penetrated beyond the firebricks into these cracks as it did in Test 11.

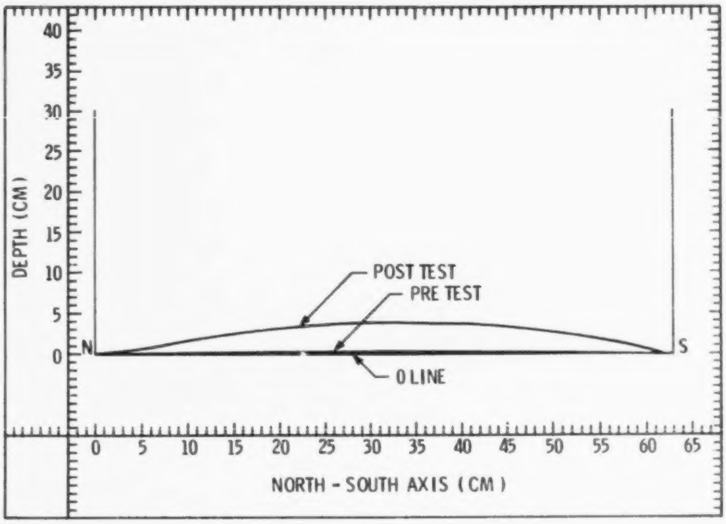

Figure 3.6-7. Test 12 Liner Configuration Posttest vs Pretest

The firebricks around the cavity side wall had reacted with the sodium and changed color from light tan to a blue-black; however, the firebricks retained their shape and position. The firebricks on the bottom underwent the same color change but could no longer be discerned as individual bricks. They had become a semi-homogenous mass that partially stuck to the bottom of the steel liner.

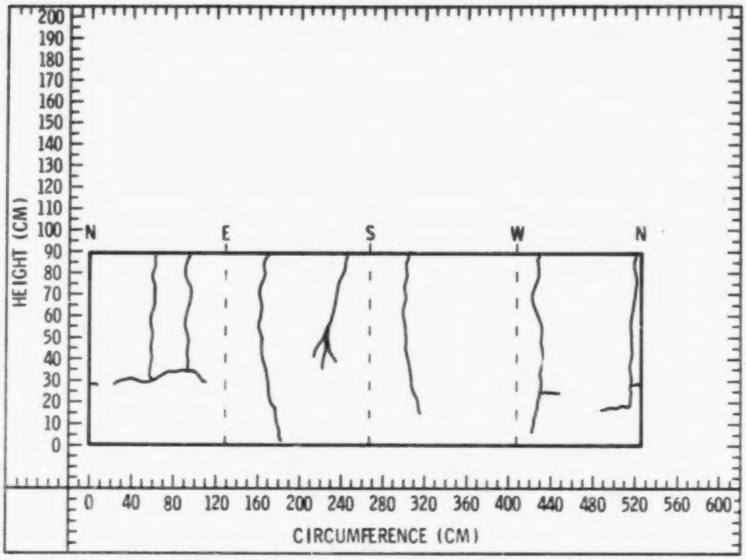

Figure 3.6-8. Test No. 12 Posttest Circumferential Distribution of Radial Cracks

The large percentage of SiO_2 makes the firebrick composition similar to that of the basalt concrete and, consequently, the same exothermic reactions are to be expected. In a bare crucible, it is believed that the entire sodium pool must saturate with NaOH before the exothermic reaction can begin. In a crucible with firebrick and liner, however, it is believed that only the sodium in the gap between the liner and firebrick or within the pores of the firebrick need saturate before the reaction can begin.

An analysis of the firebricks used in Test 12 is given in Table 3-VIII and are reported to be the same as those used in FFTF construction.

Table 3-VIII

Analysis of Firebrick

	Oxide (%)							
Type of Firebrick	SiO_2	Al_2O_3	Fe_2O_3	CaO	MgO	TiO_2	Alkalies	Bulk Density (kg/m^3)
Insulating M-20	57-60	33-36	1-2	0.1-1.6	0.01-0.6	1.5-2.5	1.2	600-700
Dense Morex	56	38	2	0.6	0.6	1	1.6	2130-2190

3.6.6 Structural Integrity

The first instrumented steel plate test in a series of heat flux experiments has been performed. The test involves the use of heat lamps to irradiate a central circular portion of a clamped 15-in.-square steel plate. The plate size approximates a section of a steel cell liner whose anchor spacing is 15 in. This test and subsequent tests will serve as benchmarks to experimentally verify both the numerical procedure and the high-temperature strain gages.

Thermocouples, resistance thermometers, high-temperature strain gages, and displacement gages were used to instrument the plate. The test series will investigate heat flux values from 10 W/cm^2 through 150 W/cm^2. The first test was conducted at a flux of 10 W/cm^2. In addition to the test program, there is an analytical effort to predict the plate temperature distribution, strain, and displacements. The general-purpose finite-element program, MARC, was used for the calculation of plate stresses, strains, and displacements. Heat transfer calculations were made using the COYOTE finite-element program. Analyses have been performed for each of the planned experiments. Comparison of the analytical and experimental data from the first test is encouraging but the results are not complete. New tests are being conducted at the higher flux levels.

References for Section 3

3-1. Light Water Reactor Safety Research Program Quarterly Report, April-June 1978, Nuclear Fuel Cycle Safety Research Department, SAND78-1901, NUREG/CR-0422, Sandia Laboratories, Albuquerque, NM, January 1979.

3-2. D. A. Powers, et al, Exploratory Study of Molten Core Material/Concrete Interactions, SAND77-2042, Sandia Laboratories, Albuquerque, NM, February 1978.

3-3. H. G. Plein, Sandia Laboratories, Albuquerque, NM (4422), unpublished results.

3-4. D. A. Powers, Core Meltdown Experimental Review, Chapter 9, SAND74-0382 (Revised), Sandia Laboratories, Albuquerque, NM, 1974.

3-5. Light Water Reactor Safety Research Program Quarterly Report, January-March 1978, Nuclear Fuel Cycle Safety Research Department, SAND78-1511, Sandia Laboratories, Albuquerque, NM, October 1978.

3-6. D. A. Powers, Sustained Molten Steel/Concrete Interactions Tests, A Preliminary Report on the Feasibility of Experimental Techniques, SAND77-1423, NUREG/CR-1066, Sandia Laboratories, Albuquerque, NM,

3-7. J. B. Rivard, "Preliminary Results from Initial In-Pile Debris Bed Experiments," Proceedings of the Third Postaccident Heat Removal "Information Exchange," November 2-4, 1977, Argonne, IL, ANL-78-10, pp. 49-61.

3-8. J. B. Rivard, Debris Bed Studies and Experiments at Sandia Laboratories, SAND78-0299, Sandia Laboratories, Albuquerque, NM, 1978.

3-9. J. B. Rivard, Postaccident Heat Removal: Debris Bed Experiments D-2 and D-3, SAND78-1238, NUREG/CR-0421, Sandia Laboratories, Albuquerque, NM, 1978.

3-10. V. S. Arpaci, Conduction Heat Transfer, Addison-Wesley Publishing Company, Reading, MA, 1966.

3-11. Budnikov, et al, Proceedings of the Second United Nations International Conference on the Peaceful Uses of Atomic Energy, A/CONF 16/P 12193, July 1958.

3-12. D. G. Swanson, E. H. Zehms, C. Y. Ang., H. L. L. Van Paassen, and A. R. Marchese, "Molten Core Debris Interactions with Core Containment Materials," Proceedings of the Third Postaccident Heat Removal," Information Exchange, November 2-4, 1977, Argonne, IL, ANL-78-10.

3-13. H. W. Godbee and W. T. Ziegler, J. App. Phys., 37, 1, 56, 1966.

3-14. D. Vortmeyer, Sixth International Heat Transfer Conference, Toronto, Canada, August 1978.

3-15. G. Kasparek and D. Vortmeyer, Wärne-und-Stoffübertragung, **9**, 177, 1976.

3-16. *Properties for LMFBR Safety Analysis*, ANL-CEN-RSD-67-1, 1976.

3-17. Touloukian, *Thermophysical Properties of Matter*, Vol. 3, Plenum Publishing, NY, 1970.

3-18. G. H. Golden and J. V. Tokar, ANL-7323, Argonne, National Laboratory, Argonne, IL.

3-19. E. E. Anderson, Nucl. Tech, **30**, 65, 1976.

3-20. C. Kim, R. Blomquist, L. Liebowitz, ANL-CENI-6863, Argonne National Laboratory, Argonne, IL, 1977.

3-21. L. Baker, Jr., *Postaccident Heat Removal*, ANL-RDP-60, p. 6.58, 1977.

BLANK PAGE

4. AEROSOL SOURCE NORMALIZATION

(R. M. Elrick, 5422)

4.1 Introduction

For those reactor accident scenarios in which the fuel vaporizes and ruptures the cladding, it is necessary that the state of the fuel before and after rupture be characterized by experiment. The first phase of this study conducted in FY77 has measured some of the physical properties of UO_2 fuel pins heated to vaporization by neutrons from a pulsed reactor. Succeeding work will study the interaction of neutron-vaporized fuels with containing structure and with sodium.

Debris properties of the UO_2 fuel (such as particle size, velocity, and density distributions as a function of time) will be measured for both bare and clad fuel pins. This characterization will (1) be used as a particle source term for aerosol codes; (2) be sufficiently accurate and complete to be compared with hydrodynamic code predictions, and (3) be compared with those particles sampled by similar methods in relevant out-of-pile experiments at Oak Ridge National Laboratory in which the fuel material is resistively heated. This comparison of in-pile to out-of-pile techniques will begin to establish limits of interest on the particle density and size spectra of debris from fuel breakup.

4.2 Progress

During this quarter, the second series of in-pile aerosol experiments was designed and fabrication has begun on all components. The experiments will be conducted in the ACRR. The additional fission energy will help produce a temperature profile across the pin diameter similar to that expected in the ORNL comparison experiments while maintaining the required energy dose in the fuel.

The experiment configuration of this series differs from that of the first series in several respects. The fresh UO_2 fuel pin will be supported vertically allowing axially symmetric exposure to the neutrons (see Figure 4.2-1). In this position, the bare pin will be viewed simultaneously from the end and the side by photography. This method of viewing allows a better correlation for determining radial temperature profiles than when the same data were obtained from separate but similar experiments. The new design provides room for making a four terminal measurement of the electrical resistance of the fuel. This measurement will provide better resistance values by essentially eliminating the effect of contact resistance. In the first series of experiments, space limitations required a two-terminal measurement which showed the phase transitions from solid to liquid and from liquid to vapor but, because of large contact resistance, gave unreliable fuel resistance values. A pumping system was designed for use in-pile to maintain vacuum in the experiment canister during temperature conditioning of the fuel by multiple pulsing or resistive heating. To accommodate the pumping system and the new area for photographic viewing of the fuel, the top of the canister is being redesigned.

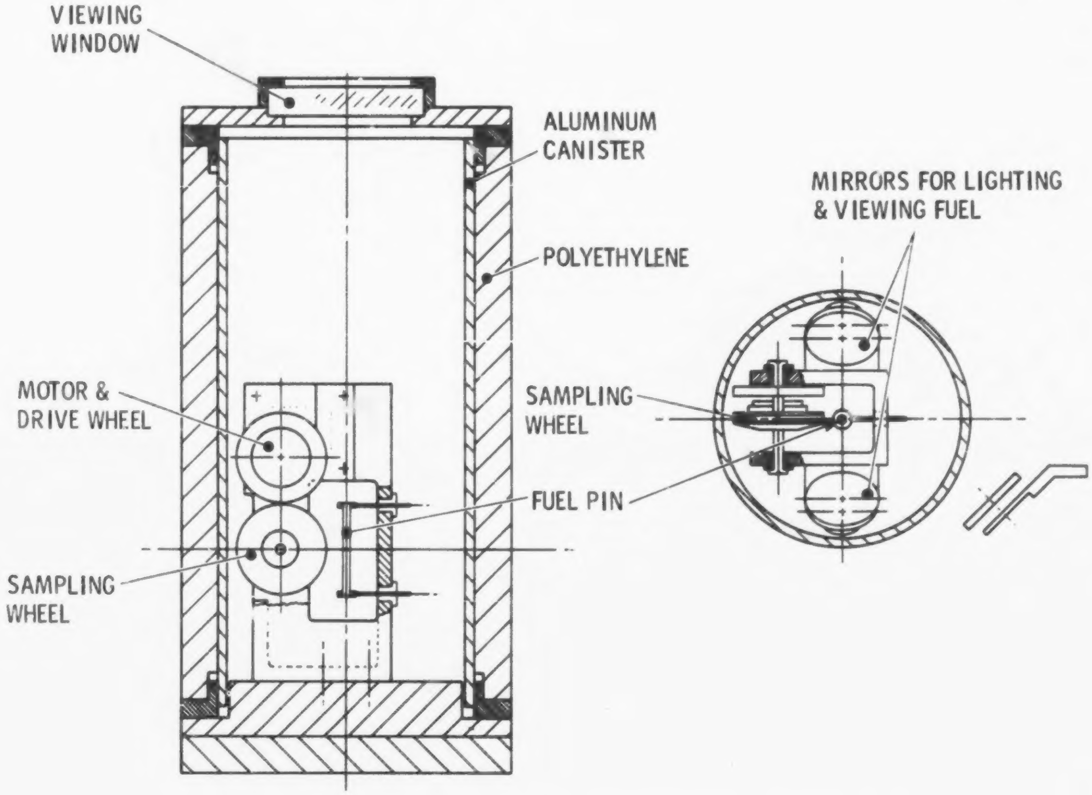
VIEWING WINDOW
ALUMINUM CANISTER
MIRRORS FOR LIGHTING & VIEWING FUEL
POLYETHYLENE
MOTOR & DRIVE WHEEL
SAMPLING WHEEL
FUEL PIN
SAMPLING WHEEL

Figure 4.2-1. Schematic of Experimental Canister To Be Used for In-Pile Aerosol Source Experiments, Series II

Time-dependent size and velocity distributions of the particles from the Series I experiments have been discussed in previous quarterlies. The total particle size distribution for the experiment was obtained by summing distributions from the individual collection channels. The total mass distribution shown in Figure 4.2-2 was obtained by calculating particle mass from particle size with the bulk density of UO_2. As the figure shows, about 30% of the total mass is in particles smaller than 2 to 3 nm and about 60% of the mass is in particles larger than 1 mm in size.

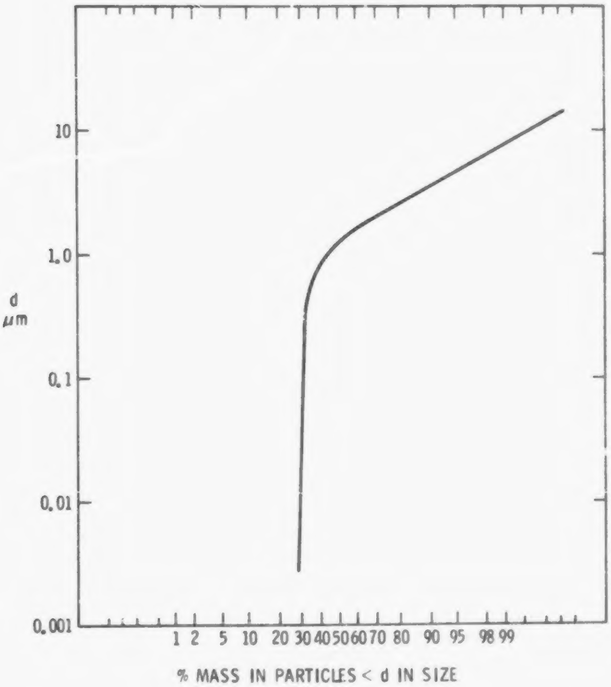

Figure 4.2-2. Distribution of Total Particle Mass According to Size for Particles Sampled in In-Pile Aerosol Source Experiment, Series I

In the out-of-pile sampling experiments scheduled to be run at ORNL, the aerosol source produced by resistively heating the fuel will be compared with the source term produced by neutronically heating the fuel as described in this series of in-pile experiments. ORNL has solved the arcing problem experienced when capacitance discharge was used to heat UO_2 fuel at reduced pressure. The fuel can now be preheated, then pulse-heated while maintaining a chamber pressure of about 0.1 torr, equal to that used in the in-pile experiments. ORNL has scheduled the close-in sampling tests for December or January. The last three of six sampling wheels being prepared for this series of experiments are nearing completion.

Next quarter, details of the out-of-pile sampling study will be discussed with ORNL. Parts for the Series II aerosol experiments will be checked, assembled, and developed for in-pile experiments subsequent to the out-of-pile comparison tests.

5. ELEVATED TEMPERATURE DESIGN ASSESSMENT

(W. A. Von Riesemann, 5431; J. A. Van Den Avyle,
5835; W. B. Jones, 5835; C. M. Stone 5431;
D. W. Lobitz, 5431; W. B. Gauster, 5111;
J. Gieske, 9352)

5.1 Introduction

The primary objectives of the elevated-temperature design assessment studies are (1) to develop correlative NDE techniques that can be used to monitor progressive creep, fatigue, and combined creep-fatigue damage in materials used in advanced reactor primary- and secondary-loop components; (2) to evaluate analytical methods and correlate with experimental data for creep buckling of advanced-reactor components operating at elevated temperatures; and (3) to design, fabricate, and operate a multiaxial creep-fatigue facility for the purpose of evaluation of creep-fatigue damage rules.

5.2 Creep-Fatigue Test Program* (Uniaxial Loading)

5.2.1 Creep Testing

Creep Test 316-C-7 was terminated short of failure after 2,204 hr at a total axial strain of 8.3% (Table 5-I). While neither this test nor Test 316-C-5 went to failure, the strain levels achieved were significantly large, and samples of these will be checked by Positron Annihilation (PA) (see Section 5.3.2) to assess the sensitivity of the method. Further creep tests to other damage levels will be run if the PA results are promising.

---

*Test material is Type 316 stainless steel.

Table 5-I

Creep Testing of Type 316 Stainless Steel

Specimen No.	Temp* (°F)	d_o (in.)	Load (lb)	Stress (ksi)	t (hr)	d_f (in.)	E_t (%)
316-C-1	1131	0.505	6005	30.0	226	-	-
316-C-2	1131	0.505	5309	26.5	549	-	-
316-C-3	1131	0.505	4808	24.0	526	-	-
316-C-4	1131	0.506	5109	25.4	802	-	-
316-C-5	1100	0.506	4929	24.5	1991	0.439	5.1
316-C-6	1100	0.506	5328	26.5	Furnace failure		
316-C-7	1100	0.505	5506	27.5	2204	0.493	8.3

*In specimens 316-C-1 through C-4, the temperature distribution was 1131°F (center), and 1027°F (bottom). These four failed at the top due to the uneven temperature distribution, and a measure of uniform axial strain (E_t) was not meaningful.

**Temperature distribution 1100°F (center) ±2°F along specimen axis.

Note: 1100°F = 593°C, 30 ksi - 206.8 MPa.

5.2.2 Creep-Fatigue Testing

Three additional tests were completed at Mar-Test Inc. Test 316-MTF-12 (866 K or 593°C, 0.5% total strain range, 10 min compressive hold) was run out to 3000 cycles without a failure. As reported in the previous quarterly report, this test had shown visual evidence of surface "cracking at 1680 cycles, a lower number of cycles to initiation than was observed for either the zero-hold test or the 10-min tensile hold tests (Table 5-II). Posttest examination at 3000 cycles showed numerous large cracks--one extended through 120° of circumference and the specimen was close to failure. Thus the numbers of cycles to failure for both the tensile and compressive hold period tests were essentially equivalent (Table 5-II). This result conflicts with other data reported for this steel which generally shows tensile hold periods to be very detrimental to life and compressive holds to have little effect.[5-1] An additional test will be run at Mar-Test Inc. to verify this result.

Table 5-II

Type 316 Stainless Steel Creep-Fatigue Test Matrix at Mar-Test Inc.
(All tests at 593°C (1100°F) at a strain rate of 4 x 10^{-3}/s)

Specimen No.	Strain Range (%)	N (cycles)	Hold Time Tensile (min)	Hold Time Compressive (min)
316-MTF-1	Void	-	-	-
316-MTF-2	0.5	9014*	0	0
316-MTF-3	1.0	984*	0	0
316-MTF-4	1.0	1632*	0	0
316-MTF-5	0.5	10078*	0	0
316-MTF-6	Void	-	-	-
316-MTF-7	0.5	1000	0	0
316-MTF-8	0.5	168	10	0
316-MTF-9	0.5	2589*	0	0
316-MTF-10	0.5	5000	0	0
316-MTF-11	0.5	20	0	0
316-MTF-12	0.5	3000	10	2
316-MTF-13	0.5	3000	0	10
316-MTF-14	0.5	3000	10-min hold at zero stress	
316-MTF-15	Tensile test for Modulus and Poisson's Ratio determination			

*Test carried to failure

Test 316-MTF-14 (866 K or 593°C, 0.5% total axial strain, 10 min zero stress hold) was run to 3000 cycles and stopped for inspection. The purpose of this test was to check the effect of time at temperature for an equivalent number of cycles as the tension and compression hold time tests. Optical examination of the specimen surface showed the nucleation of one very small crack. This observation is comparable to the tests without hold periods, and for this test with equivalent hold times, but at zero stress, the amount of cracking is much less than for the tests with hold periods with stress. This specimen will be further examined by transmission electron microscopy (TEM) and PA.

A final test of this series was conducted at Mar-Test as an elevated temperature (866 K) tensile test with both axial and diametral extensometry to check the modulus of elasticity, E, and Poisson's ratio, ν. This specimen, 316-MTF-15, yielded a ν of 0.305 and an E of 137.9 GPa (20.0 x 10^6 psi). These values will be checked at Sandia as a function of the plate rolling direction with both an ultrasonic technique and extensometers.

A series of uniaxial fatigue tests of Type 316 stainless steel at 866 K was initiated at Sandia to provide specimens for multiple sequential surface PA measurements as a function of the number of cycles at five different strain ranges. The specimen surfaces are also being observed in the scanning electron microscope (SEM) to measure the extent of surface crack initiation and propagation as a function of the number of cycles. Table 5-III lists the completed tests, including duplicate specimens at each strain range to determine specimen life without interruptions. These tests are being conducted in air under computer control at a constant plastic diametral strain range, $\Delta\epsilon_{pd}$. The sequential tests have received an initial low number of cycles and are waiting surface PA measurement.

Table 5-III

Fatigue Tests for Sequential Surface PA Measurements and Crack Observations
(All tests are 593°C in air environment at a strain rate of 4 x 10^{-3}/s.)

Specimen No.	$\Delta\epsilon_{pd}$	N	N_f	d (nm)
316-PAF-15	0.0030	2500	2500	6.365
316-PAF-16	0.0030	20	-	6.385
316-PAF-17	0.0010	20	-	6.385
316-PAF-18	0.0005	50	-	6.375
316-PAF-19	0.0020	4762	4762	6.415
316-PAF-20	0.0050	10	10	6.375
316-PAF-21	0.0020	10	10	6.415
316-PAF-22	0.0010	29221	29221	6.385
316-PAF-23	0.0005	36500	365000	6.375
316-SLF-1	0.0050	770	770	6.385
316-SLF-2	void	-	-	-
316-SLF-3	0.0005	126240	126240	6.415

Notes:

$\Delta\epsilon_{pd}$ = constant plastic diametral strain
$\Delta\epsilon_{pa}$ = plastic axial strain = $2\Delta\epsilon_{pd}$
$\Delta\epsilon_{ea}$ = elastic axial strain = stress range/area
$\Delta\epsilon_{ta}$ = total axial strain = $\Delta\epsilon_{pa}$ = $\Delta\epsilon_{ea}$.

5.3 Nondestructive Examination

5.3.1 Ultrasonic

No ultrasonic testing was conducted this quarter.

5.3.2 Positron Annihilation

Movement of the positron annihilation (PA) equipment to a new location, and subsequent malfunctions prevented PA measurements to be made for approximately 2 mo this quarter. At the end of September, angular correlation measurements were initiated on a series of sequential fatigue tests (Section 5.2.2), and the doppler broadening equipment was available to measure specimens generated in creep tests and fatigue tests with hold periods.

A set of measurements was initiated before the move, and is part of investigation to determine the species of defects (i.e. vacancies, dislocations, or precipitates) which contribute to the observed increase in PA lineshape parameter, produced by either cold work or low and elevated-temperature fatigue. Both vacancies and dislocations are produced during deformation, and it is important to understand their relative contributions to the total PA measurement. In particular, this would help explain the lower lineshape parameters measured at cyclic saturation for elevated temperature fatigue compared to room temperature fatigue.

An isochronal annealing curve for 25% cold-worked stainless steel was determined by heating one specimen to temperature for 30 min, cooling to room temperature, and taking a Doppler broadening PA measurement. This was repeated with the same specimen and increasing the temperature in 25 K increments up to 1050 K (777°C). The results are shown in Figure 5.3-1 and include baseline data for undeformed material.

The decrease in lineshape parameter with increased annealing temperature is caused by recovery and annihilation of vacancies and dislocations in the deformed metal. Significant reductions in lineshape parameter occur at 500 K (227°C), and by 900 K (627°C) values are only slightly higher than the undeformed condition. This curve shows a fairly continuous drop and shows no indication of separate annealing stages for vacancies and dislocations.

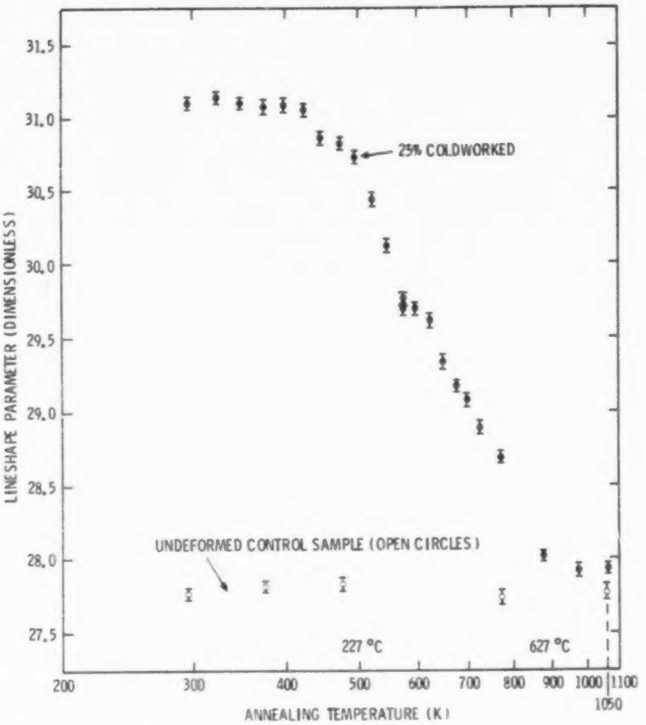

Figure 5.3-1. PA Measurements of Isochronally Annealed 25% Cold Worked Type 316 Stainless Steel

In an attempt to separate the contributions of annealing of vacancies and dislocations, a similar curve was determined measuring microhardness rather than PA lineshape parameter. Curves for 25 and 75% cold work are shown in Figure 5.3-2. Microhardness should be sensitive to dislocation density and precipitates only; changes in vacancy concentration would not affect microhardness. The curve for 25% cold work in Figure 5.3-2 shows only a moderate decrease, beginning at 873 K (600°C), finally dropping to the undeformed value after annealing at 1338 K (1065°C). Similar behavior is measured for the 75% cold worked sample. An additional PA annealing curve for 75% cold worked material will be determined.

In comparing the PA and microhardness curves at 25% cold work, a tentative explanation is that vacancy annealing begins near 503 K (230°C) and is nearly complete by 903 K (630°C). Dislocation annealing, determined by microhardness readings, becomes significant only above 873 K. This implies that vacancies produced in fatigue at 873 K would quickly anneal, and PA measurements of cycled samples would only respond to dislocation defects. PA readings of room-temperature fatigued samples would sample both vacancies and dislocations, and the saturation value of lineshape parameter would be higher. This has been qualitatively observed in the results of lineshape parameter versus number of fatigue cycles.

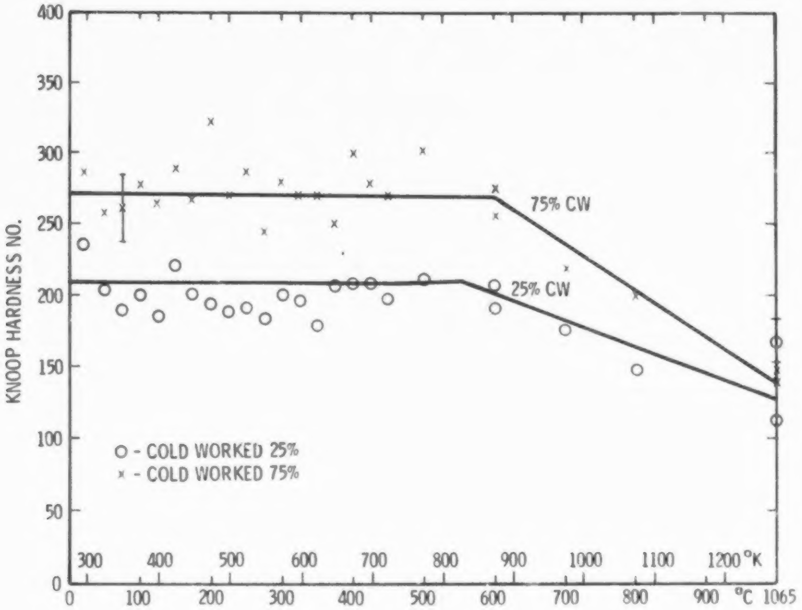

Figure 5.3-2. Hardness of Isochronally Annealed 25% and 75% Cold Worked Type 316 Stainless Steel

5.4 Microstructural Analysis

Transmission electron microscopy (TEM) observations have been completed on samples fatigued at low strain ranges at room temperature ($\Delta\epsilon_t = 0.6\%$) and 866 K ($\Delta\epsilon_t = 0.5\%$). Detailed results will be reported in detail in a future topical report. The general conclusions are:

1. Large variations in dislocation substructure are seen from grain to grain within a single sample for both high- and low-temperature fatigue. These structures are described below. The variations make it difficult to generalize a single description of a sample.

2. Dislocation structures produced by fatigue at room temperature at low-strain ranges are qualitatively different from structures produced at high-strain ranges. Cell structures are not formed at low-strain ranges; instead, after a large number of cycles the dislocations in most areas lie in linear bands with empty areas between bands. In some areas the dislocations form a tangled structure.

3. In fatigue at 866 K, small carbide precipitates nucleate on the dislocation structure which forms early in life. These structures can be linear bands or tangles. Other dislocations formed later in life are not decorated with carbides.

4. Dislocation densities observed in low- and high-temperature fatigued samples at roughly equivalent strain ranges and cycle numbers are qualitatively equivalent.

5. In one sample (316-MTF-9) which was cycled with a 10-min tensile hold period, carbide precipitation was massive on both dislocations and on grain boundaries. This sample was in testing for a much longer time than nonhold tests (433 hr vs 7 hr). The role of grain-boundary carbides on the fracture process is being investigated.

5.5 Multiaxial Test Facility

The high pressure argon gas supply for the multiaxial facility was delivered to Sandia on August 14, 1978 and was transferred to the Pressure Safety Laboratory for a pressure test. Segments of the system were successfully pressurized to 131 MPa (19,000 psi) which is approximately 1.5 times the maximum allowable working pressure of the system. Pressure relief components of the system were also checked. The pressure supply system was moved to the Metallurgy Testing Laboratory, and installation of the system and its required utilities was completed on September 15, 1978. The supplier, MTS Systems Corp, performed a system checkout and calibration on September 26, 1978. The pressure system was shown capable of cycling between 0.14 and 70 MPa (20 to 10,000 psi) within a 40-s period; faster rates are possible with a smaller pressure range. In addition, the system can maintain a set pressure in this range accurate to ±7 kPa (±1 psi).

5.6 Creep-Fatigue Damage Analysis and Analysis of Piping Elbows

5.6.1 Creep-Fatigue Damage Analysis

Work this quarter was directed toward the completion of the design of tubular biaxial test specimen which will be used in the multiaxial test facility (Section 5.5). Since buckling of the specimen is to be precluded, and the wall thickness is to be as thin as possible, analyses were directed toward this area. The preliminary analyses were completed and currently a set of operational curves as a function of temperature is being developed which, given the axial load, will prescribe the maximum allowable internal pressure so as to preclude buckling.

5.6.2 International Benchmark Activities

Participation in the International Benchmark Project was initiated by the Subcommittee on Elevated Temperature Design of the Pressure Vessel Research Committee (PVRC) of the Welding Research Council. Analysis of the two pipe ratchetting experiments (TTT-1 and -2) will be conducted.

5.6.3 Creep Buckling of Piping Elbows

Work continued on the creep-buckling analysis of the proposed Westinghouse-Advanced Reactors Division (W-ARD) 2000-h creep-buckling experiment of a piping elbow at its Multiple Load Test Facility (MLTF). The elastic-plastic behavior of the elbow has been analyzed and 400 h of the 2000-h creep hold were analyzed last quarter. This quarter, an investigation of the stress tolerance used in the convergence criterion in the MARC general purpose computer program has continued. In order for the numerical procedure to be accurate, the stress change for a given time increment must be kept small. In analyses where there is stress relaxation, the allowable creep time step must be reduced so that the stress change within the time step is within an acceptable level for consistency with theory. Creep analyses have been performed with varying stress change tolerance levels.

Additional investigations have been performed to determine differences in the behavior of several types of creep laws when applied to the analysis of piping elbows. Compared were single- and double-term Blackburn Laws and a simple Norton power law on stress. Comparison was made with results from the Japanese PNC piping elbow experiment.[5-2] The simple power law was, as expected, found to be more computationally efficient than the more complicated Blackburn law. The power law models only secondary creep behavior which is a steady-state type of response. The Blackburn law models the primary as well as secondary creep response. It is the rapidly changing primary creep portion of the creep curve which created the computational problems. Figure 5.6-1 shows a comparison between results from a two-term Blackburn law and the simpler Norton power law.

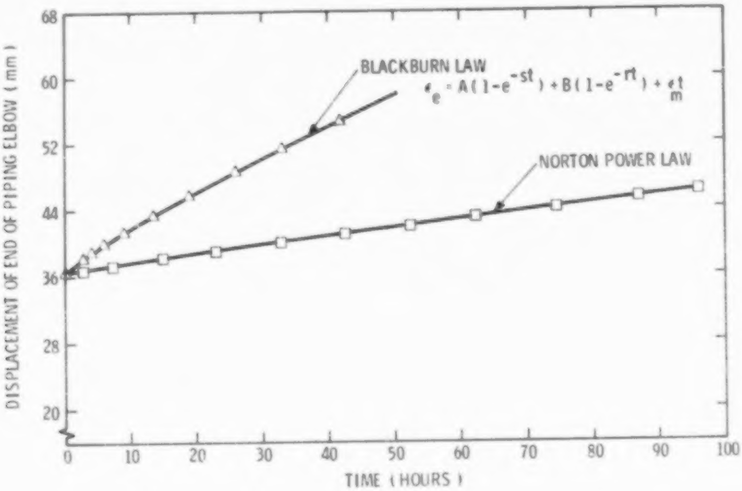

Figure 5.6-1. Comparison of Creep Laws

Figure 5.6-1 is a plot of the displacement of the end of the piping elbow as a function of time during the first creep loading stage. The properties used in these calculations were those given by PNC.[5-2] The Norton power law is given by

$$\dot{\epsilon}_c = A\,\sigma^n$$

where $\dot{\epsilon}_c$ is the creep strain rate, A and n are material constants and σ is the effective stress. The Blackburn law is given by

$$\epsilon_c = A(1 - e^{-st}) + B(1 - e^{-rt}) + \epsilon_m t$$

where ϵ_c is the effective creep strain; A, B, r, s, and ϵ_m are material constants; e is the natural logarithm; and t is time. Further investigations are needed before definitive conclusions can be stated.

References for Section 5

5-1. J. B. Conway, R. H. Stenz, J. T. Berling, Fatigue Tensile, and Related Behavior of Stainless Steels, TID-26135, US AEC, pp. 57-58, January 1975.

5-2. A. Imazu, et al, "Elevated Temperature Elastic-Plastic Creep Test of an Elbow Subjected to In-Plane Moment Loading," Journal of Pressure Vessel Technology, pp. 291-297, May 1977.

BLANK PAGE

6. LMFBR ACCIDENT DELINEATION

(P. S. Pickard, 4424; J. Sholtis,
4424; D. C. Williams, 4425;
P. W. Conrad, 4424)

6.1 Introduction

The principal objective of this program is to determine the applicability of event tree methodology to all phases of LMFBR accidents. The results of the study are intended to (1) provide a demonstrated methodology for developing accident sequence diagrams for an LMFBR, (2) identify and systematize the key phenomena and phenomenological or system uncertainties in the accident sequences, and (3) illustrate the methodology by determining the dominant accident sequences.

6.2 LMFBR Accident Delineation Study

The LMFBR Accident Delineation Study was initiated this past year at Sandia Laboratories to examine the applicability of event tree methodology to the representation of fast reactor accident sequences. This project was sponsored by the NRC as an overview effort to review and evaluate available information on LMFBR accident sequences, and to construct coherent event trees delineating these accident sequences from accident initiation to radiological release from the containment. Qualitatively, the event tree methodology used here is in most respects similar to that demonstrated in WASH-1400 and the CRBR safety study.

Work during this quarter was primarily directed toward preparation of the Interim Report, the draft of which was completed and made available for external review at the end of the quarter. This report summarizes the work completed over the past year and will present some of the major observations made by the staff from the study at this interim stage. The motivation for the study, the methodology, and some limitations of the methodology have been discussed in earlier quarterly reports and, in more detail, in the Interim Report. Therefore, these subjects will not be discussed here.

The development of event trees was carried out in three interacting but relatively distinct areas corresponding to Accident Initiation (Engineered Systems), Accident Phenomenology, and Postaccident Phenomenology (containment analysis). Figure 6.2-1 is a schematic of the LMFBR Accident Delineation program.

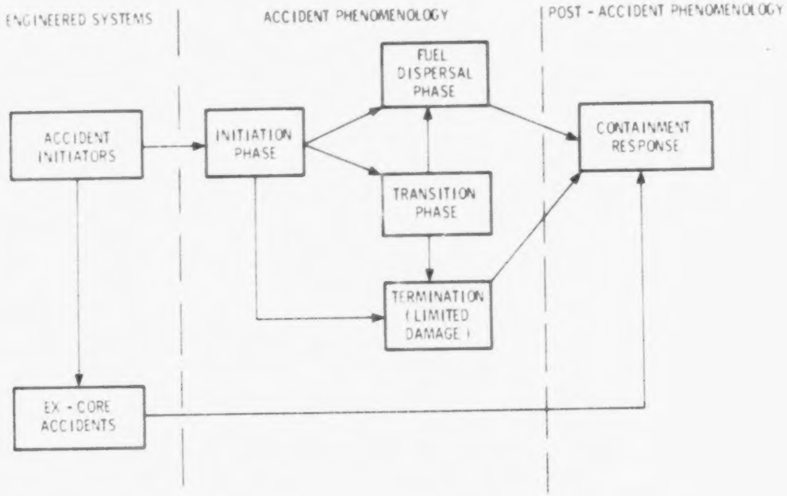
ENGINEERED SYSTEMS
ACCIDENT PHENOMENOLOGY
POST - ACCIDENT PHENOMENOLOGY
FUEL DISPERSAL PHASE
ACCIDENT INITIATORS
INITIATION PHASE
CONTAINMENT RESPONSE
TRANSITION PHASE
TERMINATION (LIMITED DAMAGE)
EX - CORE ACCIDENTS

Figure 6.2-1. Areas of LMFBR Accident Delineation Study

The Accident Initiation and Engineered Safety Systems Response area identified the key systems or subsystems which can affect the generation or transfer of heat during operation and which may, therefore, require a protective response from engineered safety systems (ESS). In each subsystem, failure modes were identified which could lead to accident initiation. The evaluation and categorization of the various combinations of these failure modes and the possible ESS responses provide accident initiation categories for the in-core accident phenomenology phase.

The Accident Phenomenology area categorized the phenomenology involved in the core response to accident initiation. The extreme complexity of Accident Phenomenology in the LMFBR, indicated the utility of decomposing the accident sequences into three distinct subtrees representing input conditions for the Containment Analysis area.

The Containment Analysis area begins with the stage before vessel melt-through and assumes that the vessel damage, if present, can be characterized immediately after the energetic phase of the CDA is over. The condition of fuel debris, bulk sodium, and the decay heat removal system is assumed to dictate the subsequent melt-through behavior. The phenomenology implicit in the early stage of the tree includes Postaccident Heat Removal (PAHR) and engineered systems considerations.

Brief summaries of results for these three areas are presented below followed by concluding observations based upon this interim stage of the study.

6.3 Engineered Systems Summary

The Accident Initiation and Engineered Safety Systems Response area identified the key systems or subsystems which are involved in accident initiation for a three-loop LMFBR. The Clinch River Breeder Reactor design has been used as the exemplary LMFBR for this analysis. However, a strong effort has been made to identify issues that are generic to LMFBR safety independently of CRBR design. One of the primary objectives of the study is to identify potential accident initiation sequences that appear to dominate the risk from an LMFBR. The study thus far has been limited to qualitative analyses of accident sequences that initiate during the operation of the plant. The emphasis, therefore, is on potential accidents involving the core during full-power operation as opposed to spent fuel storage accidents occurring during refueling, etc.

Since the only condition that can result in a core disruptive accident (CDA) involves a system failure in which the core power exceeds the heat removal capability, i.e., overpower or undercooling, two systems have been defined, a Reactor System and a Heat Transport System, to correspond to the generation and transfer of heat, respectively. The Heat Transport System consists of three stages: the Primary Heat Transport System (PHTS), the Intermediate Heat Transport System (IHTS), and the Steam Electrical Generating System (SGS). Within these four basic systems, 14 principal subsystems used directly in the control, generation, and transfer of heat have been defined as illustrated in Figure 6.3-1.

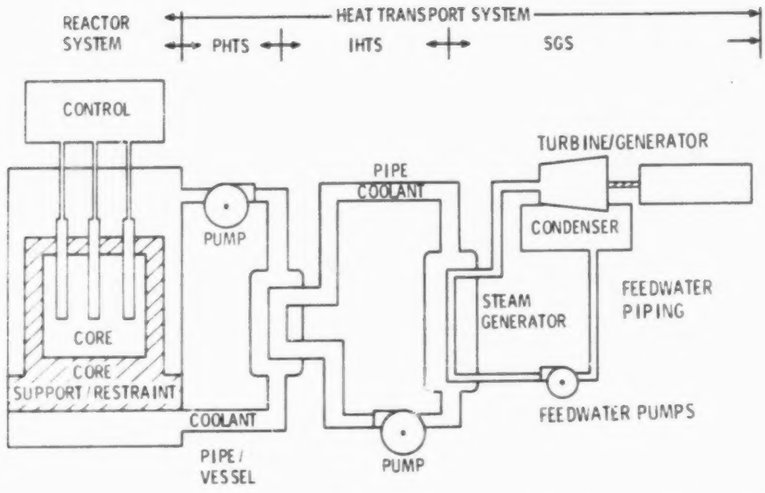
REACTOR
SYSTEM
HEAT TRANSPORT SYSTEM
PHTS
IHTS
SGS
CONTROL
CORE
CORE
SUPPORT / RESTRAINT
PUMP
COOLANT
PIPE /
VESSEL
PIPE
COOLANT
PUMP
TURBINE/GENERATOR
CONDENSER
STEAM
GENERATOR
FEEDWATER
PIPING
FEEDWATER PUMPS

Figure 6.3-1. Schematic of the Principal Systems Essential to the Generation and Transport of Heat

Based on the identification of these 14 basic subsystems, accident "initiators" have been defined as failures or faults within any of these subsystems that affect the generation or transfer of heat during operation and that, if not appropriately mitigated by Engineered Safety Systems, have a significant potential for escalating into a core disruptive accident. This systems approach to accident initiators results in a relatively small but comprehensive set of event trees which represent a reasonable approach to the identification and evaluation of accident initiation sequences.

Consideration of generic subsystem faults has led to the construction of event trees in a particular simple form involving the response of only two engineered safety systems: the Plant Protection System (PPS) and the Decay Heat Removal System (DHRS). The PPS, as used in this study, includes the Reactor Shutdown System and other engineered safety systems such as the Fuel Failure Monitoring System and the Steam Generator Leak Detection System.

The response of the PPS to the initiating subsystem fault is broken down into three separate functions of the Reactor Shutdown System, each one corresponding to a well-defined set of components: Detection, Pump Trip (PT), and SCRAM. The response of the DHRS has not been broken down into separate functions in the present study and, therefore, encompasses all capabilities to adequately remove decay heat. The engineered system event tree sequences have been truncated at the point where they interface with the core accident phenomenology. Outcomes are labeled in accordance with whether they correspond to a safe condition (sequence terminated) or an accident capable of leading to core disruption. In the latter case, the outcomes are assigned to accident categories suitable for continuing the analysis in the core accident phenomenology area. Figure 6.3-2 gives an example, illustrating a reactor control subsystem failure together with the physically meaningful combinations of successful or unsuccessful detection, pump trip, SCRAM, and decay heat removal yielding eight sequences denoted by the letters A through H.

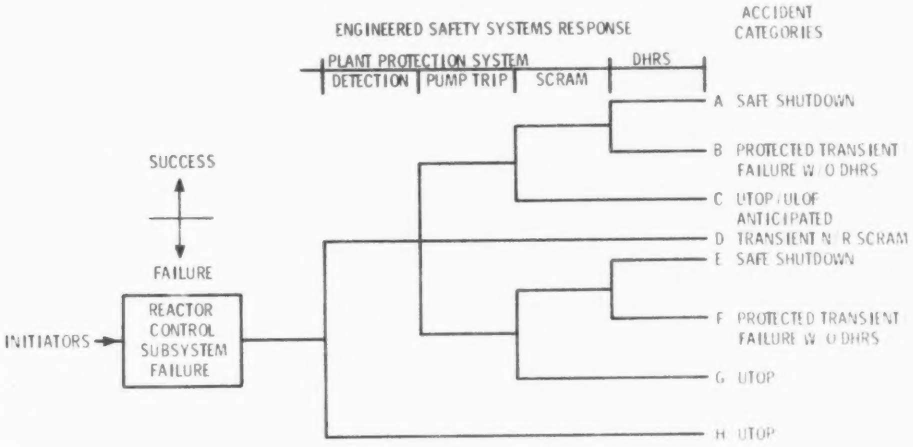

ENGINEERED SAFETY SYSTEMS RESPONSE
ACCIDENT CATEGORIES
PLANT PROTECTION SYSTEM
DHRS
DETECTION
PUMP TRIP
SCRAM
SUCCESS
FAILURE
INITIATORS
REACTOR CONTROL SUBSYSTEM FAILURE
A SAFE SHUTDOWN
B PROTECTED TRANSIENT FAILURE W/O DHRS
C UTOP/ULOF
ANTICIPATED
D TRANSIENT N/R SCRAM
E SAFE SHUTDOWN
F PROTECTED TRANSIENT FAILURE W/O DHRS
G UTOP
H UTOP

Figure 6.3-2. Event Tree for a Reactor Control Subsystem Failure

The resulting specific accident categories depend, of course, on the particular initiating subsystem failure. However, for all initiating subsystem failures, the outcomes fall into four general groups as follows:

1. No core disruptive accident develops, prevented by either safe shutdown, as in Sequences A and E, or continued operation within tolerance, Sequence D.
2. Protected accidents in which shutdown occurs but core disruption eventually results from inability to remove decay heat, Sequences B and F.
3. No protective action takes place and an unprotected transient or failure results, Sequences G and H. In the present case, where

the initiator is a reactor-control-subsystem failure, the accident category would be unprotected transient overpower (UTOP).

4. The initiator is detected, pump trip succeeds, but SCRAM fails, resulting in an unprotected loss-of-flow combined with the initiating transient failure, Sequence C. For the example illustrated, the accident category resulting would be a combined unprotected transient overpower and loss-of-flow (UTOP/ULOF).

In the manner just illustrated, initiating failures in each of the 14 key subsystems were combined with the event trees describing possible PPS and DHRS responses. Fifteen possible outcome categories were defined in this way. These categories are listed in Table 6-I, subdivided according to the four general groups just noted. Detailed discussion of these categories will not be given here, but the following two points may be noted.

1. Categorization of CDAs resulting from DHRS failure is very incomplete; more work is required in this area.
2. Categorization of the general class of unprotected accidents, in which SCRAM fails is believed to be reasonably adequate, except for some partial redundancy.

Table 6-I

Possible Outcome Categories for a Reactor
Control Subsystem Failure

I. No CDA Results

Safe shutdown

Anticipated transient or failure not requiring SCRAM (ATNS)

II. CDA Results from DHRS Failure

Protected transient or failure without DHRS

Rupture of the Primary Boundary without DHRS

Table 6-I Cont.

III. Unprotected Transient or Failure

Unprotected core fault (UCF)

Unprotected step insertion (U-step)

Unprotected transient overpower (UTOP)

Unprotected loss-of-flow (ULOF)

ULOF - two pumps

Unprotected loss-of-heat-sink (ULOHS)

Unprotected rupture of the primary boundary (URPB)

IV. Unprotected Transient or Failure and Loss-of-Flow

UCF/ULOF

U-step/ULOF

UTOP/ULOF

URPB/ULOF

(Other possibilities differ negligibly from standard ULOF).

6.4 Accident Phenomenology Summary

As in other portions of the LMFBR Accident Delineation Study, the event tree methodology proved to be a useful way both to systematically organize the existing body of information on LMFBR accident phenomenology, and also to represent the major uncertainties that remain. First it was found necessary to understand and accept limitations imposed on the methodology by two difficulties which are general to the Delineation Study, but which are particularly significant in the Accident Phenomenology area.

The first of these limitations is the fact that some of the most important branch points represent phenomenological uncertainties. This problem, discussed in some detail in the Interim Report, would seriously complicate the interpretation of any attempt to quantify the event trees; however, it did not interfere greatly with the development of the qualitative trees which were the goal of the present stage of this work. The second of these problems is that the event tree formalism is not very well suited for cases where key questions involve the magnitude of parameters which can assume a continuous range of values, rather than just one or two values. This problem is especially evident when a number of such parameters act in parallel, and it is the net effect that governs subsequent events. The net reactivity effect arising from the many different material response phenomena would be one important example.

In applying the event tree methodology to the Accident Phenomenology area, the first step was to divide the accident sequences into three phases: initiation phase, transition phase, and fuel dispersal phase. The first two of these phases are defined conventionally; the fuel dispersal phase is defined to begin with the dispersal of sufficient fuel to leave the core region permanently subcritical, provided fuel does not reenter. It consists primarily of evaluation of disassembly work energetics and FCI effects, including pressure-driven reentry and recriticality, and thus defines the mechanical insult to the containment.

Initially, generic subtrees were developed for each of the three accident phases noted above. These subtrees were intended to apply to all accident categories. As the Delineation Study progressed, it became apparent that the various accident categories differ sufficiently during the initiation and transition phases so that much useful information would be omitted from any event tree sufficiently general to apply to all accident categories. Hence, category-specific initiation phase and transition phase event trees were developed for the Unprotected Loss-of-Flow (ULOF) and Transient Overpower (UTOP) accidents. Category-specific trees were found to be necessary for delineation of the fuel dispersal phase, however, and it was discussed generically.

The LMFBR safety community has devoted a great deal of study to ULOF and UTOP accidents while much less effort has been directed toward other whole-core initiators. Inevitably, the present Delineation Study reflected this division of effort. Detailed review and delineations were carried out for ULOF and UTOP accidents, and much more limited consideration was given to other accident categories. The following are very brief summaries of the principle conclusions. Slightly more detailed summaries are contained in Chapter I of the Interim Report while a full discussion appears in Chapter IV of that report.

6.4.1 ULOF Accidents

The early portion of a ULOF accident in a core with a substantial positive void coefficient, such as CRBR, is characterized by considerable positive reactivity insertion due to voiding of the higher power/flow ratio subassemblies, and perhaps clad relocation. The resulting power surge can cause rapid pin failures in lower-power subassemblies, resulting in a sequence commonly called LOF-driven-TOP. In this sequence, there are a number of phenomena which can, in principle, lead to high, sustained reactivity ramps and disassembly. Determining whether this actually occurs in practice requires resolution of a number of complex interacting phenomenological questions. These questions may be divided into two categories:

1. Those which determine whether a LOF-driven-TOP actually does develop. Given sufficient rapid negative reactivity feedback from such effects as early fuel dispersal in high-power subassemblies, the accident tempo may be slowed sufficiently to permit voiding of the lower-power subassemblies by normal boiling prior to pin failure. In this case, the question of LOF-driven-TOP consequences is bypassed.

2. Pin-failure and post-pin-failure phenomenologies if a LOF-driven-TOP does develop. These are complex and require much more study, but, at present, it appears that at least a moderately energetic disassembly is plausible if the reactor does enter a LOF-driven-TOP sequence.

For ULOF accidents, fully benign termination, with limited damage and the core coolable, is improbable, at least for CRBR and most other US-type designs. Hence, if the initiation phase does not end in disassembly, a transition phase develops. A number of mechanisms can be identified which are likely to cause mild recriticalities. High sustained ramp rates leading to disassembly do not appear probable, but they cannot be ruled out at present.

For ULOF accidents as a whole, the LOF-driven-TOP appears to be the most important of the various sequences that could lead to disassembly. Over-all, at least a moderately energetic disassembly appears to be as plausible as a nonenergetic outcome. It is important here to emphasize that "disassembly" does not necessarily mean an extremely severe event (ramps > \$100/s, say). No reasons have been identified for believing severe events are at all likely, although they cannot absolutely be ruled out on the basis of current understanding.

6.4.2 UTOP Accidents

Unlike the ULOF initiation phase, the UTOP initiation phase can end in fully benign termination (limited damage with the core coolable). In addition, both a transition phase and disassembly are also plausible outcomes. Thus, there are three major outcome categories for the UTOP initiation phase, rather than just two as in the case of ULOF accidents. If a transition phase does develop, there are significant differences as compared to ULOF accidents, as is discussed in detail in the Interim Report.

Based on present understanding, no choice could be expressed as to the relative likelihood of the three basic outcome categories, that is, benign termination, nonenergetic meltdown, and disassembly. Phenomenological uncertainties requiring resolution in order to answer these questions were identified, and UTOP accidents were delineated with about the same degree of detail as was used for ULOF accidents.

6.4.3 Fuel Dispersal Phase

The fuel dispersal phase was delineated generically, that is, delineations were not carried out separately for each accident category. Attention was concentrated on phenomenologies governing mechanical insult to the primary containment. Major conclusions include

1. Uncertainties in accident mechanical work potentials at the present time are large. The key questions requiring resolution include reactivity ramp rates and heat transfer to steel and coolant during postdisassembly expansion.
2. With some significant qualifications, it appears that fuel-coolant interactions may be more important as a potential source of rapid material motions (and, hence, large reactivity effects) than as a direct source of containment damage.

6.4.4 Other Unprotected Accidents

Other categories of unprotected (no-SCRAM) accidents considered include a step reactivity insertion (U-Step), Unprotected Rupture of the Primary Boundary (URPB), Unprotected Loss of Heat Sink (ULOHS), and Step Insertion or Transient Overpower combined with Loss-of-Flow (U-Step/ULOF and UTOP/ULOF). Only very brief reviews were attempted. Two approaches were used. First, the very limited results of available accident analyses were briefly summarized. Second, the UTOP and ULOF event trees, whichever was most appropriate, and supporting discussion were reviewed in order to identify branch points where, for these additional accident categories, key parameters could assume significantly different values from those characteristic of the UTOP or ULOF reference category.

In the second approach, it appeared that, either the UTOP or ULOF event trees could give a reasonably good qualitative representation of these other categories. In particular, no qualitatively different phenomenologies governing accident energetics were identified as being important to these accidents that were not also important to ULOF or UTOP. Quantitatively, some if these categories may result in different energetics relative to ULOF or UTOP. Defining the nature of these differences in energetics will require further analysis. Perhaps the most important question identified here that requires further study may be the degree to which containment capability is degraded due to overheating in unprotected loss of heat sink accidents.

6.4.5 Protected Accidents

Categorization of protected accidents in which SCRAM is successful, but core disruption eventually occurs due to inability to remove decay heat, has received relatively little attention. Only two examples of this type of accident were considered at all in this work, and these were reviewed but briefly. The work reviewed indicated that meltdown does not necessarily result in recriticality, but recriticality cannot be considered implausible. If it does occur, there is very limited capability for predicting ramp rates or energetics.

Definition of an adequate set of categories for this class of accidents is still required. For each category, key questions will include: presence or absence of pony motor flow, core coolability by natural convection when pony flow is unavailable, and elapsed time prior to core disruption. Core disruption may not occur until many hours after shutdown for some scenarios, and this delay can obviously have important effects on the ultimate consequences.

6.5 Postaccident Phenomenology Summary

The purpose of the containment phase of the accident delineation study is to outline the major cause and effect relationships in an accident sequence following a CDA. Examination of these relationships identifies the effects of various phenomenological events on the quantity and timing of eventual releases of radioactivity to the surrounding environment. The event trees formulated attempt to point out the range of outcome envisaged after fast reactor CDA sequences and the intervening behavior which may affect the character of each outcome.

The event trees constructed in the Postaccident Phenomenology area were based on a generalized containment system which represented the important features for postaccident delineation. A schematic diagram of the containment system considered is shown in Figure 6.5-1.

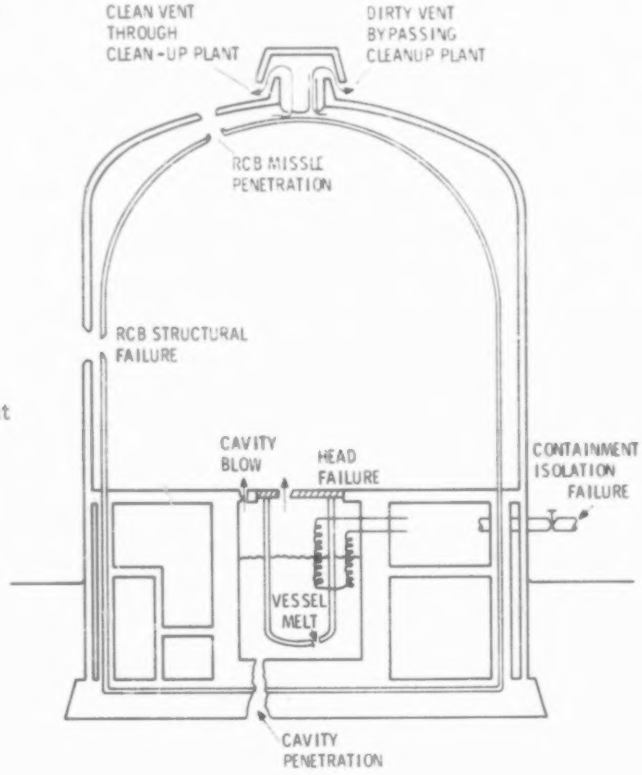
CLEAN VENT THROUGH CLEAN-UP PLANT
DIRTY VENT BYPASSING CLEANUP PLANT
RCB MISSLE PENETRATION
RCB STRUCTURAL FAILURE
CAVITY BLOW
HEAD FAILURE
CONTAINMENT ISOLATION FAILURE
VESSEL MELT
CAVITY PENETRATION

Figure 6.5-1. Model Containment System

The Reactor Containment Building (RCB) considered is provided with a capability of being isolated from the outside atmosphere. In the isolated mode it can vent gases to the atmosphere via a clean-up system (ventilation, scrubbers, filters) and a tall stack. For this study, it was assumed that direct venting could occur but only by accident.

The RCB is characterized by a leak rate which depends on overpressure and which will form a principal component of the release when the RCB retains its structural integrity. Loss of structural integrity of the RCB can occur either by missile penetration or by some other distinct, but unspecified, failure mode brought on by high temperature and/or overpressure.

The floor of the RCB will include one area forming the RCB to vessel/cavity boundary labeled EF in the figure. Failure of this boundary will lead to the introduction of active gases and aerosol into the RCB when driving pressures exist. It is supposed that the reactor vessel and the reactor cavity can be equipped with cooling devices for decay heat removal (DHRS). The location and nature of these devices are unspecified but their performance can be affected by CDA-induced damage and by changes in the sodium level.

The containment analysis area begins with the stage before vessel melt-through and assumes that the vessel damage, if present, can be characterized immediately after the energetic phase of the CDA is over. The condition of fuel debris, bulk sodium, and decay heat removal system is assumed to dictate the subsequent melt-through behavior.

The first branches on the tree address the state of fuel debris beds, the functionability of the DHRS, and the condition of the reactor vessel head. When the vessel head is failed, some sodium is assumed to be ejected to the upper RCB and its combustion products are allowed to interfere with cleanup system functioning, when the latter is available. Provided the RCB is not immediately failed by missiles produced by the CDA event, and provided the RCB isolation systems function, temperature and pressure rises in the RCB atmosphere may cause relatively early RCB structural failure.

CONTENTS

Page

FOREWORD 11 1/A12

EXECUTIVE SUMMARY 13 1/A14

1. ENERGETICS 39 1/C12
   - 1.1 Prompt Burst Energetics 39
   - 1.2 Equation-of-State 51 1/D12

2. FUEL DYNAMICS 67 1/E14
   - 2.1 Fuel Disruption 67
   - 2.2 Transition Phase 75 1/F8
   - 2.3 Initial and Extended Fuel Motion 85 1/G4
   - 2.4 Fuel Motion Detection 88 1/G7

3. CORE DEBRIS BEHAVIOR - INHERENT RETENTION 105 2/A12
   - 3.1 Molten Core Technology 105
   - 3.2 PAHR Debris Bed 127 2/C10
   - 3.3 PAHR Molten Pool 135 2/D4
   - 3.4 Containment Analysis 141 2/D10
   - 3.5 Fragmentation 142 2/D11
   - 3.6 Sodium Containment and Structural Integrity 147 2/E2

4. AEROSOL SOURCE NORMALIZATION 159 2/E14

5. ELEVATED TEMPERATURE DESIGN ASSESSMENT 163 2/F4

6. LMFBR ACCIDENT DELINEATION 175 2/G2

7. TEST AND FACILITY TECHNOLOGY 193 3/A8
   - 7.1 ACPR Upgrade - Initial Test and Operations 193
   - 7.2 ACPR Fuel-Motion Detection System 193
   - 7.3 Large-Scale Test Assessment 195 3/A10

Branch questions in the second half of the tree address melt-through related problems. The first of these inquiries whether long-term coolability of in-vessel debris beds can be contemplated and the answer to this, together with the earlier decisions on DHRS functionability, is used to show the time and circumstances under which material is introduced to the reactor cavity. Subsequent behavior depends strongly on the evolution of gases, particularly sodium vapor and hydrogen from the cavity. Important phenomenological questions which appear are therefore: (1) to what extent are sodium and fuel separated physically and maintained separate from the material from which the cavity floor and walls are constructed, and (2) to what extent does contact between the materials produce a significant pressurization of the upper RCB. Apart from opportunities for further direct venting, eventual RCB failure forms the last branch on the tree.

In terms of the severity of consequences, pathways involving a breach of the upper RCB to atmosphere are of utmost concern. Within such pathways there are three primary events whose occurrence greatly affects the outcomes: (1) failure of the boundary between cavity or vessel and the upper RCB at CDA time; (2) existence of a source of gases and sodium vapor pressurizing the upper RCB; and (3) the failure, for any reason, of the upper RCB to isolate its contents from the outside atmosphere.

The events outlined in the tree determine the cause and timing of these major events and thus determine the composition and magnitude of any release of radioactivity. Event (1) could be caused by overpressurization of the vessel, direct impact of sodium on the vessel head, direct CDA generated missile, etc, but its general effect is to introduce sodium and fuel debris to the upper RCB where its principal effect is the thermal threat to the RCB. Event (2) represents a further direct pressurization source for the upper RCB, introduces efficient decay heat transfer to the upper RCB via sodium vapor and will increase the potential explosion threat from hydrogen production and stratification. Event (3) can be caused by an immediate CDA generated missile, overpressure, isolation system failure, or deliberate or inadvertent direct venting. For each of the tree pathways, the timing of each of these major events is described relative to the CDA time to give five broad sequence categories.

Although assignment of probabilities to each branch was not attempted in this study, a qualitative exercise using broad probability quanta based on intuitive reasoning was performed. The results of this exercise show that existing phenomenological uncertainties dominate the higher probability pathways. These uncertainties are seen mainly in the following areas:

- Debris bed coolability
- Vessel head damage and quantity of sodium ejected in relation to CDA energetics
- Chemistry and reaction kinetics of sodium and fuel debris attack on reactor cavity materials
- Response of the upper Reactor Containment Building to the introduction of sodium vapor, fission products, and hydrogen from the Reactor Cavity.

These general areas of phenomenology control the timescale and magnitude of radiological release for a given range of CDA energetics. Although considerable effort is obviously required in these areas to resolve these issues, it appears that in many cases, significant improvement in understanding may be achieved in the near term. In particular, a more complete understanding of debris bed coolability is important in assessing the relative priority that should be assigned to subsequent phenomenological questions.

Future analysis of consequence mitigation through aerosol plateout and settling during the course of the accident will be required to quantify the risk reduction attainable from LMFBR containment systems. It will also be necessary to address the question of the probability of CDA energetics sufficiently severe to cause immediate or early failure of the RCB.

6.6 Study Observations

Several observations were made during the course of this initial study concerning the impact of the study as a whole and its relationship to some of the more important issues being considered in Fast Reactor Safety.

The first observation concerns the advantages and disadvantages of the event tree method for clarifying and illustrating the interaction of phenomena and systems involved in LMFBR safety. Advantages include: well-developed methodology for application to engineered systems studies; convenience of qualitative diagrammatic illustration combined with (in principle) capability for straightforward extension in quantification, given adequate information; completeness, in the sense that, for the questions judged relevant, all possible combinations of answers can in principle be explicitly represented. (In practical analyses dealing with complex systems, however, the event trees generally require simplification in order to avoid prohibitive complexity, thereby compromising the completeness advantage.) Disadvantages include: difficulty of interpreting probabilities assigned to branch points involving phenomenological uncertainties; and difficulties in representing problem features such as continuously-variable parameters, situations where subsequent events depend upon the net effect of several phenomena acting in parallel, cyclic phenomena, feedback relationships, etc. These disadvantages appear to be more serious in the accident phenomenology area than in the acciden initiation and post-accident phenomenology areas.

The prospects for future quantification of LMFBR accident sequences in terms of event tree branch probabilities and consequence categories was considered for each of the three phases of the study, with the following conclusions:

1. There seems to be no reason why the Engineered Systems phase cannot be adequately quantified in the manner of the Reactor Safety Study (WASH 1400) assuming design data, reliability data, and resources are available. Clearly a massive effort would be required to complete such quantification with a high degree of confidence. Further study of potential unscrammable faults such as massive structural failure would be necessary.

2. The in-core accident phenomenology trees are dominated by highly complex phenomenological uncertainties. Traditionally, LMFBR accident phenomenology studies have concentrated on just three accident categories: local fault propagation, ULOF, and UTOP. The present study generally supports this approach as being reasonable for unprotected (SCRAM fails) accidents, with a few relatively minor qualifications; protected accidents

(SCRAM succeeds) characterized by DHRS failure require more study. For the near term (next few years), estimation of probabilities for the event tree branch points with any confidence is very doubtful because very substantial improvements in phenomenological understanding are required. Since the phenomenologies involved are both complex and strongly interacting, extensive experimental and theoretical research will be required to resolve key questions. Until this is attained, any probabilities assigned to many of the branch points of the accident phenomenology event trees would be highly subjective. Nonetheless, a preliminary exercise of this type may be useful in detailing research priorities more clearly than the present purely qualitative accident delineation study has done.

3. The potential of LMFBR containment to provide an important risk mitigation factor for a range of core disruptive events was apparent in the preliminary quantification effort undertaken in this study. Research efforts in containment phenomenology and systems design should allow reasonable estimates of branch probabilities and consequence categories to be made in the near term. However, confidence in any such risk mitigation factor will be severely limited unless the analysis of in-core accident phenomenology is at least able to demonstrate convincingly that highly energetic outcomes of core disruptive events have a very low probability of occurrence.

Viewing the event trees for accident initiation, accident phenomenology, and containment from the more comprehensive viewpoint of overall facility safety, it is strikingly apparent that the engineered systems and design features play a dominant role in reducing the probability of severe accidents. The availability of the PPS and the DHRS is of key significance in the assessment of plant safety and identification of design features which render exceedingly unlikely certain classes of unscrammable accident initiators, notably major structural failures, merit high priority particularly in the near term.

The in-core phenomenology analysis is unlikely to be able to demonstrate convincingly that significant accident energetics are implausible, at least for the present. On the other hand, no reasons have been identified in the course of this work for believeing that it will be impossible ultimately to demonstrate that extremely severe energetics have a very low probability. Achieving this goal appears to be necessary if the postaccident analysis is to demonstrate that the containment has a very substantial risk reduction capability. Hence, it seems reasonable to concentrate accident phenomenology efforts on questions related to the likelihood of severe energetics rather than concentrate efforts on trying to show that core disruptive accidents will be completely nonenergetic.

The event trees developed at this interim stage represent only a first step in what must be considered as an iterative process in accident delineation. The extension of this type of study to a risk assessment for LMFBR plants obviously requires further development in all areas of the accident description. During the next quarter work will begin on defining those tasks which should be addressed first.

7. TEST AND FACILITY TECHNOLOGY

7.1 ACPR Upgrade - Initial Test and Operations (T. R. Schmidt, 5451)

After achieving criticality last quarter, the Nuclear Startup Tests were continued and completed this quarter. The approach to Full Power Tests was initiated. Fully steady-state power of 2 MW was achieved on July 27, 1978, followed by a period of instrumentation modifications and adjustments, dosimetry and a complete power and temperature mapping of each element in one-sixth of the core. The pulse series was initiated with achievement of a maximum single pulse with a reactivity insertion of $2.95 on August 18, 1978. The multiple pulsing mode and the transient rod withdrawal mode were also characterized.

7.2 ACPR Fuel-Motion Detection System (J. G. Kelly, 4423; K. T. Stalker, 1354)

7.2.1 Introduction

A fuel-motion detection system is being developed for the ACRR. The design of the system will be based upon the experience gained in experiments with shielding, collimation, coded aperture, imaging, and time-resolved pseudoholography at the ACPR, SPR-II, and ^{252}Cf facilities. The system will be designed for high spatial and temporal resolution measurements of fuel motion in both transient and steady-state experiments, bed-leveling and material-separation studies in the postaccident heat removal experiments.

The ACRR fuel motion detection system is designed to take advantage of the latest advances in framing camera design, optical image intensifier developments and coded-aperture imaging technology to measure fuel motion in simulated core disruptive accidents with high temporal and spatial resolution. The coded aperture, in particular, permits the collection of more imaging gamma rays per resolution element in the object per unit time than does a pin hole aperture with the same resolution. Thus, improved signal-to-noise ratios in the fuel pin image can be obtained. At present, the complete system has been designed and most of the major components have arrived. The proof tests are scheduled to start in October 1978 and will begin with assembly tests in the reactor, radiation mapping, and passive (steady-state) imaging of a fuel pin. The experiment plan was outlined in the April-June 1978 Quarterly Report.

This quarterly report will summarize the status of the system fabrication and the preparation for the proof tests.

7.2.2 Status of the Coded Aperture System

Most of the major hardware components have now been received and include the support plate for the entire system, the shield support structure, the front stainless steel scatter plate, the tank container for borated polyethylene, the stainless steel encased lead shield wall, and the instrumentation, aperture, and slot collimator chambers. Sandia has not yet received the lead and borated polyethylene collimators which surround the beam-defining apertures. These collimators are now scheduled to arrive during early October.

The modulating zones of the coded aperture are made of individually cast, tapered vanes of 30% platinum and 70% gold by weight, having a density of about 20 g/cm^3. The maximum vane thickness along the direction of the beam is 1.5 cm, so that if one can assume exponential attenuation in the material, the vanes should attenuate a 1 MeV x-ray beam by $e^{-\mu\rho x} = e^{-(0.08)(20)(1.5)} = 0.1$. This degree of modulation is far better than the 0.5 factor which was achieved in the outer zones of the coded aperture used to image a fuel pin in the ACPR during 1977.

Most of the material parts for the interior of the instrumentation chamber have also been received and assembled. These components include the optical table and support fixtures for the scintillators, the optical image intensifiers, lenses, mirrors, and framing cameras. Some additional parts which will specifically provide shadow shielding protection for individual components inside the instrumentation chamber are also on hand. The Dupont NDT 3 $CAWO_3$ screens are now being tested at the Varian Linatron 1500 Linear Accelerator (LINAC) located at Sandia Laboratories.

To achieve a wider range of dynamic intensity measurement, the optical image intensifier tubes will be gated in synchronization with the framing cameras by pulsed high-voltage power supplies. (The details of the gating systems which have been designed for this system were presented in the preceding quarterly report.) The gating power supplies have been received and tested. They will gate the intensifiers open for periods as short as 5 μs with a rise and fall time of 1 μs. (Investigators do not believe that exposures this short will yield very meaningful images from a quantum statistics point of view, although the system has enough gain for recording within this short a period.) The gating pulses, however, are degraded when they reach a 20% duty cycle. This is below the system requirements of 50%. Modifications are now being made to correct this deficiency.

7.2.3 Status of the Proof Tests

A few weeks delay is expected in the initiation of the proof test series in the ACRR because some components are slipping in their delivery dates. Although some slack time had been allotted to shops for minor modifications and mechanical corrections as the parts were checked out, there have been more required changes than were anticipated. In addition, job and personnel scheduling at the end of the fiscal year slowed shop activity in September. Assembly of the system into the ACRR tank will probably begin during the second week in October, followed shortly thereafter by proof tests.

7.3 Large-Scale Test Assessment (P. S. Pickard, 4424; J. Odom, 4424)

Large-scale test assessment efforts are directed toward the definition of an experimental program such that test data obtained have the potential to confirm analysis and conclusions drawn from smaller scale experiments as related to the core-disruptive accident (CDA). These considerations include the use of existing facilities as well as the definition of requirements for new facilities or modifications to existing ones.

7.3.1 Safety Issues

A need exists to establish a data base related to LMFBR safety analysis. Many extensive design studies have been performed for test facilities in which key safety issues can be resolved. Such facility designs depend critically on test specifications and requirements needed to resolve key safety questions. An effort is now underway to identify the major safety issues and safety programs to address these issues.

The tests required to study the LMFBR safety issues include small-scale phenomenological tests in-pile and out-of-pile; but many issues must be addressed with large-scale prototypic experiments. The report now in progress will discuss these and related topics and will propose large-scale test requirements to address the safety issues. The issues to be studied revolve around the core disruptive accident and are placed in eight categories as follows:

1. Transient Overpower - The effect of intra-subassembly failure incoherencies (in both space and time), reactivity insertion from fuel motion and sodium voiding, subassembly plugging, failure location, and fuel plateout.
2. Transition Undercooling - loss-of-flow, loss-of-heat sink, flow blockages, sodium boiling and voiding, fuel motion, and fuel blockage formations.
3. Transition Phase - degree of axial fuel dispersal, height of boil-up, upper structure plugging and ablation, and axially dependent radially heat transfer of boiling core.
4. Disassembly Phase - fission energy release during burst, rate of reactivity insertion (including feedback), fuel-coolant interactions, equation-of-state and heat transfer for fuel/steel mixtures, and behavior of above core pin structure.
5. Energy Partition and Damage Evaluation - determination of pressure source, propagation of pressures, failure propagation, molten core material interaction with above core sodium, fuel-sodium interactions (steel quenching), and shock-induced fragmentation.
6. Postaccident Heat Removal - debris bed dryout, fuel/steel/sodium/sacrificial material interactions, and molten pool dynamics.
7. Extended Material Motion - flow regime of ejected material, freezing, plugging, response of structure, interaction with above-core sodium pool or subassembly structure, and material reentry coherency.

8. Radioactive Material Transport - fuel liquid vapor release, characterization of radioactive particle size, activity and velocity, sodium spray pressurization, and sodium fires, air-cleaning system effectiveness under accident conditions, and motion of radioactive particulates under meteorological influence.

7.3.2 Study Support

Analytical support of the international fast reactor safety exchange program continued this quarter. Fission density profiles were calculated for a CABRI common test pin in the CABRI reactor with TWOTRAN and showed excellent agreement with the French results (Figure 7.3-1). The CABRI reactor was also modeled in the coupled heat-transfer/point-kinetics computer code, PKID. Power histories and profiles are being generated for various reactivity insertions (Figure 7.3-2). These results are input to the fuel failure code EXPAND to confirm recent A-series tests and predict future tests.

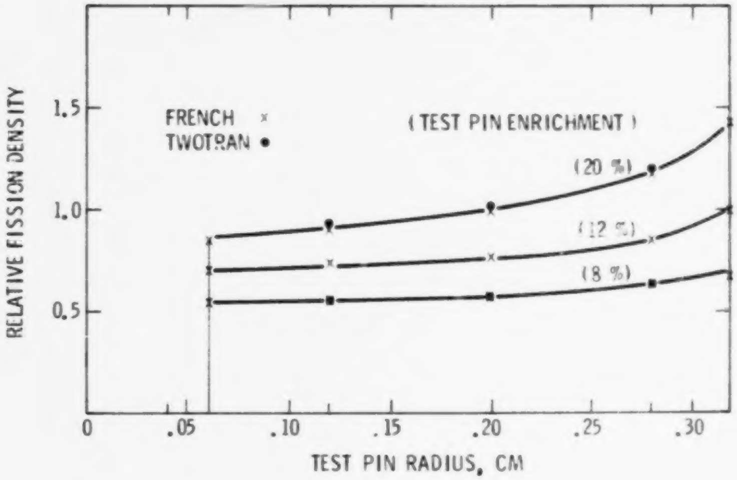

Figure 7.3-1. Fission Density Profiles in CABRI Test Pins in CABRI Reactor

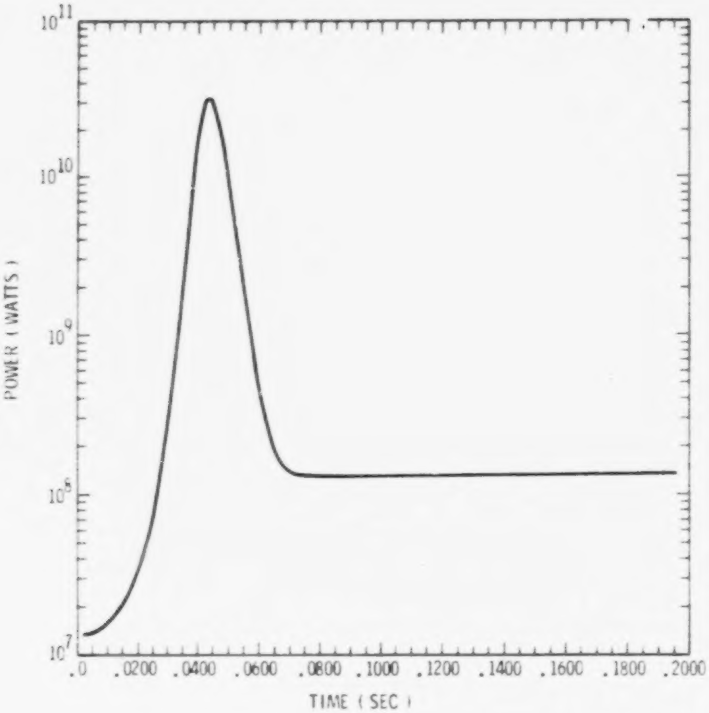

Figure 7.3-2. Power History in CABRI, P_o = 14 MW, P = \$2.7

DISTRIBUTION:

US Nuclear Regulatory Commission
(310 copies for R7)
Division of Document Control
Distribution Services Branch
7920 Norfolk Ave.
Bethesda, MD 20014

US Nuclear Regulatory Commission (4)
Division of Reactor Safety Research
Office of Nuclear Regulatory Research
Washington, DC 20555
Attn: C. N. Kelber, Assistant Director,
Advanced Reactor Safety Research
R. T. Curtis, Chief
Analytical Advanced Reactor
Safety Research, ARSR
M. Silberberg, Chief
Experimental Fast Reactor Safety
R. W. Wright
Experimental Fast Reactor Safety

US Department of Energy
Office of Nuclear Safety Coordination
Washington, DC 20545
Attn: R. W. Barber

US Department of Energy (2)
Albuquerque Operations Office
P. O. Box 5400
Albuquerque, NM 87185
Attn: J. R. Roeder, Director
Operational Safety Division
D. K. Nowlin, Director
Special Programd Division
For: C. B. Quinn
D. Plymale

University of Michigan
Nuclear Engineering Department
Ann Arbor, MI 48104

General Electric Corporation
310 De Guigne Drive
Sunnyvale, CA 94086
Attn: J. O. Bradfute, Manager
Dynamics and Safety

W. E. Nyer
P. O. Box 1845
Idaho Falls, ID 83401

Projekt Schneller Brueter (4)
Kernforschungszentrum Karlsruhe GMBH
Postfach 3640
D75 Karlsruhe
West Germany
Attn: Dr. Kessler (2)
Dr. Heusener (2)

Istitut de Protection
et de Surete Nucleaire (3)
CEN Fontenay-aux-Roses
B. P. 6
92260 Fontenay-aux-Roses
France
Attn: M. Tanguy
M. Schmitt
M. Cogne

Safety Studies Laboratory (3)
Commissariat a L'Energie Atomique
Centre d'Etudes Nucleaires de Cadarache
B. P. 1, 13115 Saint-Paul-les-Durance
Bouches-Du-Rhone
France
Attn: M. Bailly
M. Meyer Heine
M. Penet

Centre d'Etudes Nucleaires de Grenoble
B. P. 85, Centre de Tri
38401 Grenoble, Cedex
France
Attn: M. Costa

UKAEA (3)
Safety and Reliability Directorate
Wigshaw Lane
Culcheth
Warrington, WA3 4NE
England
Attn: H. J. Teague

R. G. Bellamy
Reactor Fuels Group
AERE Harwell
Oxfordshire, OX11 ORA
England

DISTRIBUTION (cont):

UKAEA - Atomic Energy Establishment
Winfrith, Dorchester
Dorset
England
Attn: R. G. Tyror, Head
Reactor Development Division

Power Reactor & Nuclear Fuel
Development Corp (PNC) (2)
Fast Breeder Reactor Development
Project (FBR)
9-13, 1-Chome, Akasaka
Minato-Ku, Tokyo
Japan
Attn: Dr. Mochizuki
Dr. Watanabe

1100	C. D. Broyles
	Attn: G. E. Hansche, 1120
	G. L. Ogle, 1125
	H. E. Viney, 1130
	J. H. Davis, 1136
1537	N. R. Keltner
	R. U. Acton
	T. Y. Chu
1550	F. W. Neilson
	Attn: O. J. Burchett, 1552
	J. H. Gieske, 1552
2150	T. L. Workman
3434	B. N. Yates
4000	A. Narath
4231	J. H. Renken
	J. A. Halbleib
	P. J. McDaniel
	J. E. Morel
4400	A. W. Snyder
4410	D. J. McCloskey
4420	J. V. Walker (5)
4422	R. L. Coats
4422	J. E. Gronager
4422	G. W. Mitchell
4422	J. B. Rivard
4422	D. W. Varela
4423	J. E. Powell
4423	G. L. Cano
4423	A. C. Marshall
4423	J. G. Kelly
4423	D. A. McArthur
4423	K. O. Reil
4423	H. L. Scott
4423	K. T. Stalker
4423	W. H. Sullivan
4423	S. A. Wright
4424	P. S. Pickard
4424	J. T. Hitchcock
4424	D. H. Worledge
4425	W. J. Camp
4425	R. W. Ostensen
4425	D. C. Williams
4425	M. F. Young
4425	R. J. Lipinski
4425	W. M. Breitung
4442	W. A. Von Riesemann
4450	J. A. Reuscher
4451	T. R. Schmidt
4452	L. D. Posey
5500	O. E. Jones
5511	M. L. Corradini
	D. O. Lee
5530	W. Herrmann
5534	D. A. Benson
	J. E. Smaardyk
5800	R. S. Claassen
5820	R. E. Whan
5821	N. E. Brown
5830	M. J. Davis
5831	N. J. Magnani
5831	D. A. Powers
5836	J. L. Ledman
5846	R. A. Sallach
	E. K. Beauchamp
8266	E. A. Aas
3141	T. L. Werner (5)
3151	W. L. Garner (3)
	For: DOE/TIC (Unlimited Release)
3154-3	R. P. Campbell (25)
	For NRC Distribution to NTIS